Optical Injection Locking of Vertical Cavity Surface Emitting Lasers

by

Lukas Chrostowski

B. Eng. (McGill University) 1998

A dissertation submitted in partial satisfaction of the
requires for the degree of
Doctor of Philosophy

in

Engineering – Electrical Engineering and Computer Science

in the

GRADUATE DIVISION
of the
UNIVERSITY of CALIFORNIA at BERKELEY

Committee in charge:

Prof. Constance J. Chang-Hasnain, Chair
Prof. Kam Lau
Prof. Peter Y. Yu

Spring 2004

The dissertation of Lukas Chrostowski is approved:

_____

Chair Date

_____

Date

_____

Date

University of California, Berkeley

Spring 2004

Optical Injection Locking of Vertical Cavity Surface Emitting Lasers

Acknowledgements

Professor Connie Chang-Hasnain

Qualifying exam committee, Professor Kam Lau, Professor Peter Yu, Professor David Attwood

Interaction and collaboration with present and past research group members
Dr. Dan Francis VCSEL laser micro-fabrication, characterization
Dr. Robert Stone fiber communications, high-speed measurements, digital, friendship,
Steve Chase, Jeff Waite, Jacob Hernandez, Pei-Cheng Ku, Carlos Mateus, Paul Hung, Mike Huang, Michael Moewe, Wendy Xiao-Xue Zhao
Chih-Hao Chang

NSERC

Peter Schultz and Rajesh Patel at MIT Lincoln Labs for their assistance with the RIN measurements

Bandwidth 9 Inc. Rob Stone, Julien Boucart, Peter Kner, Wupen Yuen

Dr. P. C. Chen at Emcore / Ortel Inc.

Professor M.C. Amann and Robert Shau at the Walter Schotky Institute, Germany.

Dad
Family
Jessica

Publications

Peer-Reviewed Journal Publications

L. Chrostowski, C. H. Chang, and C. J. Chang-Hasnain, "Injection-Locked 1.55 um Tunable VCSEL for Uncooled WDM Transmitter Applications," *IEEE Photonics Technology Letters*, vol. (to be published), 2004.

C. H. Chang, L. Chrostowski, and C. J. Chang-Hasnain, "Injection Locking of VCSELs," *IEEE Journal of Selected Topics in Quantum Electronics*, (to be published), 2004.

L. Chrostowski, C. Chih-Hao, and C. J. Chang-Hasnain, "Enhancement of dynamic range in 1.55-um VCSELs using injection locking," *IEEE Photonics Technology Letters*, vol. 15, pp. 498-500, 2003.

L. Chrostowski, C. H. Chang, and C. J. Chang-Hasnain, "Injection-locked 1.55 um VCSELs with enhanced spur-free dynamic range," *Electronics Letters*, vol. 38, pp. 965-7, 2002.

L. Chrostowski, C. Chih-Hao, R. Stone, and C. J. Chang-Hasnain, "Demonstration of long-wavelength directly modulated VCSEL transmission using SOAs," *IEEE Photonics Technology Letters*, vol. 14, pp. 1369-71, 2002.

C. H. Chang, L. Chrostowski, C. J. Chang-Hasnain, and W. W. Chow, "Study of long-wavelength VCSEL-VCSEL injection locking for 2.5-Gb/s transmission," *IEEE Photonics Technology Letters*, vol. 14, pp. 1635-7, 2002.

W. W. Chow, H. C. Schneider, S. W. Koch, C. Chih-Hao, L. Chrostowski, and C. J. Chang-Hasnain, "Nonequilibrium model for semiconductor laser modulation response," *IEEE Journal of Quantum Electronics*, vol. 38, pp. 402-9, 2002.

C. F. R. Mateus, C. Chih-Hao, L. Chrostowski, S. Yang, S. Decai, R. Pathak, and C. J. Chang-Hasnain, "Widely tunable torsional optical filter," *IEEE Photonics Technology Letters*, vol. 14, pp. 819-21, 2002.

C. H. Chang, L. Chrostowski, and C. J. Chang-Hasnain, "Parasitics and design considerations on oxide-implant VCSELs," *IEEE Photonics Technology Letters*, vol. 13, pp. 1274-6, 2001.

Invited Conference Proceedings

L. Chrostowski, C.-H. Chang, C. Chang-Hasnain, “High speed enhancement of directly-modulated VCSELs by injection locking,” to be presented at *Vertical-Cavity Surface-Emitting Lasers VIII, SPIE*, 2004 (**Invited**).

C. H. Chang, L. Chrostowski, and C. Chang-Hasnain, "Enhanced VCSEL Performance by Optical Injection Locking for Analog and Digital Applications," presented at *Laser and Electro Optic Society*, Tucson, AZ, 2003 (**Invited**).

C. H. Chang, L. Chrostowski, and C. J. Chang-Hasnain, "Injection-locked 1.55 um VCSELs in analog and digital communication systems," *LEOS Summer Topical Meetings*, Quebec, Canada, TuD2, 2002 (**Invited**).

Conference Proceedings

L. Chrostowski, M. Moewe, W. Zhao, C.-H. Chang, C. Chang-Hasnain, R. Shau, M. Ortsiefer and M.-C. Amann, “39 GHz Intrinsic Bandwidth of a 1.55 um Injection-Locked VCSEL,” submitted to *Conference on Lasers and Electro-Optics*, 2004.

C. H. Chang, L. Chrostowski, and C. J. Chang-Hasnain, "23 GHz injection-locked 1.55 um VCSEL," to be presented at the *Optical Fiber Conference*, 2004.

L. Chrostowski, C. H. Chang, and C. Chang-Hasnain, "Reduction of Relative Intensity Noise and Improvement of Spur-Free Dynamic Range of an Injection Locked VCSEL," presented at *Laser and Electro Optic Society*, Tucson, AZ, 2003

L. Chrostowski, C. H. Chang, R. Stone, and C. J. Chang-Hasnain, "Uncooled Injection-Locked 1.55 um Tunable VCSEL as WDM Transmitter," presented at *Optical Fiber Communications Conference*, 2003.

C. H. Chang, L. Chrostowski, and C. Chang-Hasnain, "Frequency Response Enhancement of Injection-Locked Lasers," *Conference on Lasers and Electro-Optics*, 2003.

C. H. Chang, L. Chrostowski, and C. J. Chang-Hasnain, "Analog modulation dynamic range enhancement using injection-locked 1.55 um VCSELs," *IEEE International Semiconductor Laser Conference*, pp.117-18, 2002.

C. H. Chang, L. Chrostowski, and C. J. Chang-Hasnain, "Transmission improvement of VCSEL at 2.5Gb/s under injection locking by another VCSEL," *IEEE Lasers and Electro-Optics Society*, vol. 2, pp.728-9, 2001.

L. Chrostowski, C. H. Chang, R. J. Stone, and C. Chang-Hasnain, "Study of long-wavelength directly modulated VCSEL transmission using SOA amplifiers," poster at *European Conference on Optical Communication*, vol.3, pp.432-3, 2001.

C. H. Chang, L. Chrostowski, and C. J. Chang-Hasnain, "Parasitics and design considerations on oxide-implant VCSELs," 17th *International Semiconductor Laser Conference*, pp.95-6, 2000.

Abstract

Optical Injection Locking of Vertical Cavity Surface Emitting Lasers

by
Lukas Chrostowski
Doctor of Philosophy in Engineering – Electrical Engineering and Computer Science
University of California, Berkeley
Professor Constance J. Chang-Hasnain, Chair

Semiconductor optoelectronics are a major enabling component in optical communications. Directly modulated diode lasers are widely deployed in today's high-speed digital optical communications. They are compact, low cost and consume low power. However, their inherent nonlinearity and noise made them, thus far, unsuitable for analog transmission. Additionally, the frequency response has prevented directly modulated lasers to being usable for high speed digital transmission at bit-rates above 10 Gb/s. Instead, high performance links have used continuous wave lasers in conjunction with external optical modulators, which can be made to have a higher linearity and higher speed. The disadvantages are in size, cost in materials and integration, and power consumption.

For low-cost, high-performance optical data links, it is of interest to increase the performance of directly modulated semiconductor lasers. It was found that a technique called optical injection locking can drastically improve the performance of a transmitter laser. Optical injection-locking uses a second laser to inject photons at a similar wavelength into the transmitter laser. The transmitter laser is thus locked (in wavelength and phase) to the master due to the coherent non-linear interaction inside the laser cavity. The advantage of injection locking is that the transmitter laser characteristics may change fundamentally resulting in a far better device performance, achieving large signal modulation at a far higher frequency than achieved today. The work has demonstrated an experimental record modulation bandwidth of nearly 40 GHz for a directly modulated vertical cavity laser.

With the use of a 1.55 um vertical cavity surface emitting laser (VCSEL), we recently showed that optical injection locking is a very promising scheme to enhance the analog transmission characteristics of a directly modulated laser. The unique high Q cavity in a VCSEL makes the injection locking far more efficient, stable and requires much less injection power. A record 25 dB increase in spur free dynamic range (SFDR), 7X relaxation oscillation frequency and 5-10 dB increase in modulation efficiency have been experimentally demonstrated. Additionally, a laser noise reduction is achieved. The theoretical modeling confirms the experimental results.

With the demonstrated improvements in directly modulated laser transmission, high performance transmitters using injection locking can be envisioned. A novel 1-to-N locking scheme is proposed, where one master laser could wavelength lock an array of

lasers at a reproducible wavelength spacing. This would substantially reduce the size and cost of a multi-channel transmitter. Eliminating the temperature and wavelength controllers in a transmitter is very desirable, since these are the most bulky and power intensive components in a transmitter module. Using tunable VCSELs with injection-locking, we have shown that the devices become temperature insensitive with a performance enhancement due to locking. Their wavelength remains locked over an ambient temperature range, with a nearly constant resonance frequency and linearity.

The injection-locking technique has been theoretically and experimentally shown to be extremely effective at improving the performance of semiconductor lasers, which to date, have not been possible otherwise. This technique will enable higher speed communications, paving the way for a new higher performance transmitter. Furthermore, theoretical and experimental work at the much higher frequencies is expected to reveal a further understanding of laser physics.

_____

Professor Connie J. Chang-Hasnain

Dissertation Committee Chair

Table of Contents

List of Figures

Chapter 1 Introduction

The invention of semiconductor lasers, optical fibers, and optical amplifiers has revolutionized the field of telecommunications. In the last 30 years, very high bandwidth fiber optic links have been made available. The data transmission capacity has enabled and improved a multitude of applications, including long distance and trans-oceanic telephone systems, and most importantly, data communications. The internet has clearly made huge impacts in the lives of the industrialized nation citizens, and its use now dominates worldwide data traffic with expectations of continued growth.

Digital transmission of data dominates the field of fiber communications. In a typical link, a transmitter consists of a laser that is either directly modulated or modulated with an external modulator. The modulation is typically on-off modulation representing digital 0s and 1s, with a bit-rate typically < 10 gigabit/s. Multiple transmitter channels can be combined into a fiber to provide a very high capacity link, ex. > 1 terabit/s. The combination of multiple channels is achieved by wavelength division multiplexing (WDM), where multiple transmitter wavelengths are combined into the fiber using a wavelength selective multiplexer, such as an arrayed wavelength grating (AWG). The number of channels that can be combined in the link is very large, since the optical bandwidth of the fiber is large. A typical system operates in the 1530-1610 nm (C-L band) with a channel spacing of 50 to 100 GHz, easily allowing for 80 channels. The data propagates in the fiber with distances on the order of 100s meters for local area networks (LAN), 100s km for wide-area networks (WAN) in metro areas and country wide networks, to 1000s km for trans-oceanic links. Amplification of the data is provided all-optically using erbium-doped fiber amplifiers (EDFAs) spaced every ~100 km. The receiver consists of a demultiplexer followed by high-speed photodetectors. A typical point-to-point link system diagram is shown in Figure 1.

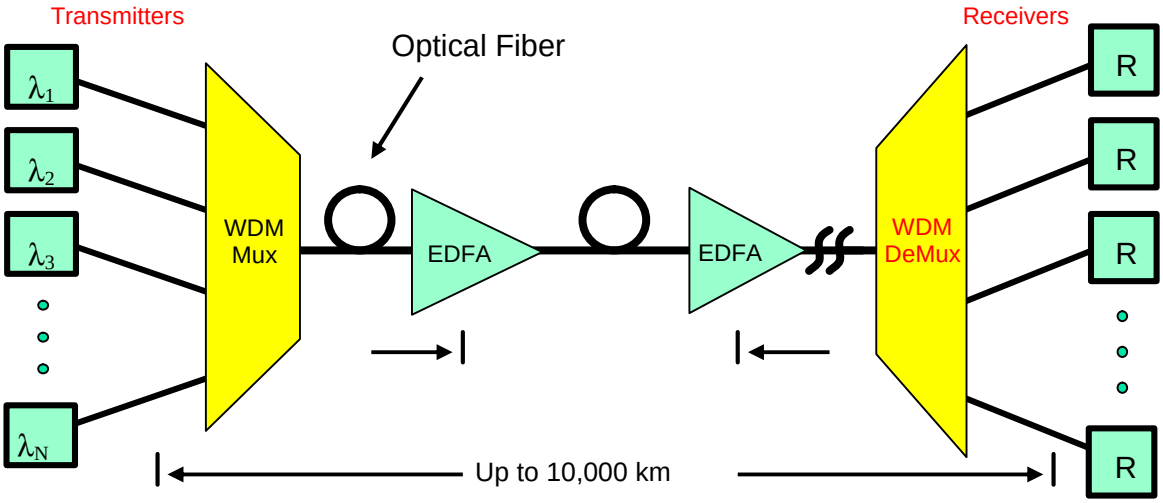

Figure 1 – Fiber optic wavelength division multiplexed data transmission

Although transmission of data is dominantly in the digital format, analog distribution also has many applications with a high demand. Analog communication

tends to be more bandwidth efficient allowing higher data throughput that the on-off-keying (OOK) methods employed in digital transmission. Additionally, it is often more cost efficient to transmit the data in its native format instead of undergoing the costly digitization that would otherwise be required. Video distribution, such as home cable television (CATV) is one application where analog fiber optical links have made a tremendous impact in reducing the cost of long distance transmission. Fibers have replaced the coax or metal millimeter waveguides used for interfacing to antenna, in particular for remote antenna applications: Cellular telephone companies have employed analog links for connecting the base-stations with transmitter sites, phase-array antenna systems can be interconnected using analog fiber links, and radar and high bandwidth wireless RF transmitters can be bridged to the base-station via fiber. Radio-over-fiber [1] and in-building wireless signal distribution is another application seeing much interest in fiber transmission. Ultra-wide bandwidth (UWB) communications may require fiber links. Sensor and instrumentation communication can be done using fibers in harsh environments where optical fibers offer immunity to RF interference, for example. Finally, fiber-to-the-home (FTTH) has been proposed for very high bandwidth availability to the home. Fiber optic distribution of high definition TV signals (HDTV) using analog modulation has been proposed, via digitally modulated subcarrier multiplexing (QAM) [2].

1.1. Optical Transmitters

A typical analog fiber link diagram is shown in Figure 2. The goal of the analog link is to provide an RF output signal that is a faithful reproduction of the RF input. Typically, the fiber, optical amplifiers, photodetector, and electronic amplifiers have a very good performance in terms of linearity. It is the optical transmitter that usually limits the performance of the link.

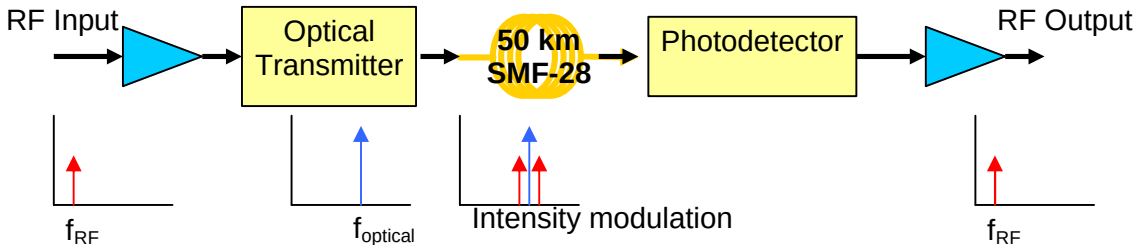

Figure 2 – Fiber optic analog fiber link

The best transmitters available are high power, low noise DFB lasers, modulated externally using a lithium-niobate modulator. The laser provides a stable, high power, low noise light source, while the modulator provides a flat frequency response. The modulator non-linearities (sinusoidal transfer function) are compensated using an electronic pre-distortion filter. This results in a link with a faithful reproduction of the input.

The externally modulated DFB laser approach to the transmitter is shown in Figure 3a. As it offers the highest performance, it is currently prevalent in most analog links and in all digital links with bit-rates above 10 Gb/s. Very high bandwidths, > 75 GHz, can be achieved with external modulators [3]. However, there are several disadvantages

associated with the use of external modulators. They tend to be very bulky, expensive and consume much RF power. Further they have a high optical loss, typical 6-7 dB mainly due to coupling loss. For WDM links, wavelength stability of the CW laser must be provided a feedback loop, which includes a Fabry-Perot etalon for monitoring the wavelength and a temperature controller for fine control.

Direct modulation of semiconductor lasers is a simple way of achieving a low cost transmitter, shown in Figure 3b. Simple drive electronics, small size and low power consumption characterize such transmitters. The disadvantages include a limited bandwidth, high distortion, high noise, frequency chirp, and limited optical power. Limiting factors in such transmitters originate in the semiconductor physics, in the device parasitics [4], and in the rate equations describing the dynamic properties [5]. Directly modulated lasers with a bandwidth as high as 40 GHz have been demonstrated [6]. Most links to date use an edge emitting structure, such as a distributed feedback (DFB) laser, for 2.5 GB/s directly modulated. As in the externally modulated link, wavelength stabilization must also be provided.

Another class of lasers, vertical cavity surface emitting lasers (VCSELs), offer an even greater cost advantage due to wafer testing, a small size leading to efficient material usage, and a possibility of integrating arrays of transmitters. Additionally, wavelength tunable VCSELs have been manufactured at the 1.55 um telecommunication wavelength [7]. These lasers can be used for directly modulated 2.5 Gb/s links with distances ~100 km.

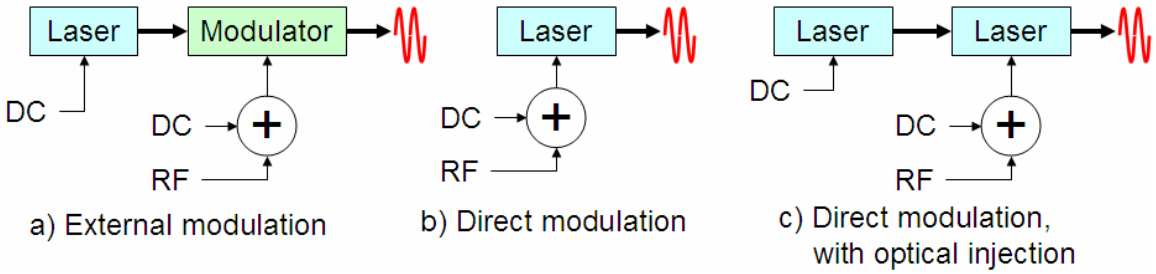

Figure 3 – Modulation schemes for the transmitter.
a) External modulation has the best performance (high linearity, high optical power, low chirp, low noise), with a trade-off of a high cost and power consumption. b) Direct modulation, the lowest cost solution, suffers from low frequency response, high chirp, non-linearity, noise. c) Injection-locking of a directly modulated laser offers the cost advantage with the possibility of sharing the injection master laser between several transmitters. Compared to a directly modulated laser, injection-locking enhances the RF bandwidth, reduces the noise, reduces non-linearities, and reduces chirp and linewidth.

The topic of this thesis, optical injection-locking, shown in Figure 3c, is a technique which can improve upon the performance of directly modulated lasers, yielding a performance comparable to externally modulated links.

1.2. Optical Injection Locking

Optical injection-locking of semiconductor lasers, is an alternative method for designing high performance transmitters. It involves using two lasers – a master laser and a follower laser (also referred to as “slave”). The master laser light is incident onto the follower laser, which alters the behavior of the follower laser. The locking

phenomenon occurs when the two lasers have wavelengths that are nearly matching. Depending on the frequency detuning and the injection power, the injection-locked laser can be stably locked, unstably locked or exhibit chaotic behavior. In the stable locking regime, injection-locking improves upon the performance of a directly modulated laser.

The improvements due to locking include an enhancement to the modulation bandwidth, a reduction in the laser noise, reduction in non-linearities, and reduction in chirp and linewidth. The follower laser wavelength is locked to the master, and can thus be used for locking the transmitter to the WDM grid.

For high speed modulation, one can use a low noise master laser with poor high-frequency characteristics to lock a noisier, high-speed packaged follower laser, yielding low noise and high speed operation. Injection-locking gives the additional design freedom with greatly increased performance that makes injection-locked directly modulated lasers attractive for various applications.

1.2.1. Background

The frequency locking phenomenon between two oscillators has been an area of interest for physicists and mathematicians for centuries. In 1600s, Huygens [8] first discovered the synchronization between two clocks on the wall. The phenomenon did not begin to be understood until the development of nonlinear dynamics by Poincare, and Van der Pol was first to study the forced oscillator in detail. Adler [9] later demonstrated that this frequency locking synchronization between oscillators can also apply to electronic circuits and opened up a new era in communications and power electronics.

Starting in the 1980s, when well-engineered semiconductor lasers became available, injection locking between two lasers was actively researched [10-12] and proposed for applications such as receiver end design in optical coherent communication [13].

Injection locking was suggested as an effective method to reduce laser noise [14] and optical spectral width [11], for the case when the follower laser is under continuous wave (CW) operation. For the case when the follower laser is directly modulated, injection locking was predicted to reduce frequency chirp [15, 16], increase the frequency response [17], and reduce non-linear distortions [18].

Theoretical work in understanding injection locking of lasers has been an interesting topic since it was discovered. A rate equations based model is usually used to describe the interaction between photons and carriers inside a laser cavity. When an additional light source is injected into the cavity, the system preserves the general form of the original equations, but with extra terms describing the effects of the injection [19]. These extra terms play an important role in this nonlinear dynamic system, and the following equations are used in this thesis for the simulations:

$$\frac{dS}{dt} = \frac{G_0(N-N_0)}{1+eS}\cdot S - \frac{S}{t_p} + \boxed{2k_c\sqrt{S\cdot S_{inj}}\cdot\cos(\ f(t)-f_{inj}\ )} + R_{sp} + F_s \qquad (1.1)$$

$$\frac{df}{dt} = \frac{a}{2}G_0(N-N_{th}) - \boxed{2p\cdot\Delta\ f - k_c\sqrt{\frac{S_{inj}}{S}}\cdot\sin(\ f(t)-f_{inj}\ )} + \frac{F_f}{S} \qquad (1.2)$$

$$\frac{dN}{dt} = \frac{I}{q} - \frac{N}{t_s} - \frac{G_0(N-N_0)}{1+eS}\cdot S + F_n \qquad (1.3)$$

In these equations, S denotes the photon number, G_0 the material gain, N_0 the transparency carrier number, N_{th} the threshold carrier number, e the gain compression factor, t_p the photon lifetime, k_c the coupling coefficient of the injected light into the cavity, S_{inj} the master laser photon number, f the photon phase inside the original cavity, f_{inj} the phase of the injected light, R_{sp} the spontaneous emission rate, a the linewidth enhancement factor, Δf the frequency difference, or detuning, between the two lasers, and F_s, F_f, F_n denotes the Langevin noise terms in photon, phase and carrier respectively. The terms within the dashed box are introduced by the additional injection light source.

By changing the magnitude and the optical frequency of the injection master laser, the follower laser can operate in different regimes [20]: stably locked to the injected laser frequency; amplitude modulated at the detuning frequency (beating); self-pulsating at the relaxation frequency, or become chaotic. Because of the sensitivity of such a nonlinear dynamic system to the initial conditions and the parameters describing it, immense computing power is necessary to explore all these interesting phenomena.

It is interesting to note from equations (1.1)-(1.3) that if S_{inj}=0 and the noise terms are neglected, the coupled equations are reduced to the original two coupled rate equations [5].

From the steady state solution, the stable locking range can be approximated to be:

$$-k_c\sqrt{\frac{S_{inj}}{S}}\sqrt{1+a^2} \le 2p\cdot\Delta f \le k_c\sqrt{\frac{S_{inj}}{S}} \qquad (1.4)$$

Using this relation, a stability plot for the injection-locked laser can be plotted, as shown in Figure 4. It is also sometimes referred to as the Arnold tongue plot. Since the experimentally measured quantity is typically the wavelength of the two lasers, we typically plot $\Delta\lambda$ (instead of Δf) as a function of the injection power. The detuning is defined as $\Delta\lambda = \lambda_{master} - \lambda_{follower}$.

As can be seen from (1.4), k_c is perhaps the most important parameter. For a given injection power, the larger k_c is, the larger the locking rage (i.e. detuning within which stable locking is maintained). For typical parameters, the k_c of a VCSEL is 30-100 times larger than that of a DFB laser, with a typical value of ~4 x 10^{12} Hz. Thus, VCSEL injection-locking is expected to be much more easily achievable, with a larger possible detuning range.

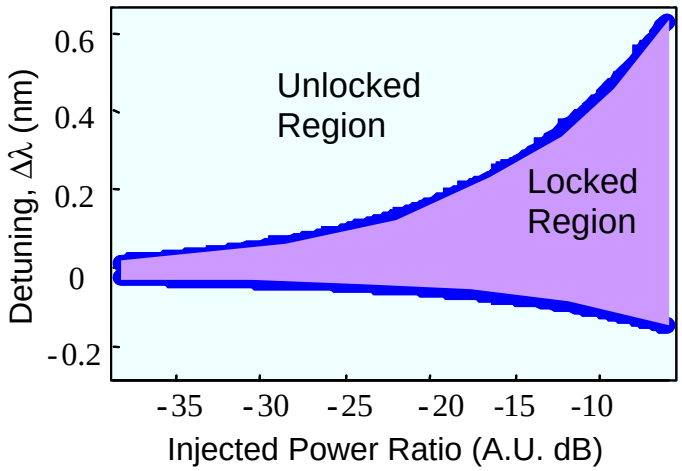

Figure 4 - Stability plot of wavelength detuning vs. injection intensity.
The higher the injection power, the larger the detuning can be allowed to achieve stable locking.

1.2.2. Previous Experiments

Experimental work on semiconductor laser injection locking started in the 1980s. Kobayahi and Kimura [21] first demonstrated laser diode injection locking experimentally. C. Henry [22] explored the locking range of an InGaAsP laser diode. A transmission performance improvement at 2 Gb/s using the injection locking technique was demonstrated with ridge-type DFB lasers for both master and follower, in 1985 [12]. In the mid 90s, an eye diagram improvement for a 10 Gb/s system was also demonstrated [16], using an external cavity tunable laser as the master, and a DFB for the follower. In addition to digital modulation improvement, small signal modulation was also experimentally shown to have a three times enhancement in the relaxation oscillation frequency when it is injection locked to another laser [18]; in the same experiment, the linearity of the laser was also improved.

Early work on injection-locking typically was focused on the weak injection regime [10, 23-25]. In the weak regime, the locking range is typically very small, and is usually only for positive wavelength detuning (negative frequency detuning). Additionally, in this regime, chaotic behaviour, resonant oscillations, and unstable locking limit the usefulness of injection-locking in practical systems [26, 27]. In contrast, the strong injection regime is characterized by a large, stable locking range (0.5 nm). The unstable locking range is usually bounded in the strong injection regime [24].

Using injection-locking has allowed for the experimental determination of laser parameters using the four-wave mixing method [28, 29]. With the laser and injection parameters experimentally determined, the small-signal frequency response was predicted using an analytic approach. In this experiment, the locked resonance frequency was predicted to be 29 GHz with a 35 GHz modulation bandwidth [30].

Laser relative intensity noise (RIN) reduction was also observed under injection locking [31, 32]. In [31], the follower laser was an edge-emitting laser with a low side-mode suppression. Thus, the follower laser could be locked when the master was closely tuned to one of the follower laser side modes; this was termed inter-modal injection

locking. Using this technique, it was possible to lock at an 8.3 nm detuning; thus, wavelength conversion was proposed using this technique. In these experiments, the master lasers used were either external cavity lasers or DFB lasers, which typically have narrow linewidth around MHz or even kHz range.

Inter-modal injection-locking [33] has been experimentally demonstrated, for locking of Fabry-Perot edge emitting lasers. It was found that the resonance frequency enhancement depended on the mode locked; in particular, the longer wavelength modes experienced the highest enhancement.

Experimental and theoretical work on optical injection-locking of vertical cavity surface emitting lasers (VCSELs) has been performed. VCSEL locking with theory including effects of modal competition, has been modeled [34]. 850 nm VCSEL locking experiments have been performed showing successful locking over a large range of 80 GHz [35]. Polarization switching of VCSELs using injection-locking has been shown [36], and recently the effect has been used for an optical inverter [37]. Finally, injection-locking of VCSEL arrays has been theoretically modeled [38, 39].

Our early experiments demonstrated a vertical cavity surface emitting laser (VCSEL) to injection locking another VCSEL [22], with a diagram of the setup shown in Figure 5. This experiment challenged two previous assumptions: (a) the master needs to have a narrow linewidth and (b) a high injected power is required for the locking. The master VCSEL we used has a rather broad linewidth of 100MHz. In addition, a very low injection power of 30 uW was used. The follower laser was directly digitally modulated at 2.5 Gbps, and the signal propagated through 50 km of standard single mode fiber. We achieved an improvement of 2dB reduction in minimum required power for a fixed bit error rate (BER) of 10^{-9}. This is the first time a master laser with low power and broad linewidth is shown to be effective in injection locking, showing experimental proof of chirp reduction with a BER curve and with propagation through an optical fiber.

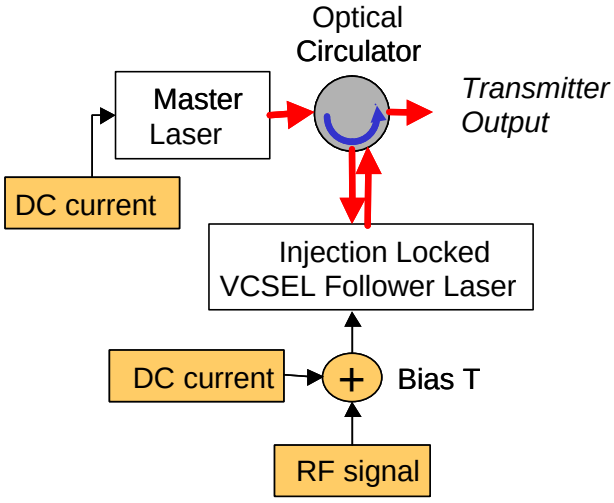

Figure 5 - Injection-locking experimental setup

1.2.3. Applications

Recently, several applications have arisen from the injection-locking technique,

including radio-over-fiber (ROF), mm-wave generation, wavelength conversion, pulse reshaping, multicasting, and un-cooled transmitters.

Injection-locking has been used for radio-over-fiber applications [40]. Experimentally, a DFB laser was modulated with a 125 Mb/s digital signal multiplexed to an RF carrier of 18 GHz. Due to the injection-locking resonance frequency enhancement, narrow-band transmission at the sharp resonance frequency peak is possible. Using a similar approach, injection-locking has been applied in a CATV transmission experiment, demonstrating a slight performance (3 dB in CSO and CTB) with locking [41]. In the locked case only, the signals were first up-converted to the locked resonance frequency, which was ~18.5 GHz. The transmission results were compared to base-band free-running transmission.

Optical generation of millimeter-waves has been demonstrated by a sideband injection-locking technique [42-44], with sub-Hertz RF linewidths. Recently, it has been implemented in a monolithic two-laser device [45]. The two lasers are biased such that they are unlocked and detuned by 36 GHz. The follower laser is modulated at 12 GHz, and has a third harmonic at 36 GHz, which gives rise to locking at this spectral component. Monolithic integration has also shown a resonance frequency enhancement to 21 GHz [46].

Clocked decision, retiming and pulse shaping as well as wavelength conversion (32 nm) is demonstrated at 2.5 and 5 Gbit/s with bi-stable semiconductor lasers. It is also shown that switching is possible at 10 Gbit/s using the same mechanism [47].

A multi-wavelength WDM transmitter for use in multicasting applications was demonstrated using inter-modal injection-locking, where 8 modes in the FP laser were simultaneously locked [48].

Finally, we have proposed using injection-locking for use in an un-cooled transmitter, employing a tunable VCSEL [49, 50]. The tunable laser is used to tune the wavelength to approximately the correct wavelength, while injection-locking achieves wavelength stabilization as well as a performance enhancement (modulation bandwidth, distortion reduction).

1.3. Analog Fiber Communications

This section introduces the main considerations involved in designing analog fiber optic links. The system requirements are related to device parameters, which are important in this thesis as we are studying optical injection-locking impact on device performance for analog fiber communications.

1.3.1. Sub-carrier Multiplexing

The transmission technique used for CATV signal distribution is sub-carrier multiplexing (SCM). In this technique, multiple low bandwidth data signals are combined electronically, and simultaneously modulate the transmitter. The individual signals can be either analog or digital, and each signal modulates a unique carrier. Each signal amplitude is made to be small enough such that the total signal amplitude is compatible with the transmitter. The combined signals modulate the transmitter, are transmitted via fiber, detected, and de-multiplexed at the receiver. The link is shown in

Figure 6.

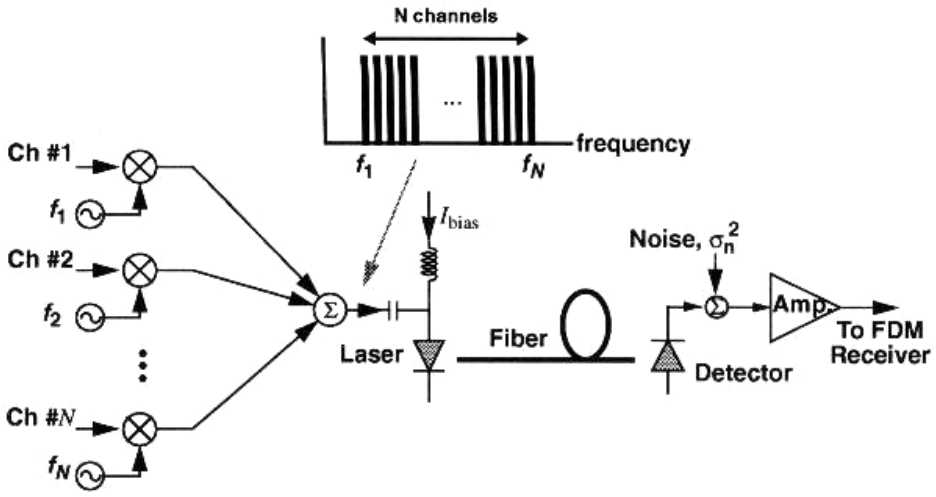

Figure 6 – Sub-carrier multiplexed transmission
(Figure from [51])

In sub-carrier multiplexed systems, there are several metrics to describe the performance of the link. Modulation index, signal-noise ratio, link gain, distortion, and dynamic range are the key parameters. These parameters are actually used for all analog links, not just SCM.

Modulation Index

For an N-channel sub-carrier system, the current applied to the transmitter is the sum of N individuals channels with signal *s(t)*, with modulation index *m*, frequency *w*:

$$i(t) = I_{bias}\left(1 + \sum_{n=1}^{N} m_n s_n(t)\cos(w_n t + f_n)\right) \tag{1.5}$$

For a large number of channels, by the central limit theorem, the input signal can be modeled as a Gaussian random variable with a standard variation of $m_{tot} I_{bias}$, where m_{tot} is the RMS modulation index:

$$m_{tot} = m\sqrt{\frac{N}{2}} \tag{1.6}$$

The total effective modulation index in a sub-carrier multiplexed system must be small enough so that clipping of the signal is not introduced. Typically, the effective modulation index is chosen to be < 0.26, with each channel modulation index to be ~ 0.02 [51].

1.3.2. Signal to Noise Ratio

Compared to digital systems, where a signal-to-noise ratio (SNR) of 10 dB is usually enough to yield a 10^{-9} bit error rate, analog sub-carrier multiplexed systems require an SNR that is typically larger than 50 dB. For amplitude modulated signals (AM-VSB), the signal-to-noise ratio is often replaced with the carrier-to-noise ratio

(CNR). The CNR is defined as the ratio of the RMS carrier power to the RMS noise power at the output of the photodetector. It can be written as

$$CNR = \frac{(mRP)^2/2}{\sigma_{shot}^2 + \sigma_{Th}^2 + \sigma_{RIN}^2 + \sigma_{Distortion}^2} \tag{1.7}$$

where m is the channel modulation index, R is the detector responsivity, P is the average received optical power, and σ_{shot}, σ_{Th}, σ_{RIN}, and $\sigma_{Distortion}$ are the RMS values of the noise currents associated with the shot noise, thermal noise, laser intensity noise, and distortion sources, respectively. $\sigma_{Distortion}$ depends on the transmitter distortions as well clipping distortion. Additionally, amplifiers in the link will contribute to the total noise.

$$\begin{aligned} \sigma_{shot}^2 &= 2q(RP + I_d)\Delta f \\ \sigma_{Th}^2 &= 4k_B T F_N \Delta f / R_L \\ \sigma_{RIN}^2 &= (RIN)(RP)^2 \Delta f \end{aligned} \tag{1.8}$$

To achieve a CNR of 50 dB, with a modulation index of m=0.03 (typical for a large number of channels), with a frequency band of 50 MHz, a laser with a RIN of -160 dB/Hz is required.

AM-VSB modulation is easy to implement, but has a very large CNR requirement. Alternatively, frequency modulation (FM) can be used. This relaxes the CNR requirement by providing an enhancement in the received SNR. For example, for an FM frequency factor of ~ 5, a ~39.5 dB improvement over the CNR was observed [52]. For such a system, an optical CNR of only 11 dB would be sufficient for CATV distribution, with a trade-off of added complexity in the transmitter/receiver.

1.3.3. Transmitter Noise

In a fiber optic link, the laser source used at the transmitter has noise, termed relative intensity noise. The noise will degrade the signal to noise ratio, as appears in (1.7). It is thus important to design a link with a low noise at the transmission frequency band.

Analog fiber transmission lasers are designed to have a low noise performance. For example, lasers manufactured by Ortel Inc. have a RIN < –165 dB/Hz [53].

For certain applications in RF links, noise figure is also important. The lowest reported noise figures are 17.8 dB for direct modulation [54] and 2.5 dB for external modulation [55].

1.3.4. Transmitter Distortion

This section discusses the distortion induced noise term in the CNR definition, equation (1.7). The origin of transmitter distortion depends on the transmitter type. For a semiconductor laser, the distortion physically originates from the nonlinear characteristics of the laser, including nonlinearity of the light-current (LI) curve, the carrier-photon interaction, or from spatial hole-burning [56, 57]. In a Mach-Zehnder interferometer modulator, the transfer function is sinusoidal, thus leads to distortion.

Transmitter distortion is extremely important for multi-channel systems, where

some of the power from interacting carriers can be transferred onto other channels. This leads to a reduction in the dynamic range of the system.

Spur-Free Dynamic Range

For an analog optical communication system, one most important figure of merit is the spur free dynamic range (SFDR), also known as intermodulation-distortion-free dynamic range. It is defined as dynamic range at the modulation power when the system noise floor equals the distortion noise [58], and gives the largest possible dynamic range of a given link. This quantity takes into account both the distortion and noise of a transmitter, hence is often used to describe the performance of a transmitter.

The largest SFDR measured for fiber-optic links is 128 $dB/Hz^{2/3}$ for a directly modulated laser source [59], and 132 $dB/Hz^{2/3}$ for an externally modulated source [60]. Short wavelength VCSELs have been used for analog transmission, and the highest SFDR reported is 98 $dB/Hz^{2/3}$ at 1.0 GHz for a 980 nm VCSEL [58]. For 850 nm VCSELs, the highest SFDR is 113 dB $Hz^{2/3}$ at 0.9 GHz [61]. A 1.55 um VCSEL was measured to have an 81 dB $Hz^{2/3}$ SFDR at 1.0 GHz [62].

Electro-absorption modulators using the quantum-confined stark effect or the Franz-Keldysh effect have been used for analog transmitters. The highest achieved SFDR is 124 dB $Hz^{4/5}$ [63] with the Franz-Keldysh effect. Using both effects has been proposed to increase linearity [64].

Linearization of transmitters

For applications where the device linearity is not high enough, techniques have been developed to linearize the transmitter.

Pre-distortion is the most common technique used. A circuit at the transmitter applies a distortion that is equal but opposite to the transmitter distortion, leading to a distortion cancellation. This results in the overall system that is much more linear. Pre-distortion has been applied to the linearization of LED transmitters [65], laser transmitters for CATV [66], for laser transmitters for radio-over-fiber systems between 0.2 – 2 GHz [67], and for Mach-Zehnder modulators. The pre-distortion circuits must be matched to the individual laser or modulator.

Feed-forward compensation is another method of achieving linearization. The circuit implementation is more complicated and can be difficult to implement since it requires two lasers, a detector, and microwave devices. It offers several advantages, including broadband distortion reduction, possible distortion reduction of all orders, non-linear characteristics of the laser do not need to be known [68], and can simultaneously reduce RIN [69]. A 10 dB reduction in the intermodulation distortions was observed using this technique [68]. Also, a 10 dB RIN decrease between 1.7-3 GHz was demonstrated [70].

Optical injection locking has been shown to be an effective technique for reduction distortion [18, 71, 72]. M. C. Wu, et. al. [18] have performed injection locking experiments for analog applications using DFB lasers. They found that at 2 GHz, the injection locked laser exhibited an IMD3 power reduction of 15 dB, leading to a 5 dB increase in SFDR. The SFDR in this case increased from 95 $dB/Hz^{2/3}$ to 100 $dB/Hz^{2/3}$.

1.4. Thesis Organization

This thesis describes the optical injection locking technique for analog fiber communication applications.

Chapter 2 presents the theory of injection locking, with the derivation of the injection-locking rate equations and modulation models. The derivation presents an understanding of the important parameters in the model, especially the coupling coefficient, k_c.

Chapter 3 describes theoretical and experimental work on small-signal modulation. The resonance frequency enhancement is studied for the various injection conditions, identifying the best parameters for the enhancement. Very high resonance frequencies are experimentally reported.

Chapter 4 focuses on laser noise, and the possibility of reducing the noise in the presence of injected light. Theoretical and experimental investigations demonstrate a very large reduction in the noise near the free-running laser resonance frequency, as well as for low frequency. Injection-locking thus enables a large frequency band with lower noise.

In Chapter 5, laser distortions are studied. It is shown that injection locking can reduce the non-linear laser distortions for a large frequency band. The distortion is characterized with system level measurements in mind by considering the spur-free dynamic range of the VCSEL. In particular, injection-locking can greatly increase the dynamic range.

Chapter 6 proposes the use of tunable VCSELs as an un-cooled transmitter. Injection-locking not only stabilizes the wavelength over an ambient temperature range, but improves the performance of the laser in terms of an enhancement in small signal modulation and a reduction in non-linear distortions. Next, isolator-free injection-locking is investigated.

Finally, Chapter 7 presents concluding remarks.

Chapter 2 Injection-Locking Theory

2.1. Injection-Locking Rate Equations

The derivation of the injection-locked rate equations presented in this section follows the traveling wave approach presented in [73] to derive the spatially-averaged free-running rate equations. However, for injection-locking, the electric field rather than photon density must be considered since there is a coupling of external light. Additionally, the boundary conditions are modified to include the external light injection.

In our derivation, we start with Maxwell's wave equation:

$$\nabla^2 \bar{E} - me \frac{\partial^2}{\partial t^2} \bar{E} - m \frac{\partial^2}{\partial t^2} \bar{P} = 0 \tag{2.1}$$

We let the electric field be defined by a time and space sinusoidal varying component multiplied by an undetermined function E(x,y):

$$\bar{E} = E(x, y) e^{i(wt - kz)} \tag{2.2}$$

The slowly-varying wave approximation is used on E(x,y), where

$$\frac{\partial^2}{\partial z^2} \ll k \frac{\partial}{\partial z}, \frac{\partial^2}{\partial t^2} \ll w \frac{\partial}{\partial t}$$

The E-field (2.2) is substituted in to (2.1)

$$\begin{aligned} \left(\frac{\partial}{\partial z} + \frac{n}{c} \frac{\partial}{\partial t} \right) E(x, y) &= im / k e^{-i(wt - kz)} \frac{\partial^2}{\partial t^2} \bar{P} \\ &= \tfrac{1}{2} cg(N) E \end{aligned} \tag{2.3}$$

Next, we model the laser using the traveling wave approach, as shown in Figure 7. There are two traveling waves in the cavity, described by the complex electric field amplitudes E^- and E^+, traveling in the left and right direction respectively. An external electric field is incident on the right facet. The cavity length is L.

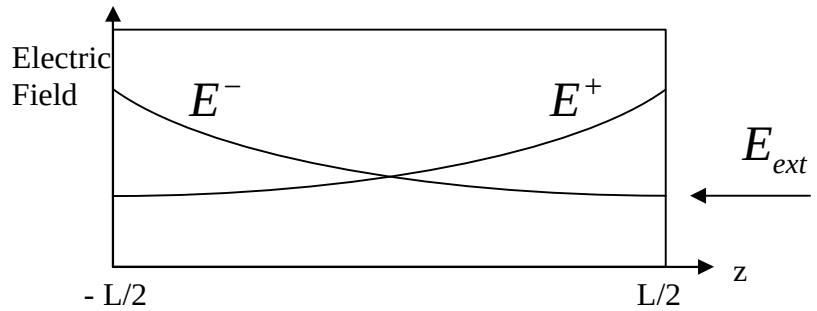

Figure 7 – Traveling wave model for rate equation derivation

We describe the traveling E-field as two functions:

$$\begin{aligned} \bar{E}^+ &= E^+(x, y) e^{i(wt - kz)} \\ \bar{E}^- &= E^-(x, y) e^{i(wt + kz)} \end{aligned} \tag{2.4}$$

The electric field grows in both directions, and is reflected at each facet. Optical injection is provided by the external field. We write two equations for propagating waves

in the left and right direction. We neglect spontaneous emission, and re-write the material polarization as an optical gain function.

$$\begin{aligned}\frac{\partial E^+}{\partial t}+c\frac{\partial E^+}{\partial z}&=\tfrac{1}{2}cg\left(N\right)E^+\\ \frac{\partial E^-}{\partial t}-c\frac{\partial E^-}{\partial z}&=\tfrac{1}{2}cg\left(N\right)E^-\end{aligned} \tag{2.5}$$

where E^+ and E^- are the forward and backward propagating electric fields, N is the carrier density, c is the group velocity of the waveguide mode, *g(N)* is the optical gain, *z* is the distance along the active medium with *z = 0* at the center of the laser.

2.1.1. Lasing at the Fabry-Perot condition

The first case we discuss is that where the lasing wavelength matches a fabry-perot cavity mode wavelength. In this condition, the round-trip phase is a multiple of 2 π, thus we have full constructive interference in the cavity. The externally injected light is also assumed to be in phase with the cavity mode.

We introduce the boundary conditions to take into account the reflectivity of the mirrors as well as incorporate the external injection field:

$$\begin{aligned}E^-\left(\frac{L}{2}\right)&=rE^+\left(\frac{L}{2}\right)+\sqrt{1-r^2}E_{ext}\\ E^+\left(\frac{-L}{2}\right)&=rE^-\left(\frac{-L}{2}\right)\end{aligned} \tag{2.6}$$

E_{ext} is the external injection electric field, r is the electric field reflectivity coefficient, and (1- r^2)E_{ext} is the optical field that penetrates the cavity. The reflectivity is assumed real (i.e. no phase change in the reflection). It is assumed that the injection field is small relative to the laser cavity field, as it leads to a difference in the forward and backward propagating waves.

Equations (2.5) are a set of differential equations with Equations (2.6) as the boundary values. It can be simplified tremendously and solved by spatially averaging over the length of the laser, to result in the spatially averaged injection-locked rate equations. The validity of this assumption is investigated by Moreno [74], and was shown to be valid for a reflection coefficient greater than 0.2.

$$\begin{aligned}\frac{dE^+*}{dt}+c\left(E^+\left(\frac{L}{2}\right)-E^+\left(\frac{-L}{2}\right)\right)&=\tfrac{c}{2}(g\left(N\right)E^+)*\\ \frac{dE^-*}{dt}-c\left(E^-\left(\frac{L}{2}\right)-E^-\left(\frac{-L}{2}\right)\right)&=\tfrac{c}{2}(g\left(N\right)E^-)*\end{aligned} \tag{2.7}$$

The * denotes the spatial average $\int_{-L/2}^{L/2}\frac{dz}{L}$. Equations (2.7) are added, the boundary conditions (2.6) applied, and the two electric field components are assumed symmetric about z = 0, and $E_T\left(z\right)=E^+\left(z\right)+E^-\left(z\right)$:

$$\frac{dE^+}{dt}*+\frac{dE^-}{dt}*+\frac{2c}{L}(1-r)E^+\left(\tfrac{L}{2}\right)-\frac{c}{L}\sqrt{1+r^2}E_{ext}=\tfrac{c}{2}(g(N)E^+)*+\tfrac{c}{2}(g(N)E^-)*$$

$$\frac{dE_T}{dt}*+\frac{2c}{L}\frac{1-r}{1+r}\left[E^+\left(\frac{L}{2}\right)+E^-\left(\frac{L}{2}\right)\right]-\frac{c}{L}\sqrt{1+r^2}E_{ext}=\tfrac{c}{2}(g(N)E_T)* \quad (2.8)$$

$$\frac{dE_T}{dt}*+\frac{2c}{L}\frac{1-r}{1+r}E_T\left(\frac{L}{2}\right)-\frac{c}{L}\sqrt{1+r^2}E_{ext}=\tfrac{c}{2}(g(N)E_T)*$$

This can be simplified, as done by Moreno, if we assume that both the E-field and gain are approximately constant throughout the cavity, $E=E_T\left(\tfrac{L}{2}\right)=\int_{-L/2}^{L/2}\frac{E_T(z)}{L}dz$, and $g(N)=\int_{-L/2}^{L/2}\frac{g(N,z)}{L}dz$:

$$\frac{dE}{dt}+\frac{2c}{L}\frac{1-r}{1+r}E-\frac{c}{L}\sqrt{1-r^2}E_{ext}=\tfrac{c}{2}g(N)E \quad (2.9)$$

Solving this equation in steady state gives the E field inside the cavity due to the external field E_{ext}. For example, it gives $E = 28\ E_{ext}$, for $R = 0.99$. This verifies that for a high Q resonator, the E-field inside the cavity can be much higher than the incident E-field.

The E-field rate equation typically used for the injection-locked analysis [10] is

$$\frac{dE(t)}{dt}=\left[jw_n(n)+\frac{1}{2}\left(g(n)-\frac{1}{t_p}\right)\right]E(t)+k_cE_{inj}(t)+E_n(t) \quad (2.10)$$

In this equation, the term *jw(t)* is included since *E(t)* is the actual electric-field in the cavity as a function of time. The difference between the results of our analysis (2.9) and (2.10) is that our electric-field is only the complex electric field amplitude, thus no *jw(t)* appears.

Next, we assume that the electric field is properly normalized such that $|E(t)|^2=S$, where S is the photon number. We can express the electric field description (2.9) in terms of the photon number:

$$\frac{dS}{dt}=\frac{d}{dt}\left(E\,\bar{E}\right)=2\mathrm{Re}\left\{\bar{E}\,\frac{dE}{dt}\right\} \quad (2.11)$$

Where $\bar{E}$ is the complex conjugate of the field E. We assume that the external electric field is at the same optical frequency as the follower laser, i.e. the system is injection-locked, and introduce the phase difference between the two fields as $f(t)$, resulting in:

$$\frac{dS}{dt}=\left(cg(N)-\frac{4c}{L}\frac{1-r}{1+r}\right)S+\frac{2c}{L}\sqrt{1-r^2}E_{ext}E\cos(f(t)) \quad (2.12)$$

$$\frac{dS}{dt}=\left(cg(N)-\frac{1}{t_p}\right)S+2k_c\sqrt{S_{inj}S}\cos(f(t)) \quad (2.13)$$

where

$$\frac{1}{t_p}=\frac{4c}{L}\frac{1-r}{1+r},\ \mathrm{R}=\mathrm{r}^2,\ k_c=\frac{\sqrt{2}c}{L}\sqrt{1-R} \quad (2.14)$$

2.1.2. Photon Lifetime

Equation (2.13) has the same form as the previously published rate equation, where the photon lifetime is $\frac{1}{t_p} = \frac{4c}{L}\frac{1-r}{1+r} \approx \frac{c}{L}\ln\left(\frac{1}{R}\right)$, assuming r ~ 1, where $R = r^2$ is the power reflectivity. This derivation matches to the classical definition of the photon lifetime: $\frac{1}{t_p} = \frac{c}{L}\ln\left(\frac{1}{R}\right)$. The comparison of the two definitions is shown in Figure 8, where the y-axis has been normalized to c/L. The classical definition is unbound for R ~ 0, whereas the definition derived here approaches 4. The definition derived here is only valid for R > 0.2, since for small R the gain will be non-uniform (and we have assumed uniform gain).

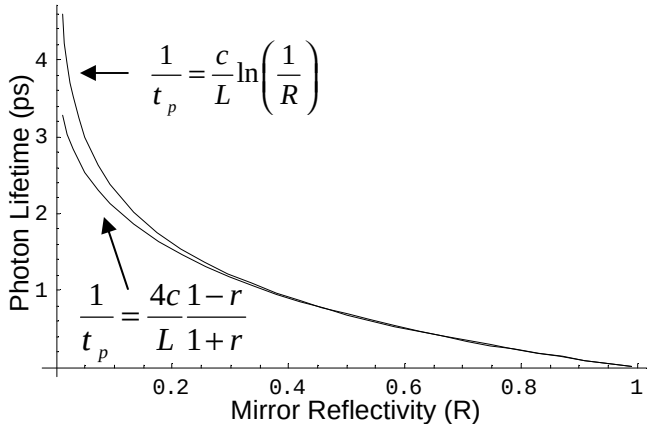

Figure 8 - Photon lifetime vs. mirror reflectivity

One can also carry out this same analysis for photon density rather than electric field. In this case, the difference is that the boundary conditions are stated in terms of power reflectivity, and the variables are photon density, rather than E-field. In this case, the analysis leads to a photon lifetime that yields the same value as the classical definition, in the limit of R ~ 1 [73].

2.1.3. Coupling Coefficient, k_c

The injection-locking rate equations previously published include a coupling coefficient, k_c. This coefficient describes the rate at which the injected electric field adds to the follower cavity electric field. In this section, we seek to understand the origin of this coefficient, and determine if the standard definition is applicable for high Q cavity lasers. What is the value of the coupling coefficient for VCSELs compared to edge-emitters? Would the multiple reflections from the high-reflectivity mirror contribute to an increased k_c?

The early k_c definition used by R. Lang [10] assumes a simple description of the propagating wave model, where the external field adds to the internal field every time it

hits the irradiated facet at a time interval of $t_R = 2nL/c$, which is the cavity round-trip time. Thus, $k_c = \frac{c}{2L}$. Reflectivity of the laser facets is not taken into account.

Shunk and Petermann [19] define the k_c constant in a similar fashion, but consider the time interval which is the cavity round trip time normalized by the photon decay, i.e. the cavity lifetime $t_R / \ln\left(1/R\right) = 2nL \Big/ c\ln\left(1/R\right)$. Taking into account the mirror (power) reflectivity, the k_c is thus defined as $k_c = \frac{c}{2nL}\ln\left(\frac{1}{R}\right) \approx \frac{c}{2nL}\frac{1-R}{\sqrt{R}}$.

Finally, most publications use $k_c = \frac{c}{2L}h$, where η is the coupling of the external to internal electric-fields. It is usually left unspecified, except by Mogensen [23] and Li [35], where it is defined as $h = \sqrt{1-R}$. This definition is similar to our derived definition, but with a differing factor of 2.

The injection-locking coupling coefficient derived using this analysis is $k_c = \frac{c}{L}\sqrt{1-r^2} = \frac{c}{L}\sqrt{1-R}$.

The results are summarized in Table 1, assuming an index of refraction of *n=3*, for a typical edge-emitting laser (EEL) and a typical vertical cavity laser (VCSEL). The assumed dimensions are typical values, and given in the table. The definition derived here yields similar values for the k_c coefficient as the previously published values for low reflectivities. However, for the case of the high reflectivity VCSEL, the k_c expressions used give vastly different results. In particular, the k_c derived here, which takes into account the cavity effects, results in a significantly higher value than defined by Shunk-Peterman, by a factor of ~45.

	L	R	k_c Lang	k_c Shunk-Petermann	k_c Mogensen	**k_c Chrostowski**
EEL	300 um	0.3	1.7×10^{11}	2.1×10^{11}	1.4×10^{11}	**2.8×10^{11}**
VCSEL	1 um	0.998	5.0×10^{13}	1.0×10^{11}	2.2×10^{12}	**4.5×10^{12}**

Table 1 – Summary of published k_c expression values

2.1.4. Rate Equations for lasing detuned from Fabry-Perot condition

The analysis above is a solution to a boundary value problem which includes multiple reflections. The spatial-average assumed that the reflection coefficient was greater than ~ 0.2, thus, it is thus an accurate description of a laser with injection-locking for both edge emitting lasers (R ~ 0.3) and VCSELs (R ~ 0.99). This description did not include cavity phase effects, thus it is only valid for the zero frequency detuning case. It may not apply for the general case of non-zero detuning. For non-zero detuning, the cavity phase would lead to a reduction in the cavity Q, thus a reduction in the photon lifetime.

The second case we discuss is that where the lasing wavelength doesn't match a Fabry-Perot cavity mode wavelength. In this condition, the round-trip phase is not a

multiple of 2π, thus we have some destructive interference in the cavity.

Effectively, we model the cavity to have shifted its Fabry-Perot center wavelength relative to the lasing wavelength. In this case, we model the reflectivity as a complex number, with amplitude to be the original reflectivity and phase, J, to correspond to a detuning in the lasing wavelength compared to the Fabry-Perot mode.

$$r' = re^{iJ} \tag{2.15}$$

We modify the boundary conditions to take into account the complex reflectivity of the mirrors as well as incorporate the external injection field (assumed in phase):

$$\begin{aligned} E^{-}\left(\frac{L}{2}\right) &= re^{iJ}E^{+}\left(\frac{L}{2}\right) + \sqrt{\left(1-r^2\right)}E_{ext} \\ E^{+}\left(\frac{-L}{2}\right) &= re^{iJ}E^{-}\left(\frac{-L}{2}\right) \end{aligned} \tag{2.16}$$

Solving the traveling wave equations (2.5) with the boundary conditions (2.16), we obtain a similar result:

$$\frac{dE}{dt} + \frac{2c}{L}\frac{1-re^{iJ}}{1+re^{iJ}}E - \frac{c}{L}\sqrt{1-r^2}E_{ext} = \tfrac{c}{2}g\left(N\right)E \tag{2.17}$$

Expressing this rate equation as a photon number rate equation, we find that the photon lifetime is now:

$$t_p = \frac{L}{4c}\left|\frac{1+re^{iJ}}{1-re^{iJ}}\right| \approx \frac{L}{4c}\mathrm{Re}\left\{\frac{1+re^{iJ}}{1-re^{iJ}}\right\},\ where\ J = 2p\,L\frac{l_o - l}{l_0^{\,2}} \tag{2.18}$$

For a reflectivity coefficient of r = 0.999, an effective cavity length of L = 3.1 μm, with an index of refraction n=3, we plot the photon lifetime, as a function of the lasing wavelength, in Figure 9. The center wavelength is λ_o = 1.55 μm, and the calculation is shown for a typical injection detuning range of -0.1 nm < detuning < 0.5 nm. As shown in the plot, the photon lifetime decreases by about ½ for the largest negative detuning. Not considered in this analysis is the fact that the index of refraction in the locked laser increases as the carrier density changes. Thus, for positive wavelength detuning, the cavity will be much closer aligned to the lasing wavelength than is shown in the figure.

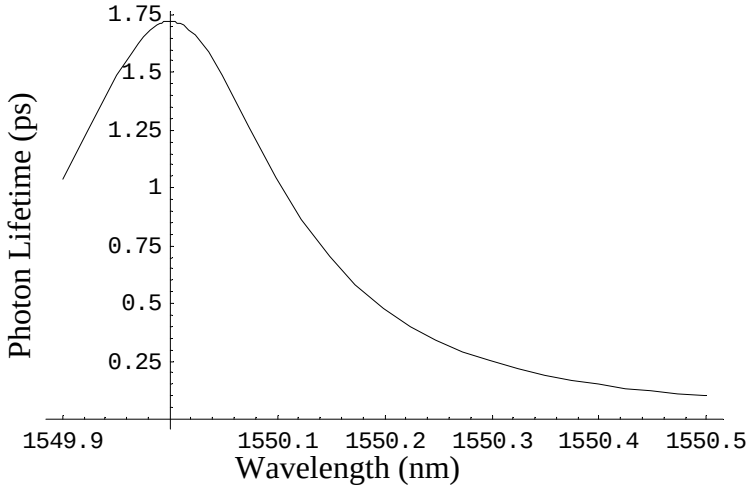

Figure 9 - Photon lifetime vs. lasing wavelength

An accurate injection-locking model of a VCSEL should actually have a photon lifetime that varies with the locking condition. The photon lifetime would be a functional form of equation (2.18), which considers the detuning between the cavity wavelength and the lasing wavelength. Such an analysis would greatly increase the numerical complexity in solving the rate-equations. It is expected that a decreased photon lifetime would contribute to the increase the resonance frequency of the laser due to locking.

In summary, injection-locking of a high-Q cavity such as a VCSEL can be modeled by using the constant coupling coefficient, equation (2.14), along with the photon lifetime, which varies with the detuning conditions, equation (2.18).

2.1.5. Injection Efficiency

The typical definition of injection-efficiency is:

$$inj\_eff = \frac{S_{inj}}{S_0} \tag{2.19}$$

This definition is intuitive when considering an edge-emitting laser with R = 0.3. In this case, the cavity has a very low Q, and since the reflectivity is low, the photon number that enters the cavity will be approximately the same as the photon number that is injected and is incident on the outside mirror. In the case of a high Q resonator, the injected optical field, E_{inj}, enters the cavity as $\sqrt{1-r^2}\,E_{inj}$. Thus, for a VCSEL, the definition of injection-efficiency is confusing, since it is unclear if one should use the injected field inside or outside of the cavity. For clarity, the injection efficiency will not be used. Rather, the optical injected photon number S_{inj} will be used to describe the injection ratio.

$$injection\ ratio = \frac{S_{inj}}{S_0} \tag{2.20}$$

In numerical simulations, describing the photon density inside cavities is equivalent to the photon densities outside the cavities, since the lasers are identical in the simulations. Experimentally, we actually measure the external photon densities, and the injection ratio should be consistent with definition (2.20).

2.2. Steady-state solution to the rate equations

The analysis presented in this section begins with the injection-locked rate equations:

$$\begin{aligned}
\frac{dS}{dt} &= \frac{G_0\left(N-N_{tr}\right)}{1+eS}\cdot S - \frac{S}{t_p} + 2k_c\sqrt{S\cdot S_{inj}}\cdot\cos\left(\Delta f\left(t\right)\right) + R_{sp} + F_s \\
\frac{df}{dt} &= \frac{a}{2}G_0\left(N-N_{th}\right) - \Delta w - k_c\sqrt{\frac{S_{inj}}{S}}\cdot\sin\left(\Delta f\left(t\right)\right) + F_f \\
\frac{dN}{dt} &= \frac{I}{q} - \frac{N}{t_s} - \frac{G_0\left(N-N_{tr}\right)}{1+eS}\cdot S + F_n
\end{aligned} \tag{2.21}$$

The terms F_s, F_f, F_n are the noise Langevin forces, and $\Delta f\left(t\right) = f_{inj} - f(t)$ is the phase

difference between the incident injection light and the follower laser field. The injection-locking detuning between the master and free-running follower lasers can be described either by a wavelength detuning ($\Delta\lambda$) or by a frequency detuning ($\Delta\omega = 2\pi\Delta f$). The wavelength and frequency detunings are related by:

$$f_o = \frac{c}{l_o}$$
$$\Delta l\ (\text{detuning}) = \frac{c}{f_o} - \frac{c}{f_o - \Delta f\ (\text{detuning})} \tag{2.22}$$

The injection-locking rate equations are first solved in the steady-state to determine the region of stability, and to solve for the steady-state parameters. Setting the time-varying terms in the photon and phase differential equations, in (2.21), we obtain:

$$0 = \frac{G_0(N - N_{tr})}{1 + eS} \cdot S - \frac{S}{t_p} + 2k_c\sqrt{S \cdot S_{inj}} \cdot \cos(\Delta f) + R_{sp} + F_s$$
$$0 = \frac{a}{2} G_0\left(N - N_{th}\right) - \Delta w - k_c\sqrt{\frac{S_{inj}}{S}} \cdot \sin(\Delta f) + F_f \tag{2.23}$$

Assuming the system is stabily locked, the phase relation between the master and follower lasers is constant, which we denote as $\Delta f = f_{inj} - f(t)$. Next, we approximate the gain by removing the gain compression, and define Nth as the clamped carrier density of the free-running laser,

$$\frac{G_0(N - N_{tr})}{1 + eS} \cdot S - \frac{S}{t_p} \approx G_0\left(N - N_{th}\right) \cdot S \tag{2.24}$$

Solving (2.23) for the frequency detuning Δw,

$$\Delta w = k_c\sqrt{\frac{S_{inj}}{S}}\sqrt{1 + a^2}\,\sin\left(\Delta f - \tan^{-1} a\right) \tag{2.25}$$

Alternatively, we can solve for the phase difference, as a function of frequency detuning and injection power.

$$\Delta f = \sin^{-1}\left(\frac{\Delta w}{k_c\sqrt{S_{inj}/S}\sqrt{1 + a^2}}\right) + \tan^{-1} a \tag{2.26}$$

2.2.1. Locking Range

Following the discussion in [25], we can describe the locking bandwidth of the system. From (2.25), we can see that due to the sin term, the system is limited to a range of:

$$|\Delta w| \le k_c\sqrt{\frac{S_{inj}}{S}}\sqrt{1 + a^2} \tag{2.27}$$

However, since injection-locking increases the stimulated emission, it decreases the carrier number and decreases the gain. Thus, if it is assumed that the gain change in the follower laser cavity can only be negative, we find a second restriction on the locking bandwidth. The phase is bound by

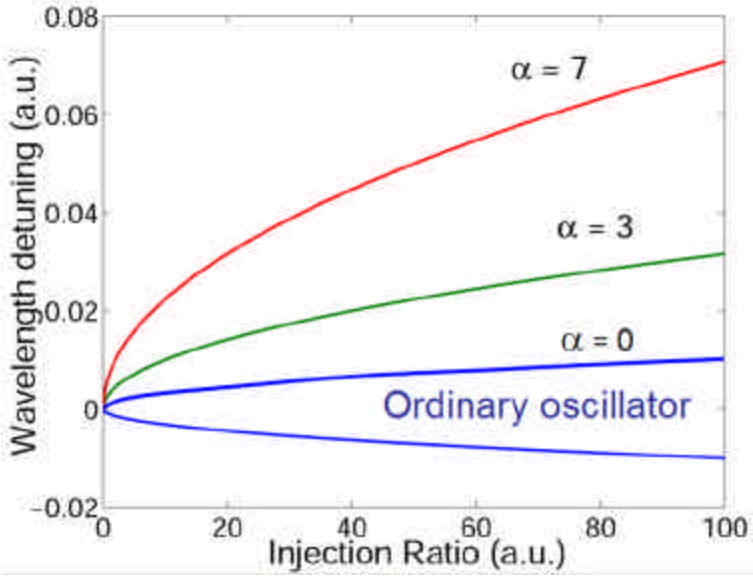

Figure 10 – Analytic injection-locking stability plot
Injection ratio is in arbitrary units, plotted in the linear scale.

$$|\Delta f| \le \frac{p}{2} \tag{2.28}$$

This leads to a reduced locking range, given by:

$$-k_c\sqrt{\frac{S_{inj}}{S}}\sqrt{1+a^2} \le \Delta w \le k_c\sqrt{\frac{S_{inj}}{S}} \tag{2.29}$$

The locking range for various α parameters is plotted in Figure 10. The locking range is asymmetric due to the change in index of refraction when the system is locked. This leads to a cavity wavelength shift in the longer wavelength direction, and finally an asymmetric locking range.

The locking range given by equation (2.29) is approximate, since it does not consider long-term stability of the system due to perturbations. Such an analysis has been performed in [25]. Numerical solutions to determine the stability can also be performed. Figure 11 shows the results of such a simulation. For locking to be stable, the wavelength must match the master wavelength, and the photon and electron numbers much reach a steady-state. The simulations were performed for a linewidth enhancement factor of α=3. In the figure, the injected power is plotted in logarithmic units. For low injection powers, it is seen that stable locking is not possible for a 0 detuning, as predicted by equation (2.29). Indeed, in early experimental demonstrations of injection-locking using edge-emitting lasers, locking was only observed for a small negative frequency detuning.

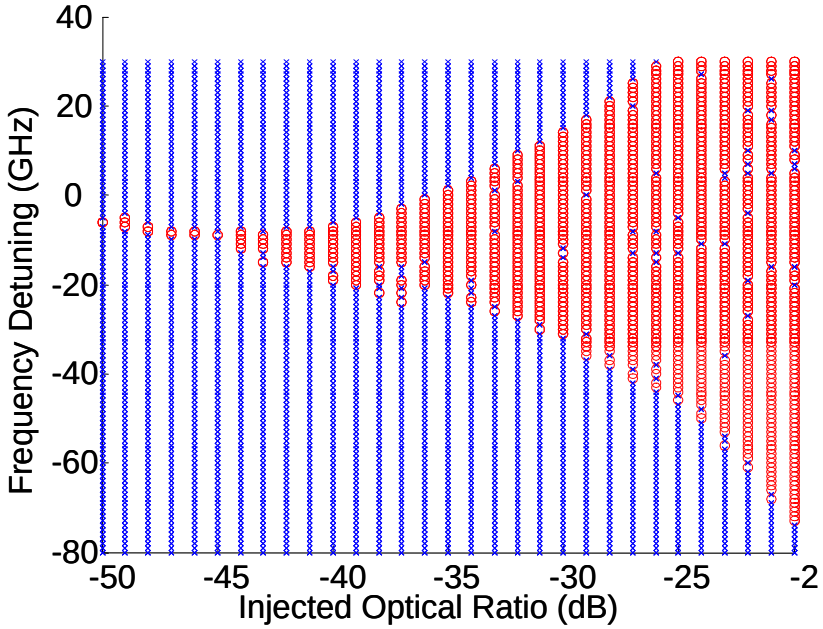

Figure 11 - Numerically simulated injection-locking stability plot.

2.2.2. Locking Mechanism

In a semiconductor, the locking mechanism is more complicated that in RF oscillators. In an RF oscillator, the locking range is symmetric. In a semiconductor, the linewidth enhancement factor leads to an asymmetry in locking. As shown by Lang [10], the carrier density in the active region of an injection-locked laser is reduced. This leads to an increase in the index of refraction, which gives rise to a decrease in the cavity resonance frequency (increase in wavelength). This leads to locking that prefers the longer wavelengths.

In the VCSEL, the cavity is a very high Q resonator. This leads to the question of how it can be possible for this laser, when locked, to lase at an off-resonance condition, where the round-trip phase is not 2π. As shown in the k_c derivation, this leads to an effective increase in the cavity loss. This increases the gain required for lasing (threshold gain, g_{th}). In the injection-locked system, the external light reduces the required gain for lasing (since there are now additional photonics); the laser will lock to the master only if the new threshold gain is low enough to sustain lasing oscillations. For too high a detuning, the injection-locked threshold gain will be too high and the laser will be unlocked, preferring the unlocked on-resonance condition.

In edge-emitter lasers, the cavity has a very small Q, thus the cavity does not play a major role in the locking analysis. For the case of a high Q resonator, the locking range will be reduced. In the case of a VCSEL, the linewidth of a cold cavity resonator is approximately 1 nm, which is larger than the typical injection-locking range, hence the high-Q should not limit the locking range.

2.3. Small-signal analysis of injection-locked rate equations

Equations (2.21) are used as the starting point for all injection-locking simulations

and analytic solutions. In this section, a small-signal analysis is performed, to derive the laser RIN and small-signal modulation response.

We begin by assuming a steady-state value for each of the variables with a small-signal modulation term, at the electrical frequency ω. The steady-state values are denoted with the 0 subscript.

$$\begin{aligned} &F_s = F_s(w)e^{iwt},\ F_f = F_f(w)e^{iwt},\ F_N = F_N(w)e^{iwt} \\ &S = S_0 + S_1(w)e^{iwt},\ f = f_0 + f_1(w)e^{iwt},\ N = N_0 + N_1(w)e^{iwt} \end{aligned} \tag{2.30}$$

Substituting (2.30) into (2.21), we find the small signal terms to be:

$$\begin{aligned} iw\,S_1(w)e^{iwt} = &\frac{G_0\left(N_0 + N_1(w)e^{iwt} - N_{tr}\right)}{1 + e\left(S_0 + S_1(w)e^{iwt}\right)} \cdot \left(S_0 + S_1(w)e^{iwt}\right) - \frac{S_0 + S_1(w)e^{iwt}}{t_p} \\ &+2k_c\sqrt{\left(S_0 + S_1(w)e^{iwt}\right)\cdot S_{inj}}\cdot\cos\left(f_0 + f_1(w)e^{iwt} - f_{inj}\right) + R_{sp} + F_s(w)e^{iwt} \end{aligned} \tag{2.31}$$

$$\begin{aligned} iw\,f_1(w)e^{iwt} = &\frac{a}{2}G_0\left(N_0 + N_1(w)e^{iwt} - N_{th}\right) + \left(w_0 - w_{inj}\right) \\ &-k_c\sqrt{\frac{S_{inj}}{\left(S_0 + S_1(w)e^{iwt}\right)}}\cdot\sin\left(f_0 + f_1(w)e^{iwt} - f_{inj}\right) + F_f(w)e^{iwt} \end{aligned} \tag{2.32}$$

$$\begin{aligned} iw\,N_1(w)e^{iwt} = &\frac{I}{q} - \frac{N_0 + N_1(w)e^{iwt}}{t_s} \\ &-\frac{G_0\left(N_0 + N_1(w)e^{iwt} - N_{tr}\right)}{1 + e\left(S_0 + S_1(w)e^{iwt}\right)}\cdot\left(S_0 + S_1(w)e^{iwt}\right) + F_n(w)e^{iwt} \end{aligned} \tag{2.33}$$

We expand (2.31)-(2.33), and use the following approximations (i.e. first order Taylor expansions) to solve the photon number equation:

$$\frac{1}{1 + e\left(S_0 + S_1(w)e^{iwt}\right)} \approx \frac{1}{1 + eS_0}\left(1 - \frac{S_1(w)e^{iwt}}{1 + eS_0}\right)$$

$$\frac{1}{1 + e\left(S_0 + S_1(w)e^{iwt}\right)} \approx \frac{1}{1 + eS_0}\left(1 - \frac{eS_1(w)e^{iwt}}{1 + eS_0}\right) \tag{2.34}$$

$$\cos(A + x) \approx \cos(A) - \sin(A)\,x \tag{2.35}$$

$$\sqrt{\left(S_0 + S_1(w)e^{iwt}\right)\cdot S_{inj}} \approx \sqrt{S_0 S_{inj}} + \frac{S_1(w)e^{iwt}}{2}\sqrt{\frac{S_{inj}}{S_0}} \tag{2.36}$$

Only considering the small-signal modulation terms in (2.31) for the photon part,

$$\begin{aligned} iw\,S_1(w) = &\frac{G_0(N_0 - N_{tr})}{1 + eS_0}S_1(w)\left(1 - \frac{eS_0}{1 + eS_0}\right) + \frac{G_0 N_1(w)}{1 + eS_0}S_0 - \frac{S_1(w)e^{iwt}}{t_p} \\ &+2k_c\left(\sqrt{\frac{S_{inj}}{S_0}}\frac{S_1(w)}{2}\cos\left(f_0 - f_{inj}\right) - \sqrt{S_0 S_{inj}}\sin\left(f_0 - f_{inj}\right)f_1(w)\right) + F_s(w) \end{aligned} \tag{2.37}$$

Similarly, for the phase term, considering the small-signal modulation terms in (2.31), and using the following approximations,

$$\sqrt{\frac{A}{B+x}} \approx \sqrt{\frac{A}{B}}\left(1-\frac{A}{2B}x\right), \sqrt{\frac{S_{inj}}{\left(S_0+S_1(w)e^{iwt}\right)}} \approx \sqrt{\frac{S_{inj}}{S_0}}\left(1-\frac{S_{inj}}{2S_0}S_1(w)e^{iwt}\right) \quad (2.38)$$

$$\sqrt{\frac{A}{B+x}} \approx \sqrt{\frac{A}{B}}\left(1-\frac{x}{2B}\right), \sqrt{\frac{S_{inj}}{\left(S_0+S_1(w)e^{iwt}\right)}} \approx \sqrt{\frac{S_{inj}}{S_0}}\left(1-\frac{S_1(w)e^{iwt}}{2S_0}\right) \quad (2.39)$$

$$\sin(A+x) \approx \sin(A)+\cos(A)x \quad (2.40)$$

$$\begin{aligned} iw f_1(w) &= \frac{a}{2}G_0 N_1(w) \\ &-k_c\sqrt{\frac{S_{inj}}{S_0}}\left(-\frac{S_1(w)}{2S_0}\sin(f_0-f_{inj})+\cos(f_0-f_{inj})f_1(w)\right)+F_f(w) \end{aligned} \quad (2.41)$$

Finally, for the carrier term,

$$\begin{aligned} iw N_1(w) &= -\frac{N_1(w)e^{iwt}}{t_s}-\frac{G_0(N_0-N_{tr})}{1+eS_0}S_1(w)\left(1-\frac{eS_0}{1+eS_0}\right) \\ &-\frac{G_0 N_1(w)}{1+eS_0}S_0+F_n(w) \end{aligned} \quad (2.42)$$

Equations (2.37), (2.41), (2.42) can now be written in matrix form:

$$A\begin{bmatrix} S_1 \\ f_1 \\ N_1 \end{bmatrix} = \begin{bmatrix} F_S \\ F_f \\ F_N \end{bmatrix} \quad (2.43)$$

$$A = \begin{bmatrix} iw-\frac{G_0(N_0-N_{tr})}{1+eS_0}\left(1-\frac{eS_0}{1+eS_0}\right) & 2k_c\sqrt{S_0 S_{inj}}\sin(f_0-f_{inj}) & -\frac{G_0}{1+eS_0}S_0 \\ +\frac{1}{t_p}-k_c\sqrt{\frac{S_{inj}}{S_0}}\cos(f_0-f_{inj}) & & \\ -\frac{k_c}{2}\sqrt{\frac{S_{inj}}{S_0^3}}\sin(f_0-f_{inj}) & iw+k_c\sqrt{\frac{S_{inj}}{S_0}}\cos(f_0-f_{inj}) & -\frac{a}{2}G_0 \\ \frac{G_0(N_0-N_{tr})}{1+eS_0}\left(1-\frac{eS_0}{1+eS_0}\right) & 0 & iw+\frac{G_0}{1+eS_0}S_0+\frac{1}{t_s} \end{bmatrix} \quad (2.44)$$

This matrix can be inverted to provide the solution for the small-signal variables, where in this case, S_1 is the laser RIN, ϕ_1 describes the laser linewidth, and N_1 is the noise in the electron population.

$$\begin{bmatrix} S_1 \\ f_1 \\ N_1 \end{bmatrix} = A^{-1}\begin{bmatrix} F_S \\ F_f \\ F_N \end{bmatrix} \quad (2.45)$$

Assuming the Langevin noise terms are white Gaussian random variables, the laser RIN will be given by:

$$RIN(w) = \left|S_1(w)\right| \tag{2.46}$$

The full analytic expression for RIN is extremely unwieldy, and needs to be evaluated numerically. In Chapter 4 numerical results using this model are presented, showing the noise spectra for the injection-locked laser.

The small-signal modulation response can also be found from this system by considering I as the small signal modulation current.

$$\begin{bmatrix} S_1 \\ f_1 \\ N_1 \end{bmatrix} = A^{-1} \begin{bmatrix} 0 \\ 0 \\ I \end{bmatrix} \tag{2.47}$$

The modulation response transfer function will be

$$H(w) = \frac{\left|S_1(w)\right|}{I(w)} \tag{2.48}$$

Based on the above analysis, the small signal modulation response of the injection-locked laser is found to be a polynomial with a denominator of 3rd order and a numerator of 1st order [75, 76]:

$$H(s) = A\frac{s + a_0}{s^3 + b_2 s^2 + b_1 s + b_0} \tag{2.49}$$

In this equation, s = jω, and the coefficients a_i and b_i are functions of the laser parameters and injection conditions. We define the gain as $g = G_0(N_0 - N_{tr})/(1 + eS_0)$, and we assume the differential of the gain with respect to the carrier and photon number is $dg = a_N dN - a_S dS$, where a_N is the differential gain, and a_S takes into account the gain compression. The analytic expressions for the coefficients a_i and b_i are given by:

$$a_0 = k_c\sqrt{\frac{S_{inj}}{S}}\left(\cos f - a\sin f\right) \tag{2.50}$$

$$\begin{aligned} b_0 = {} & -k_c a_N \sqrt{S_{inj} S}\left(a_S S - g\right)\left(\cos f - a\sin f\right) \\ & -\left(a_N S + 1/t_n\right)\left[\left(g - 1/t_p - a_S S\right)k_c\sqrt{\frac{S_{inj}}{S}}\cos f + k_c{}^2\frac{S_{inj}}{S}\right] \end{aligned} \tag{2.51}$$

$$b_1 = a_N S\left(a_S S - g\right) - k_c{}^2\frac{S_{inj}}{S} - \left(a_N S + 1/t_n + k_c\sqrt{\frac{S_{inj}}{S}}\cos f\right)\left(g - 1/t_p - a_S S\right) \tag{2.52}$$

$$b_2 = a_N S + 1/t_n - \left(g - 1/t_p - a_S S\right) \tag{2.53}$$

$$A = \frac{1}{q}a_N S \tag{2.54}$$

$$\text{where } f = -\sin^{-1}\frac{2p\Delta f}{k_c\sqrt{\frac{S_{inj}}{S}}\sqrt{1 + a^2}} - \tan^{-1} a \tag{2.55}$$

The transfer function polynomial can be factored and written in the pole (p_i) and zero (z_i) format:

$$H(s) \propto \frac{s - z_0}{(s - p_0)(s - p_1)(s - p_2)} \tag{2.56}$$

Because the coefficients a_i and b_i are all real, the poles and zero are found to be configured as shown in Figure 12. Two poles (p_1, p_2) are complex conjugates and these determine the resonance frequency and damping. One pole (p_0) and the zero (z_0) are real hence are found on the x-axis. The modulation frequency, s = jω, is shown on the y-axis.

The frequency response amplitude is found to be the distance from s to O position divided by the product of the distances from s to the X positions. The resonance frequency is the distance from the complex pole, X, to the origin. The damping is from the complex pole, X, to the y axis.

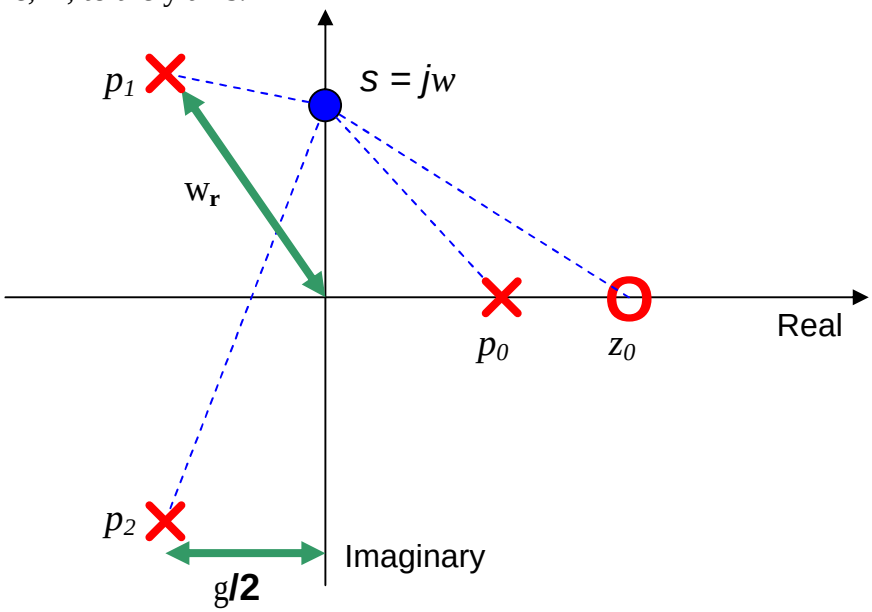

Figure 12 - Complex pole-zero plot for the transfer function polynomial

The frequency response of this system is simplified considerably when $S_{inj} = 0$ (i.e. no injected light). In this case, $a_0 = b_0 = 0$, and the frequency response in equation (2.49) is reduced to the familiar two-pole equation for a directly modulated laser, with a relaxation oscillation frequency f_r.

$$H(jw) = A\frac{1}{(jw)^2 + b_2(jw) + b_1} \tag{2.57}$$

$$f_r = (2p)^{-1}\sqrt{b_1} \sim (2p)^{-1}\sqrt{a_N S / t_p}$$

On the other hand, when S_{inj} / S is very large, b_0 becomes negligible compared to the other terms in the denominator of the transfer function, which is once again reduced to a two-pole function, $H(jw) = A\frac{jw + a_0}{\left[(jw)^2 + b_2(jw) + b_1\right](jw)}$. In the large injection ratio limit, the resonance frequency is approximately, and indicates that with strong injection f_r can be increased indefinitely:

$$w^2_r \approx w^2_{r,free-running} + k_c^2 \frac{S_{inj}}{S} \tag{2.58}$$

Indeed, our experimental work has shown that the resonance frequency can be increased by as much as a factor of 7 [77]. Simulation and experimental results are presented in Chapter 3 .

Inspection of the transfer function (2.56), we find that it can be re-written as:

$$\left|H(f)\right|^2 \propto \left[\frac{1-\left(\frac{f}{f_z}\right)^2}{1-\left(\frac{f}{f_p}\right)^2}\right] \frac{1}{\left(1-\left(\frac{f}{f_r}\right)^2\right)^2 + \left(\frac{g}{2p\, f_r}\right)^2 \left(\frac{f}{f_r}\right)^2} \tag{2.59}$$

In this equation, f_0 and f_n represent the pole and zero introduced by the injection, f_r is the resonance frequency and γ is the damping term. This form of the modulation response is useful for curve-fitting the experimental and numerically simulated small-signal modulation response curves, and will be used in Chapter 3 .

2.4. Harmonic distortion analysis

For free-running lasers, analytic harmonic distortion analyses have been conducted by considering small-signal modulation of the rate-equations, and solving for the higher order distortion terms [78]. This analysis has resulted in an analytic expression for intermodulation distortion. A similar analysis has been performed for the injection-locked rate equations [79], leading to complicated analytic formulations and predicted distortion responses.

Alternatively, distortion in the injection-locked laser can be analyzed by numerically solving the injection-locked rate equations. A single tone (or two tones) is input as a current modulation. The response of the laser is then Fourier-transformed, to yield the frequency information of the output light. The harmonic distortion power can be analyzed as a function of modulation frequency, and for varying injection parameters. This numerical analysis is carried out in Chapter 5 .

2.5. Summary

This chapter presented the derivation of the theoretical model used for injection-locking simulations. The injection-locked rate equations were derived using the traveling-wave approach with the addition of external light injection to the boundary conditions. It was found that the coupling coefficient derived is similar to the definition of $k_c = \frac{c}{2L}\sqrt{1-R}$ which is frequency used in the literature [23, 35]. The model was extended to take into account that the laser can be forced to lase at a wavelength detuned from the Fabry-Perot condition. It was found that for those cases, the photon lifetime is effectively reduced.

With the derived rate equations for injection-locking, a linear small-signal analysis was performed. From this analysis, the small-signal modulation response is found. It is found that the response can be described by the same expression as for a free-running laser, with an additional pole and zero to the transfer function. This expression can be

used for curve-fitting to the experimental results.

Chapter 3 Laser Frequency Response

The enhancement of the resonance frequency of semiconductor lasers due to injection-locking has been theoretically predicted [25, 80, 81] and experimentally verified [17, 18, 29, 82, 83]. The resonance frequency enhancements observed are typically a factor of 3 increase. The increased resonance frequency leads to a change in the small-signal frequency response, and in some conditions lead to an enhancement of the electrical bandwidth.

This chapter discusses the small signal frequency response of injection-locked lasers. Simulations based on the theoretical model presented will be discussed first, followed by several experiments performed. Two types VCSELs with different mirror design and one DFB type was characterized. Resonance frequency enhancement was observed for all devices tested.

3.1. Injection-Locking small-signal modulation simulations

3.1.1. Numerical simulations

This section describes the simulations performed by a numerical solution to the injection-locked rate equations. Although the simulations are more computationally time consuming than the analytic model presented in Chapter 2, the results are more accurate since they include the photon number and carrier number changes due to locking. Additionally, the numerical model does not include any small-signal approximations, thus can be used for large signal digital modulation. The simulation code was implemented in Matlab, and is shown in Appendix A.

The small signal modulation response was calculated using the injection-locked rate equations. For each frequency point, the rate equations were solved with an input sinusoid at that frequency. The small-signal amplitude was 0.1 times the threshold current. The simulation was performed in steady-state, to find the operation condition of the follower laser, then modulated for at least 2 ns (to allow the laser to stabilize). The last sinusoid cycle was used to determine the amplitude and phase, by curve-fitting to a sinusoid function.

The S21 response was curve-fitted to the injection-locked small signal response equation:

$$\left|H(f)\right|^2 \propto \left[\frac{1-\left(\frac{f}{f_z}\right)^2}{1-\left(\frac{f}{f_p}\right)^2}\right]\frac{1}{\left(1-\left(\frac{f}{f_r}\right)^2\right)^2+\left(\frac{g}{2p\,f_r}\right)^2\left(\frac{f}{f_r}\right)^2} \tag{3.1}$$

In this equation, f_p represents the 1st order pole introduced by the injection, f_z is the numerator zero frequency, f_R the resonance and γ the damping term. Equation (3.1) is applicable for both injection-locked and free-running small-signal responses.

For free-running lasers, the f_p term becomes very large (>> f_r) and does not contribute to the response. The numerator term is also negligible for the free-running

case. This equation is a third-order filter response with a canceling first-order numerator, hence has a 40 dB/decade roll-off for high frequencies. For the free-running cases, where the f_p and f_z terms is very large, the roll-off is 40 dB/decade, and the response is the normal free-running laser response, given by:

$$\left|H(f)\right|^2 = \frac{1}{\left(1-\left(\frac{f}{f_r}\right)^2\right)^2 + \left(\frac{g}{2p\,f_r}\right)^2\left(\frac{f}{f_r}\right)^2} \tag{3.2}$$

Figure 13 shows a typical S21 simulation, showing both the simulation data and the curve-fit data for free-running and injection-locked cases. The injection condition is an injection ratio of 0.0003 with detunings of 4 and -11 GHz. In this example, the free-running resonance frequency is 4.8 GHz with a damping of 26 GHz. The injection-locked resonance frequency increases to 7 and 10 GHz, for the 4 and -11 GHz detuning respectively, with corresponding damping of 15 and 43 GHz. Also, for both cases, the pole frequency is small than the zero frequency, i.e. $f_p < f_z$. The fitting parameters for the simulation data is shown in Table 2.

Parameter	Free-running	Injection Locked 4 GHz	Injection Locked -11 GHz
f_r	4.8	10.0	7.3
γ	26.2	15.3	43.1
f_p	74.6 (~ 8)	7.0	10.6
f_z	74.6 (~ 8)	30.0	23.4

Table 2 – Fitting parameters to numerically simulated small-signal response

Noting that f_z is typically much larger than f_r, we can neglect this term when we are only interested in the frequency response for frequencies near the resonance, say less than $2f_r$. Hence, the approximate formula for fitting can be:

$$\left|H(f)\right|^2 \propto \left[\frac{1}{1-\left(\frac{f}{f_p}\right)^2}\right]\frac{1}{\left(1-\left(\frac{f}{f_r}\right)^2\right)^2 + \left(\frac{g}{2p\,f_r}\right)^2\left(\frac{f}{f_r}\right)^2} \tag{3.3}$$

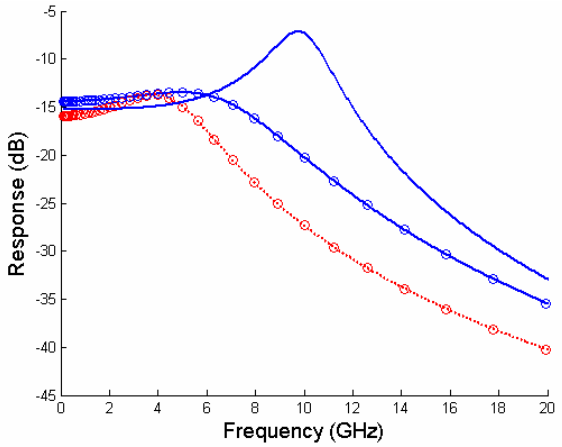

Figure 13 - Simulated amplitude frequency response
The injection ratio is 0.003 and the detuning values are 4 and -11 GHz.

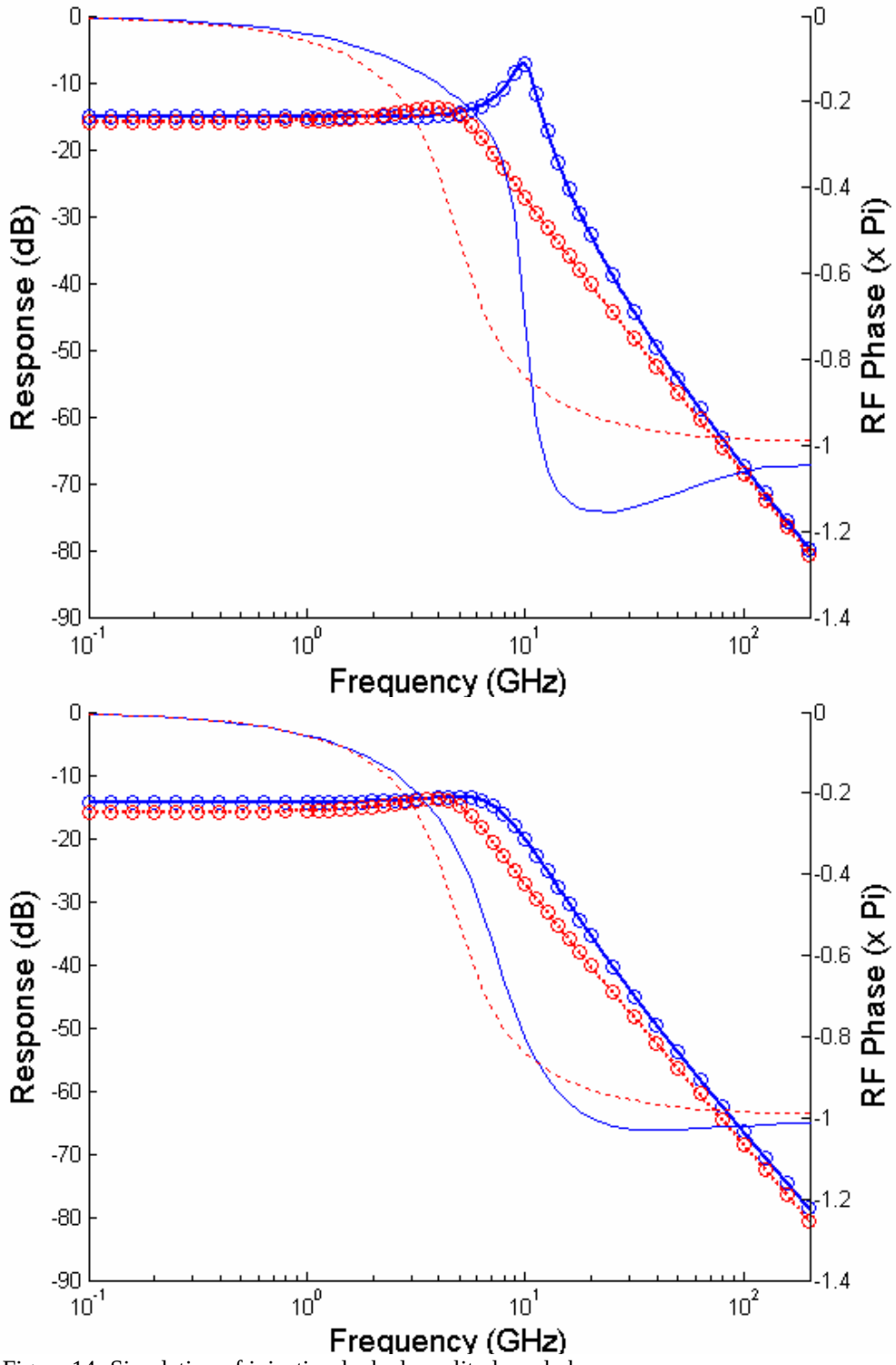

Figure 14- Simulation of injection-locked amplitude and phase response
The injection ratio is injection ratio 0.0003.
Detuning is 4 GHz (top plot), and -11 GHz (bottom plot).
The RF small-signal response is shown with traces having the "o" markers and thick lines (curve-fit). The RF phase response is the thin lines. The dotted lines are free-running, the solid lines are injection-locked.

Parameter	Units	Symbol	Value
Laser cavity length	cm	L	1×10^{-4}
Active region length	cm	L_a	24×10^{-7} 3 QWs 8nm each
Mesa size	cm^2	A	4×10^{-6}
Mirror reflectivity		R	0.998
Differential gain	cm^2	dgdn	2×10^{-16}
Differential gain (normalized)		$G = \Gamma\ dgdn\ v_g / AL_a$	7.65×10^{-6}
Confinement factor		$\Gamma = 2\ L_a/L$ 0.9	0.043
Gain compression factor		ε	20×10^{-8}
Group velocity	cm/ns	v_g	8.5
Carrier number at transparency		N_0	1.8×10^{18}
Carrier density at transparency	cm^{-2}	$N_{0,density}$	1.73×10^{7}
Current density at threshold	A/cm^2	J_{th}	1005
Carrier number at threshold		N_{th}	5.23×10^{18}
Carrier density at threshold	cm^{-2}	$N_{th,density}$	5.0×10^{7}
Carrier lifetime	ns	τ_s	2
Photon lifetime	ns	τ_p	2×10^{-3}
Linewidth enhancement factor		α	3 to 6
Spontaneous emission rate	ns^{-1}	R_{sp}	2×10^{3}
Master laser bias	mA	I_{master}	$4 \times I_{th}$
Follower laser bias	mA	I_{master}	$4 \times I_{th}$
Threshold current	mA	I_{th}	4
Coupling coefficient	ns^{-1}	$k_c = \sqrt{(1-R)}\ v_g /L$	3.8×10^{-3}

Table 3 – Typical simulation laser parameters

Phase Response

For the free-running laser, the RF phase response is similar to a typical two-pole response, where the phase decreases by $\pi/2$ for each pole. As can be seen in Figure 14, the phase remains nearly constant for frequencies below the resonance frequency. The phase changes abruptly near the resonance frequency, reaching its final value of $-\pi$ for high frequencies.

For the injection-locked cases, the phase response is similar, though the transition in phase is much more abrupt for positive detuning values (i.e. Figure 14b). The rate of transition where the phase changes from 0 to $-\pi$ is related to the damping term in the small-signal amplitude response. The high frequencies, the phase approaches $-\pi$, and experiences undershoot in the phase just above the resonance frequency.

Figure 14a shows the phase and amplitude response for free and injection-locked cases, for a 4 GHz detuning, with an injection ratio of 0.0003; Figure 14b shows the same plot but for a -11 GHz detuning. As seen in the figures, the small-signal response features a sharp peak response for the 4 GHz detuning, with a highly damped response for the -11 GHz. The increase in the damping rate for negative frequency (positive wavelength) detuning has been attributed to gain change in a locked laser [81], and is seen in the analytic expression for the modulation response.

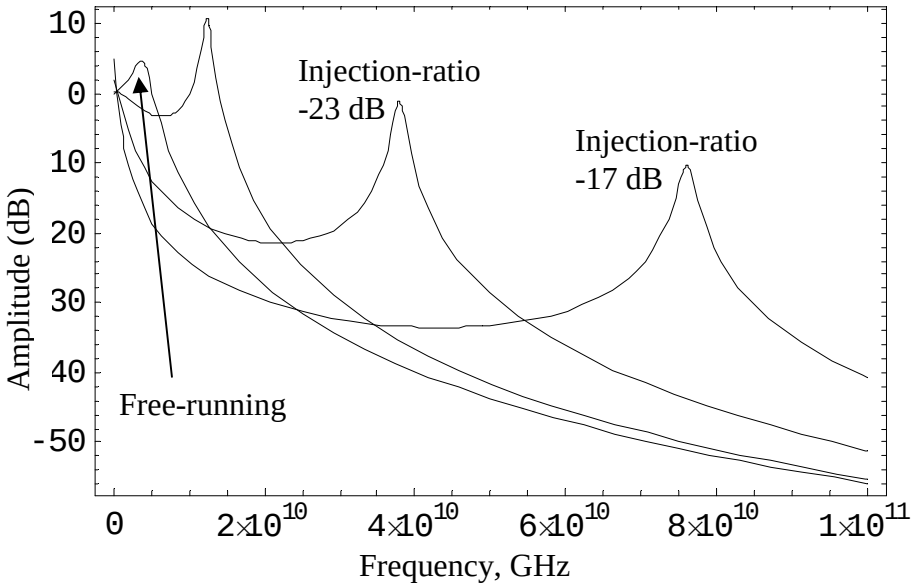

Figure 15 - Calculated frequency response for an injection-locked semiconductor laser.
The laser parameters are chosen to be that of a VCSEL with a ~4 GHz resonance frequency. 0 GHz detuning is used for all cases, and the injection ratio is -33, -23 and -17 dB

The simulation was performed up to 200 GHz frequency to verify the 40 dB/decade slope. Interestingly, for very high frequency, the small-signal response of the locked laser coincides with the free-running laser response. Thus, injection locking only affects the laser response for frequencies 0 to several times the resonance frequency.

These simulation results show that the RF phase of an injection-locked laser is well behaved, and similar to a free-running laser, but with the transition in phase occurring at the new locked resonance frequency. Thus, the RF signal will not experience a significant phase distortion in the typical transmission band (well below the resonance frequency); as expected, the injection-locking scheme increases the available RF bandwidth for analog transmission.

The parameters used for the simulations are shown in Table 3.

3.1.2. Analytic Frequency Response

Simulations of the injection-locked small signal frequency response are performed by evaluating the analytic solution presented in . The plots in Figure 15 show the effect of increasing injection power on the small signal modulation response. The injection ratio is the ratio of the external injected photon density divided by the follower laser photon density. For increasing injection power, the model predicts that the frequency response can be increased indefinitely. For a -23 dB injection ratio, the resonance frequency can be increased by a factor of ~10X, to a resonance frequency of ~40 GHz. For a higher injection ratio of -17 dB, the resonance frequency increases to ~80 GHz. A parasitic-like low frequency pole appears at ~$0.5f_r$. This is due to the fact that $H(\omega)$ is a 3-pole function, with an additional pole contributed from the injection.

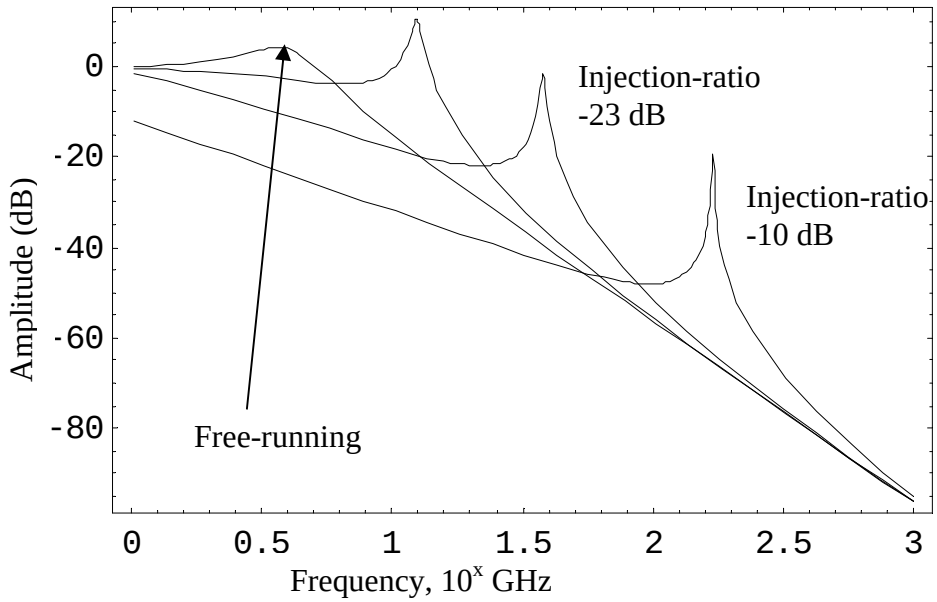

Figure 16 - Calculated frequency response for an injection-locked semiconductor laser.
The frequency response is plotted on a log-x scale, showing a 40 dB/decade decrease in the frequency response for high frequency, for both free-running and injection-locked curves. Regardless of the injection condition, the S21 for free-running and locked cases are coincident at high frequency.
The laser parameters are chosen to be that of a VCSEL with a ~4 GHz resonance frequency. 0 GHz detuning is used for all cases, and the injection ratio is -33, -23 and -10 dB

In Figure 16, the same lasers are simulated, with the frequency response plotted on a logarithmic scale (where x=1 is 10 GHz, x=2 is 100 GHz, and x=3 is 1000 GHz). As shown, for a -10 dB injection ratio, the resonance frequency increases up to ~160 GHz, a factor of 40X increase from the free-running case. For all cases, a high frequency 40 dB/decade decrease is evident in the frequency response.

Impact of Injection Conditions on Resonance Frequency

Numerical simulations of the frequency response using the small signal analytic model are also performed throughout the locking range. The results are fitted with equation (3.1) to extract the S21 parameters, and the resonance frequency is shown in Figure 17 for different detuning and injection conditions. A higher resonance frequency can be achieved with a larger injection power. The lowest detuning values will result in a higher resonance frequency, while the large positive detuning resulting in a lower resonance frequency with a higher damping.

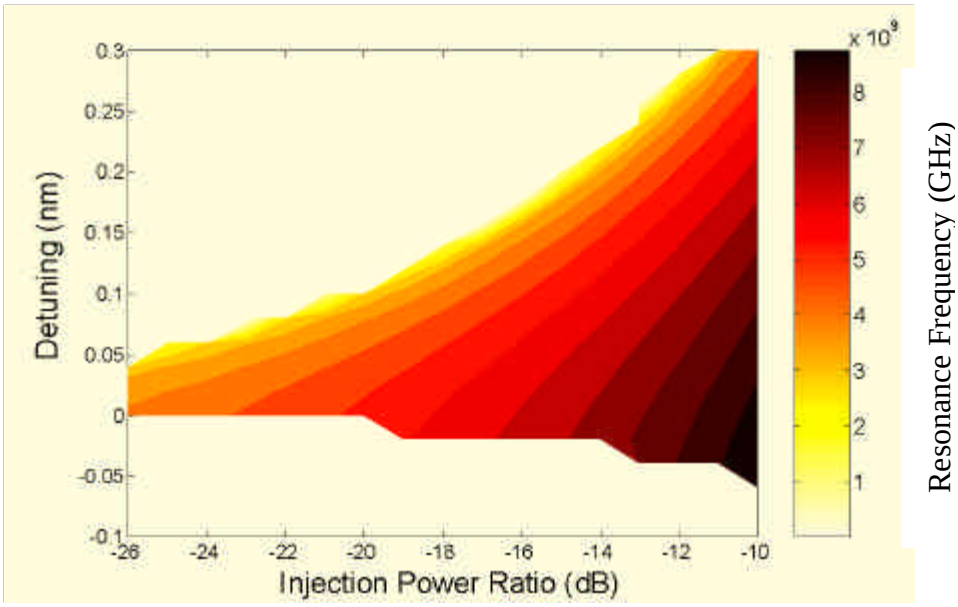

Figure 17. Simulated Arnold tongue of resonance frequency.
The theory predicts the highest resonance frequency occurs at a high injection power and small detuning condition. Taking into account of the difference in the definition of the injection power between the experiment and the simulation, the tilted stripes in the figure will become more vertical. The overall trend predicted by the theory matches well to the experimental Arnold tongue.

Figure 17 shows the simulated Arnold tongue for the resonance frequency. In the simulation, the value of the x-axis (injection power ratio) is the product of the coupling coefficient and the square root of the master and follower power ratio. The value is proportional to the power that already penetrates into the cavity and interacts with the follower laser field.

3.2. Frequency Response of Injection-Locked 1.55 ㎜ VCSELs

3.2.1. Introduction

Vertical-cavity surface-emitting lasers (VCSELs) provide a low-cost transmitter configuration for optical communication applications. The highest direct modulation bandwidth demonstrated so far is 21 GHz, realized using p-side down epi structure with strained InGaAs/GaAs QWs at 850 nm [84]. Unfortunately, lasers at this wavelength are not suitable as long-range transmitters. To fully take advantage of the fiber network, VCSEL at 1.55 μm is of great interest. However, the material difficulties at this wavelength, such as low material gain, low differential gain and the severe thermal effects in the VCSEL structure, have prevented its high-speed operation from being realized. Only recently have directly modulated VCSELs at 1.55 μm for 10 Gb/s applications (with the record 12 GHz resonance frequency) been demonstrated with InGaAlAs QWs [85].

Optical injection locking is an effective technique, other than improving the laser design, to considerably enhance the laser bandwidth. In early experiments, we have demonstrated VCSEL bandwidth enhancement using a DFB laser for injection-locking

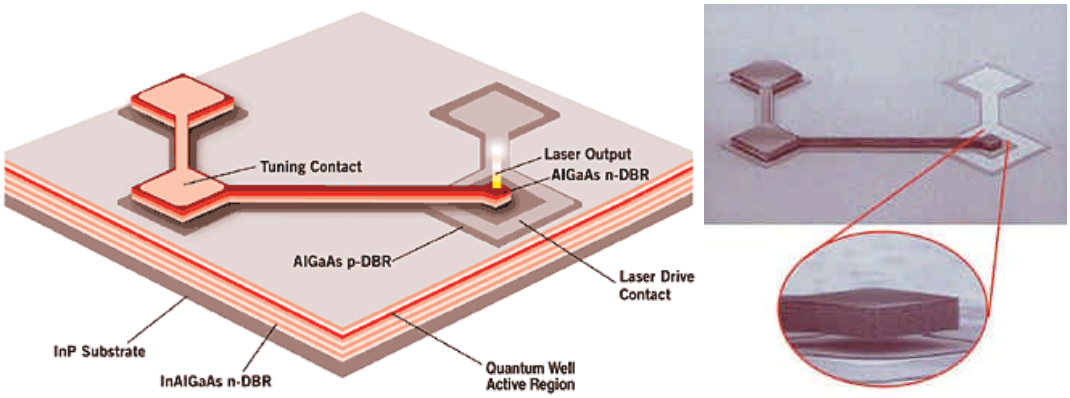

Figure 18 – BW9 VCSEL diagram and SEM.

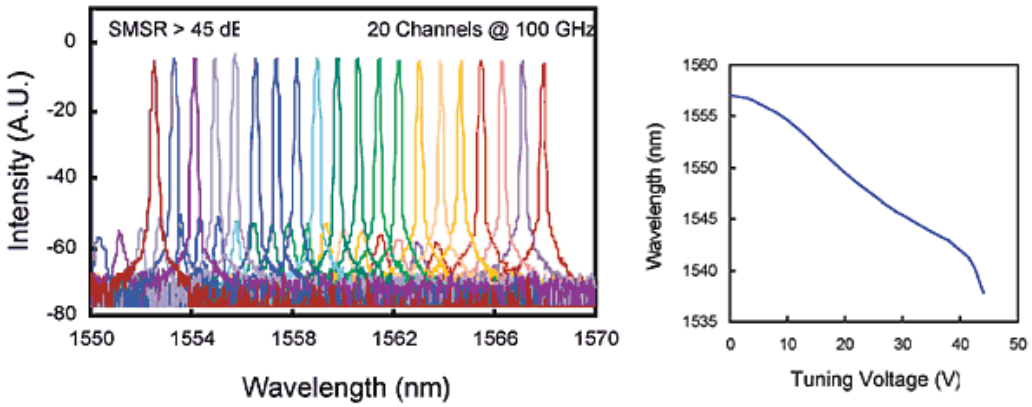

Figure 19 – BW9 wavelength tuning characteristics (typical).

[75]. The 1.55 μm VCSELs used were manufactured by Bandwidth 9 Inc., and are fully epitaxially grown with tens of pairs of mirrors and had a free-running resonance frequency of 3.5 GHz. The resonance frequency was improved to ~10 GHz by injection. This chapter focuses on whether the technique is specific for one kind of VCSEL and whether the same technique can be used to further enhance the bandwidth for higher speed applications.

3.2.2. Experiments using Bandwidth 9, Inc. VCSELs

Device Description

A top-view diagram and scanning electron microscope photograph of the Bandwidth 9 Inc VCSELs is shown in Figure 18. The device includes an electrostatically tunable top distributed Bragg reflector (DBR) mirror, which is actuated using the left contact. The right contact is used to bias the quantum well active region in the device.

Typical wavelength tuning characteristic of the devices are shown in Figure 19, with > 15 nm continuous tuning available.

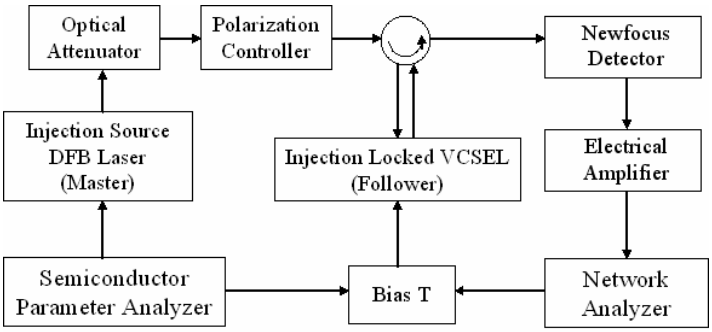

Figure 20 - The experimental setup.

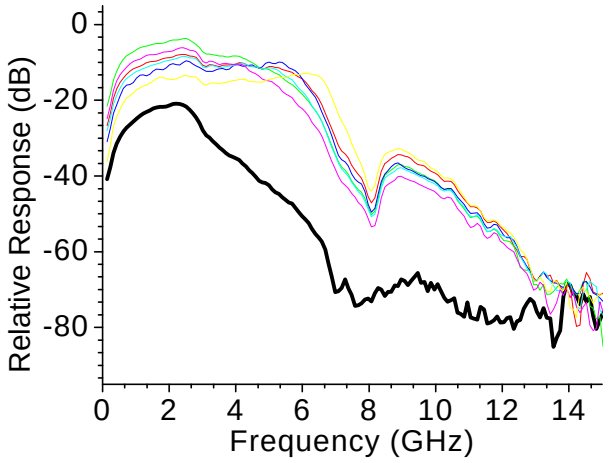

Figure 21 – Injection-locked frequency response, raw data.

Experimental Setup

The experimental setup is shown in Figure 20. The VCSEL is used as the follower laser while a DFB is used as the master laser. The wavelength detuning ($= \lambda_{DFB} - \lambda_{VCSEL}$) was adjusted by tuning the DFB temperature and the injection power was varied with an optical attenuator at the output of the DFB. The polarization of the DFB signal was adjusted using a polarization controller before injecting into the VCSEL. In the experiment, the polarization was chosen such that the VCSEL has the most significant enhancement in the frequency response.

The frequency response, or S21, of the VCSEL for different injection conditions are shown in Figure 21, as measured by the network analyzer. As seen in the data, a large modulation efficiency enhancement is observed, and a large bump appears at 9 GHz. However, from this data, it is unclear at what frequency the resonance is. The data is significantly impaired by the parasitics present in the device and packaging.

To understand the injection-locking phenomena and impact on the small-signal frequency response, it is crucial to determine and remove the parasitics. This can be done either by physical design, or by data analysis. The following section describes the

method developed to analyze the intrinsic laser frequency response.

Parasitic Extraction

Measuring a laser frequency response involves understanding the frequency response of the cables, amplifiers, detector, device packaging, as well as the device parasitics. Calibration of cables, amplifiers and the detector can be accomplished using the network analyzer "thru" calibration. However, measuring the device parasitics can be difficult. Measuring the reflection can give insight into the device transfer function, but does not provide method of calibrating for device parasitics.

One method of determining the laser device parasitics is by measuring the system frequency response for two bias conditions, and fitting the difference of the measurement to two theoretical small-signal modulation frequency responses [86]:

$$H_1(f) - H_2(f) = \frac{1}{\left(1-\left(\frac{f}{f_{1r}}\right)^2\right)^2 + \left(\frac{g1}{2p\, f_{1r}}\right)^2 \left(\frac{f}{f_{r1}}\right)^2} - \frac{1}{\left(1-\left(\frac{f}{f_{r2}}\right)^2\right)^2 + \left(\frac{g2}{2p\, f_{r2}}\right)^2 \left(\frac{f}{f_{r2}}\right)^2} \quad (3.4)$$

The ideal response is then compared to the measured response, and the difference is the parasitic term. This procedure can be performed several times for different biasing conditions to find the average parasitic response. This technique however only yields useful calibration up to frequencies for which the signal is significantly above the noise floor of the detection system.

In cases where injection-locking increases the resonance frequency to a relatively high frequency, especially for frequencies higher than the device parasitics, the technique described does not provide accurate calibration. For cases where the injection-locked peak is measurable, this technique has been extended to use the injection-locked small-signal frequency response, rather than the free-running small-signal response. The injection-locked frequency response has been shown to be the same as a free-running laser, but with an additional effective 1st order pole. The difference of two responses is thus:

$$H_1(f) - H_2(f) = \frac{1}{1-\left(\frac{f}{f_{O1}}\right)^2} \frac{1}{\left(1-\left(\frac{f}{f_{1r}}\right)^2\right)^2 + \left(\frac{g1}{2p\, f_{1r}}\right)^2 \left(\frac{f}{f_{r1}}\right)^2} - \frac{1}{1-\left(\frac{f}{f_{O2}}\right)^2} \frac{1}{\left(1-\left(\frac{f}{f_{r2}}\right)^2\right)^2 + \left(\frac{g2}{2p\, f_{r2}}\right)^2 \left(\frac{f}{f_{r2}}\right)^2} \quad (3.5)$$

Figure 22a shows the frequency response of two injection-locked conditions. Figure 22b shows the difference of the two responses, as well as a fit using the above equation.

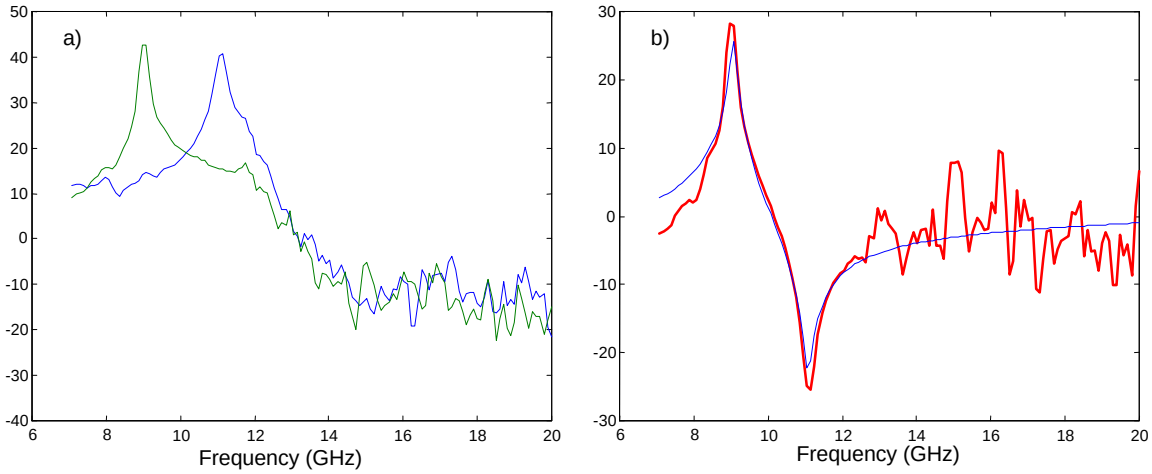

Figure 22 – Parasitic estimation method
(a) Two sample measured injection-locked frequency response curves
(b) difference of the measured response, with a curvefitted result

Comparing the curves in Figure 22a with the fitted modulation response using the parameters found in Figure 22b, one finds the parasitic response of the system, showing in Figure 23a. As can been seen from this figure, the parasitic has a frequency response with a -3dB bandwidth of approximately 12 GHz. Finally, subtracting the parasitic response from the measured data, one obtains the parasitic-free modulation response, in Figure 23b, which is much easier to interpret the raw data shown in Figure 21.

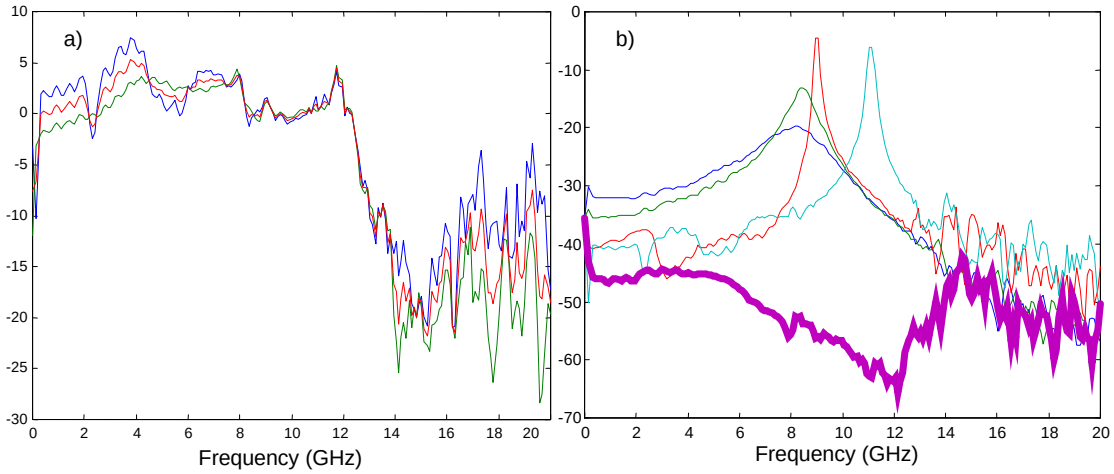

Figure 23 – Parasitic estimation method
(a) Parasitic frequency response, (b) Parasitic-free injection-locked frequency response.

For S21 measurements of lasers that have extremely severe device parasitics, other techniques can be used. First, an optical amplifier can be used as a pre-amplifier before the detector, which lowers the noise floor and extends the frequency range which is measurable. Second, the RF electrical input amplitude into the device can be varied. For the high frequency portion, an electrical amplifier can be used to boost the signal going into the device. Care must be exercised not to input too high a modulation current at low frequencies, where the parasitics are not limiting the transmission of power into the laser. Alternatively, a network analyzer can be made to have variable output power during the

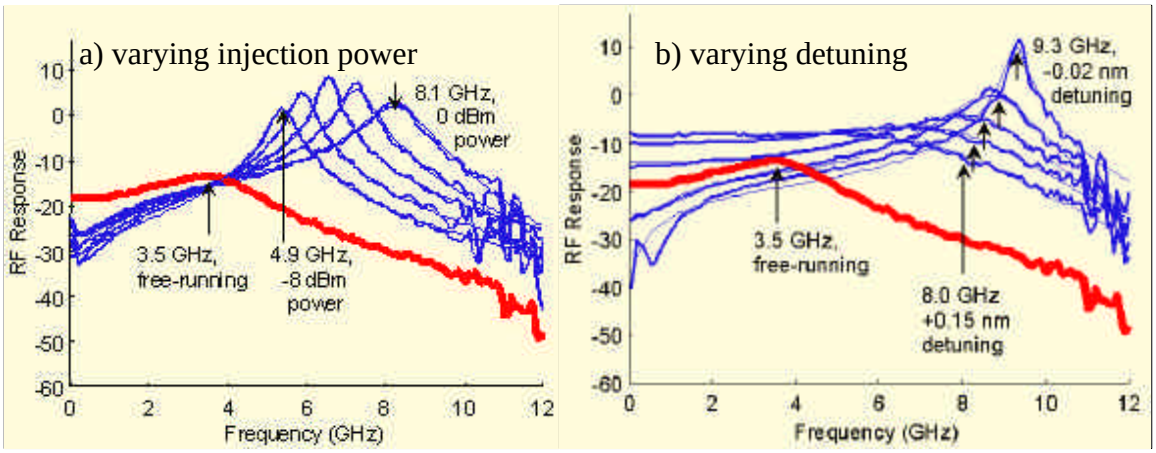

Figure 24 - Effect of injection power and detuning on frequency response.
The free running S21 curve is also shown as the reference. The arrows indicate the position of the resonance peak from curve fitting. For the fixed detuning case (a), the injection power is ~0 dBm. The resonance frequency increases with injection power. For the fixed injection power case (b), fr increases from 8 GHz to 9.3 GHz when detuning changes from +0.15 nm to -0.02 nm. The large detuning cases exhibit relatively flat S21 up to 7 GHz.

frequency sweep. A linear increase in the output power can be used to increase the signal-to-noise ratio for the high frequency region. Finally, the easiest is to configure the network analyzer to measure in two frequency bands. The first is for low frequency (< 10 GHz) with a low power, ex. -30 dBm, and the second is for higher frequency (> 10 GHz), with a higher input power, ex. -10 dBm. This higher power compensates for the loss due to the device parasitic and allows measurements to higher frequencies.

Experimental Results with Bandwidth 9, Inc VCSELs

Each experimental S21 is fitted to the theoretical frequency response of an injection-locked laser, which is found to be the same form as that of a free-running laser with an additional 1st order pole [75]:

$$H(s) \propto \frac{s + a_0}{s^3 + b_2 s^2 + b_1 s + b_0} \propto \frac{1}{1 + jw\mathrm{K}} \cdot \frac{1}{w_R{}^2 - w^2 + jwg} \tag{3.6}$$

In this equation, s = jω and K represents the 1st order pole introduced by the injection, ω_R the resonance and γ the damping term. The injection conditions together with the laser parameters determine these coefficients and, therefore, the small signal performance of the injection-locked laser.

To calibrate the device and packaging parasitic, the subtraction result of two S21 curves at different conditions is fitted to an equation, which is the subtraction of two ideal injection-locked responses, equation (3.6), with different parameters, as described in the previous section.

Once the modulated follower VCSEL is stably locked, its frequency response is measured with a network analyzer at -10 dBm modulation power level. Figure 24a shows family curves for various injection conditions. All the S21 curves are fitted with equation (3.6) to obtain the resonance frequency and the damping values. In the case of a fixed detuning around 0 nm, the resonance frequency is enhanced more than 2x for the strongest injection power. For a fixed injection power around 0 dBm, the resonance frequency enhancement in Figure 24b is more than 2x, but the damping clearly increases

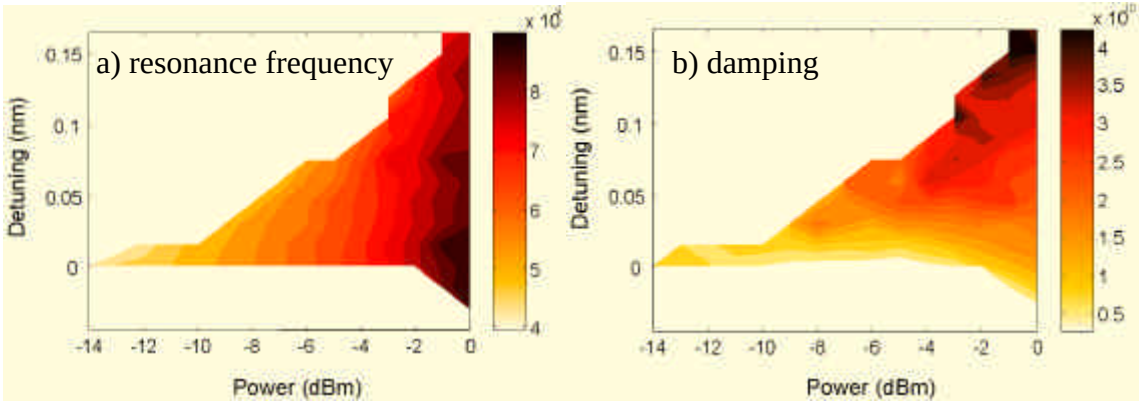

Figure 25 - Experimental Arnold tongues of resonance frequency and damping.
a) A higher injection power is desirable to improve the resonance frequency. b) A larger detuning yields a higher damping, thus flatter small-signal frequency response curves.

with the amount of detuning, resulting in both peaky and flat S21. A flat S21 is especially suitable for wide-band modulation applications. In some cases, the S21 are relatively flat from DC to ~7 GHz with resonance frequencies of more than 8 GHz. Compared to its free running value at 3.5 GHz, this is a highly desirable improvement by injection locking.

Another interesting observation is that the amplitude of the S21 varies with different detuning values. This is clearly seen in the low frequency regime, where the amplitude enhancement in Figure 24b can be more than 10 dB in some cases for high detuning values. This improvement of the modulation efficiency directly translates into the RF gain in an analog link. The increase of the fundamental tone power also results in a larger spur-free dynamic range. This is another advantage of injection locking technique in the analog applications. The physical origin of this modulation efficiency has never been predicted before, and has not been observed by other research groups. The origin of this improvement has not yet been understood.

The rich characteristics of the S21 curves warrant a thorough study for different injection conditions. S21 measurements throughout the entire Arnold tongue were performed and the results were again curve-fitted to equation (3.6) to extract the resonance frequency and the damping value. The obtained f_r and damping values are plotted as a function of the injection power and detuning in Figure 25.

Figure 25a indicates that a higher resonance frequency can be achieved with a larger injection power. The injection power is defined as the absolute amount of power incident on the follower VCSEL without taking into account the coupling loss. The small detuning values will result in a higher resonance frequency, but the effect is relatively small (note the almost vertical stripes in the figure). From the damping Arnold tongue in Figure 25b, it is obvious that both injection power and detuning play important roles in determining the damping value. The largest damping happens when both the injection power and detuning are large. Flat modulation response curves are observed for cases where the damping is larger than the resonance frequency, and occur for large detuning. The flattest S21 curve in Figure 24b corresponds to the upper-right corner in the damping Arnold tongue. These two Arnold tongues suggest that a large positive detuning with a high injection power is the best for frequency response improvement with a flat S21 featuring a high modulation bandwidth.

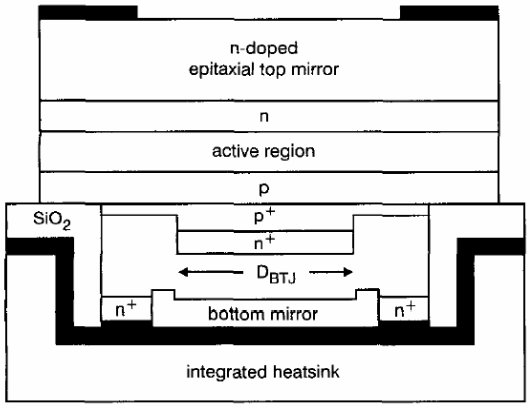

Figure 26 - Schematic diagram of the BTJ-VCSEL [87]

Experimentally, we have observed that reflection coefficient varies with detuning relative to the cold cavity resonance peak. In particular, the reflection coefficient is lowest at the cavity wavelength and increases as detuning increases; this results in a higher power coupling for 0 nm detuning. Note the similarity between Figure 25a and Figure 17. The figures would be even more similar if the theoretical power was calibrated to the actual power getting into the follower cavity (tilt the vertical stripes in Figure 17 to the left). Alternatively, we note that the photon lifetime should be reduced for lasing at an off Fabry-Perot condition. The reduced photon lifetime would lead to an increased resonance frequency. The experimental results agree in trend with the theoretical predictions.

3.2.3. Experiments using Walter Shotky Institut, M. C. Amann VCSELs

In this section, we investigate the injection-locked performance of a 1.55 μm VCSEL with a different mirror and active region design concept than the Bandwidth 9 VCSELs. Its resonance frequency is enhanced from 7 GHz to 28 GHz, the highest reported VCSEL resonance frequency. The improvement by injection locking is thus universal for different kinds of lasers and can be routinely achieved. The experiments also demonstrate the scalability of the resonance frequency enhancement for higher speed devices.

Device description

A 5-QW InGaAlAs/InP VCSEL at 1.55 μm with sub-mA threshold current is used in this experiment [87]. A buried tunnel junction (BTJ), a short period dielectric back-side mirror and an electroplated heatsink are incorporated in the structure to realize a low resistance, high efficiency and output power device, shown in Figure 26.

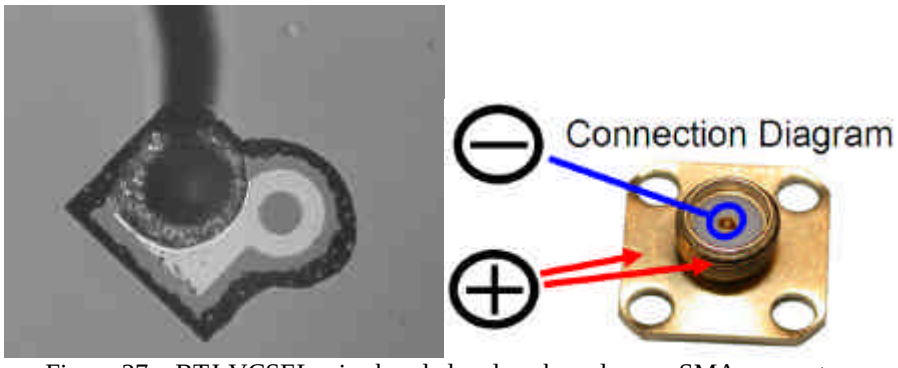

Figure 27 – BTJ-VCSEL wire-bonded and packaged on an SMA connector.

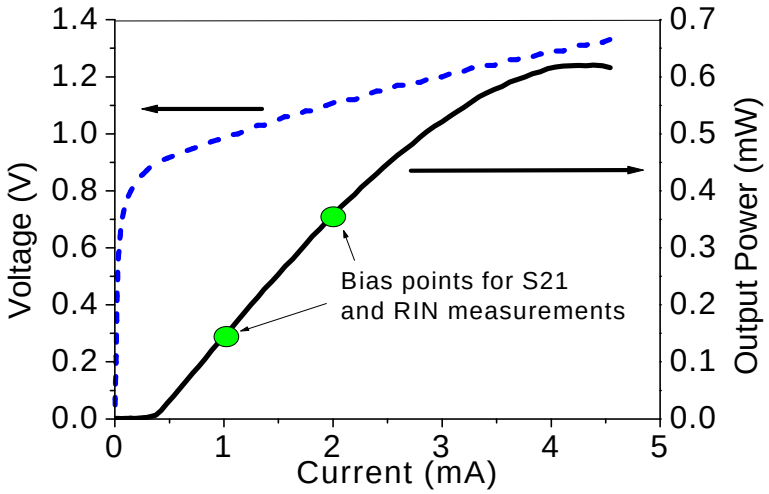

Figure 28 - LIV curve of the M.C. Amann 1.55 um VCSEL.
The two dots indicate the bias points chosen for the frequency response and RIN characterization.

The device was packaged for high speed operation, by wire-bonding the device to an SMA connector, shown in Figure 27.

The light output and voltage versus drive current curve of this device is shown in Figure 28. The laser threshold current is 0.4 mA. In the figure, the two biasing conditions chosen for the experiment are shown: at a 1.0 mA biasing current, the free-space output power is 0.147 mW (fiber circulator coupled -15 dBm) and the resonance frequency is 7 GHz; at 2.0 mA the output power is 0.36 mW (fiber circulator coupled -11 dBm), and the resonance frequency is 10 GHz.

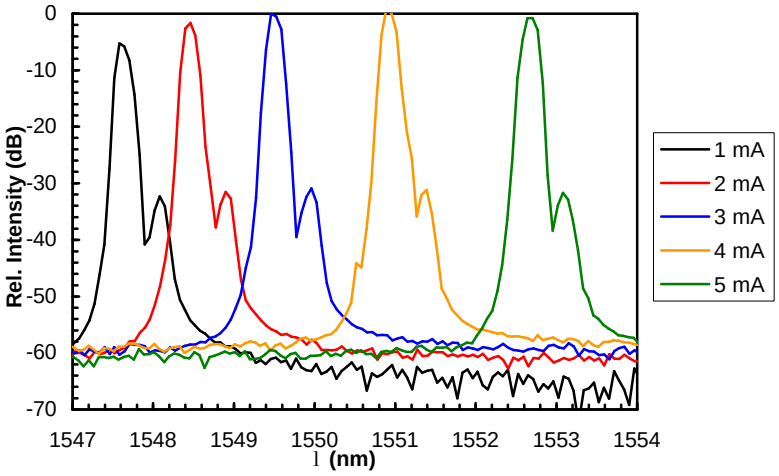

Figure 29 – Optical spectra of the free-running M.C. Amann 1.55 um VCSEL.

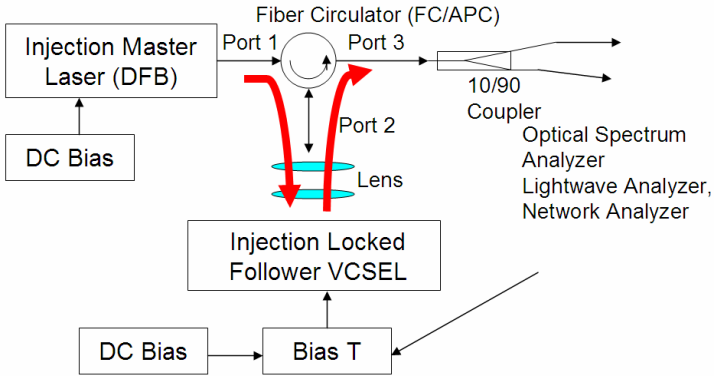

Figure 30 – Experimental setup.

The optical spectra for the device for various bias conditions are shown in Figure 29. The side-mode suppression ratio (SMSR) is ~30 dB. The optical output of the VCSEL was filtered using a Glan-Thompson polarizing beam-splitter cube, to determine the polarization of the light. By rotating the polarizer, it was found that the two modes were linearly polarized with the two modes nearly perpendicular to one-another (80 degree polarization).

Experimental Setup

The experimental setup is similar to that used in the previous BW9 VCSEL experiments [75]; however, the VCSEL is injection-locked using a polarization maintaining circulator, as shown in Figure 30. A polarization maintaining fiber coupled Ortel/Emcore DFB laser (RIN < -165dB/Hz, P_{max}=38 mW) is used as the master laser. As such a high power was unnecessary for the experiment, the master laser was significantly attenuated. The VCSEL light is coupled into the polarization maintaining fiber circulator (port 2) using two lenses with a 4.5 mm focal length. The VCSEL was directly modulated a characterized using a 40 GHz network analyzer, and noise was characterized using an EDFA, optical filter and lightwave analyzer. The wavelength

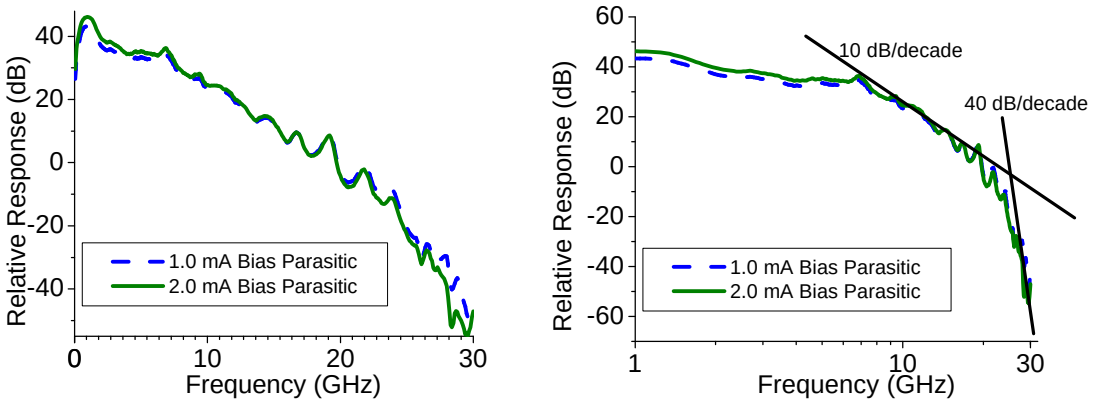

Figure 31 - Parasitic frequency response of the measurement system and Amann VCSEL
Data is plotted in linear frequency (left), and on a logarithmic frequency scale (right).

detuning (= λ_{DFB} - λ_{VCSEL}) was adjusted by tuning the DFB temperature and current. The injection power is varied by adjusting the DFB bias and by adjusting the FC/APC connectorization loss. The polarization of the DFB signal is adjusted to match the polarization of the VCSEL by rotating the circulator fiber (port 2) relative to the VCSEL. For master light perpendicularly polarized to the free-running VCSEL polarization (non-matching polarization), no locking was possible even for the highest injection powers.

The experimental small-signal frequency response (S21) data is fitted to the theoretical injection-locked laser frequency response [75]. The system and device parasitics, which are assumed constant for a given bias, are found by curve-fitting the difference of two S21 curves. Using this technique, we can study the intrinsic laser modulation response, free from all parasitics.

Results

The small signal frequency responses for the injection-locked curves are downloaded and used to calculate the parasitic response of the system, packaging, and laser.

The parasitic frequency response is shown in Figure 31. The low-frequency bump and drop at 0 GHz are due to the network analyzer. The frequency response is relatively flat up to about 7 GHz, after which the response is dominated by the parasitics and the response is significantly attenuated. At 30 GHz, the loss is 90 dB higher than for low frequencies. For the frequency range of 12 to 24 GHz, the response decreases at ~10 dB/decade, shown in Figure 31b.

This parasitic is attributed to the device or device packaging. For frequencies between 25 and 30 GHz, the response decreases much faster, at approximately 40 dB/decade. The detector and amplifiers used for the measurement are limited to 22 GHz, thus the measurement system is attributed to be the main contributor to the frequency response decrease.

Given that the parasitic response for this laser is so severe, it is essential to subtract the parasitic response from the measured data, in order to analyze the intrinsic laser response. The consequence of the large parasitic is that for high frequency operation,

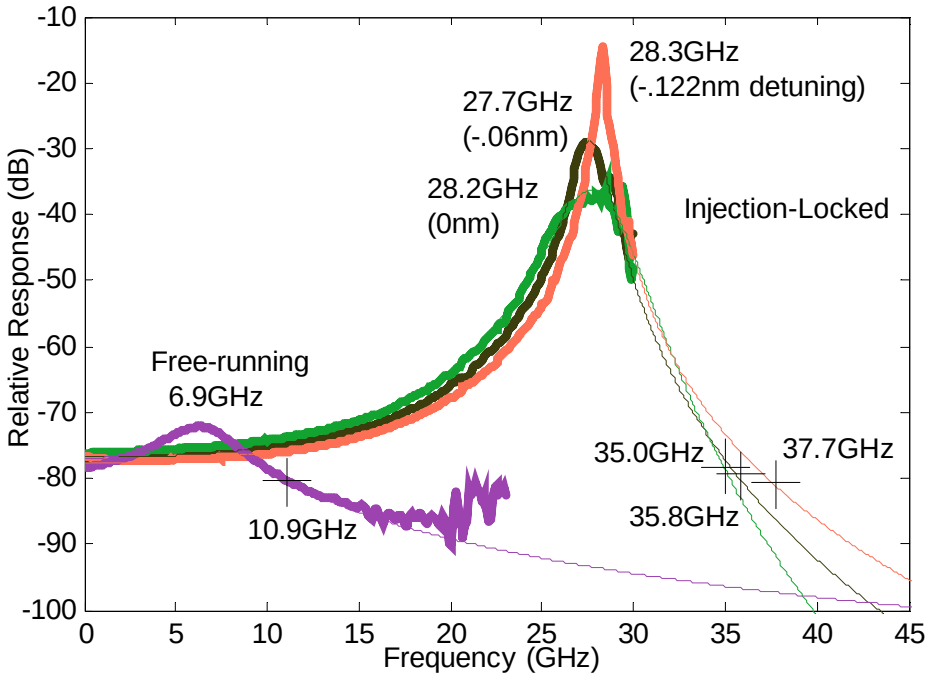

Figure 32 – Injection-locked frequency response of Amann VCSEL biased at 1.0 mA
The estimated injection power is -1 dBm, with wavelength detunings of 0, -0.06 and -0.122 nm. The free-running resonance frequency is enhanced from 7 GHz to 28 GHz for a -0.122 nm detuning. The estimated 3 dB bandwidth is 38 GHz. The small-signal responses are calibrated.

device engineering is required to reduce the device parasitics. For large signal digital modulation for example, a flat frequency response is desired up to approximately the bit rate of the signal, depending on the modulation scheme.

Measurements were performed for varying injection power and detuning, and the measured small-signal frequency response data was calibrated using the parasitic response.

Figure 32 shows the calibrated small-signal frequency response of the VCSEL biased at 1.0mA for an approximate injection power of -1 dBm, for various wavelength detunings. All parasitics have been removed from the data. The highest injection-locked relaxation oscillation frequency (f_r) obtained is 28 GHz (4.3X improvement from 6.5 GHz free-running). The lowest damping (sharpest resonance peaks) occur for the lowest detuning values (-0.122 nm detuning in this case). The S21 measurements were instrumentation limited, and the 3 dB bandwidth of the locked laser can be estimated using the curve-fit frequency response, and is found to be as high as 37.7 GHz.

In Figure 33, the VCSEL is now biased at 2.0mA with an estimated injection power of 2.5 dBm, and the resonance frequency is enhanced from 10 GHz to 28 GHz (~3X). A flat response with a high f_r of 26.7 GHz with an estimated 39 GHz bandwidth is obtained for large detuning. A lower detuning usually yields a smaller damping, resulting in an S21 with sharp resonance peak. On the other hand, if a flat S21 is desirable, a large detuning should be used. Additionally, at 0.5mA biasing, a 7X enhancement from 3.5

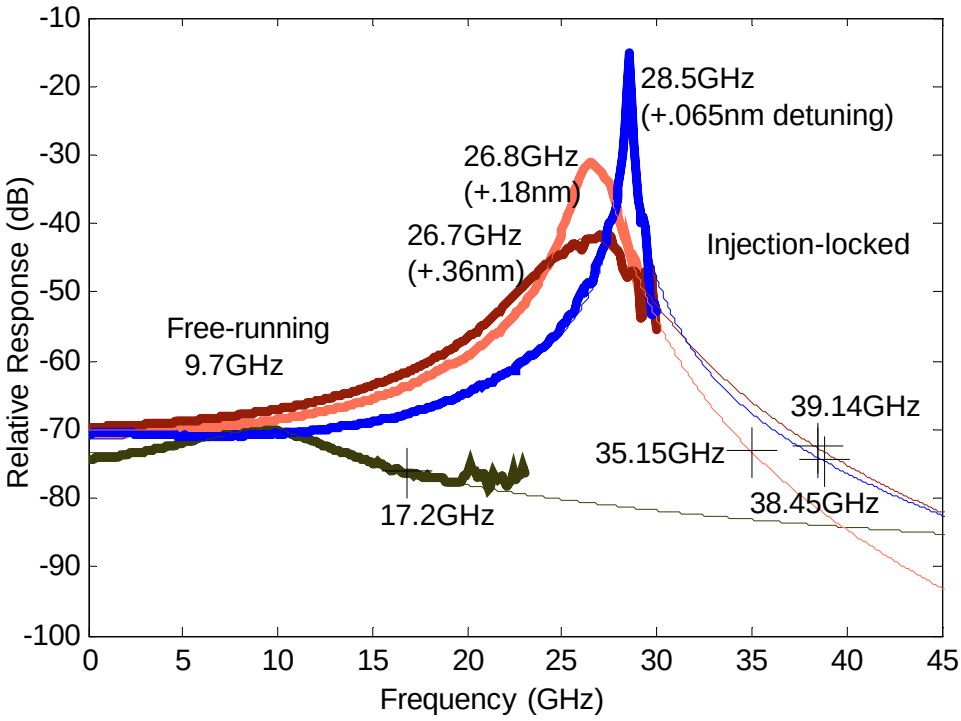

Figure 33 – Injection-locked frequency response of Amann VCSEL biased at 2.0 mA
The estimated injection power is +2.5 dBm, with wavelength detunings of 0.065, 0.18 and 0.36 nm. The free-running resonance frequency is enhanced from 10 GHz to 28 GHz for a 0.065 nm detuning. The estimated 3 dB bandwidth is 39 GHz. The small-signal responses are calibrated.

GHz to 24 GHz was observed.

The approximate injection power was determined by observed the reflected master light power when the VCSEL is turned off, assuming that the reflected light is coupled with the same coupling coefficient as the VCSEL light (-6.5 dB loss), and that all the light collected actually interacts with the VCSEL. For the highest injection condition, estimated to be -1 dBm, the master DFB light at the output of the circulator port 2 is 10.5 dBm, while power coupled into the circulator is -7.5 dBm. Assuming the same coupling loss, -6.5 dB, suggests that the incident power on the VCSEL could be as high as 4 dBm. However, there is a mismatch between the size of the fiber core and the VCSEL aperture, and the reflected power could be reflecting from an area on the VCSEL outside the aperture; thus, the optical power that actually is present in the locking could be far lower. Indeed, determining the actual power that is incident on the aperture of the VCSEL is difficult.

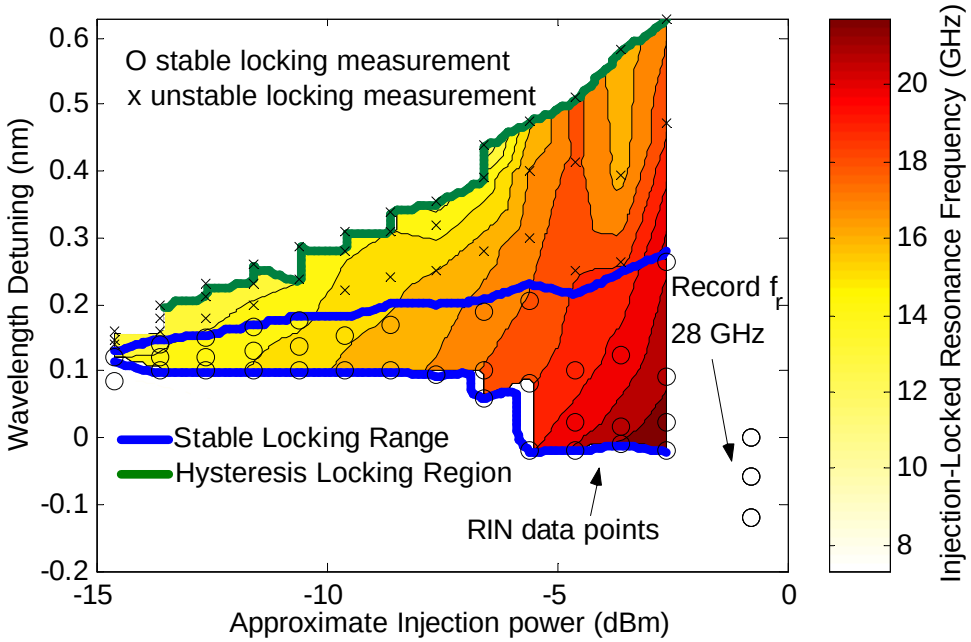

Figure 34 – Locking plot (VCSEL at 1 mA)

For a fixed VCSEL bias at 1mA, the resonance frequency is plotted in Figure 34 over the locking range, for varied detuning and injected power. The highest resonance frequency is seen for the highest injection power and lowest detuning. In the stability plot, the stable locking range (data points marked with an O) is between 0 nm and 0.25 nm for -2.5 dBm injection power; for larger detuning, the VCSEL is unstably locked (data points marked with an X). In this region, the VCSEL can be locked only if the master wavelength swept from the stable region into the unstable. If the coupling between the lasers is simply turned on for such a condition (ex. 0.5 nm detuning), the VCSEL will not lock to the main mode. Instead, it may be possible to lock to a longer-wavelength 2nd polarization mode of the VCSEL.

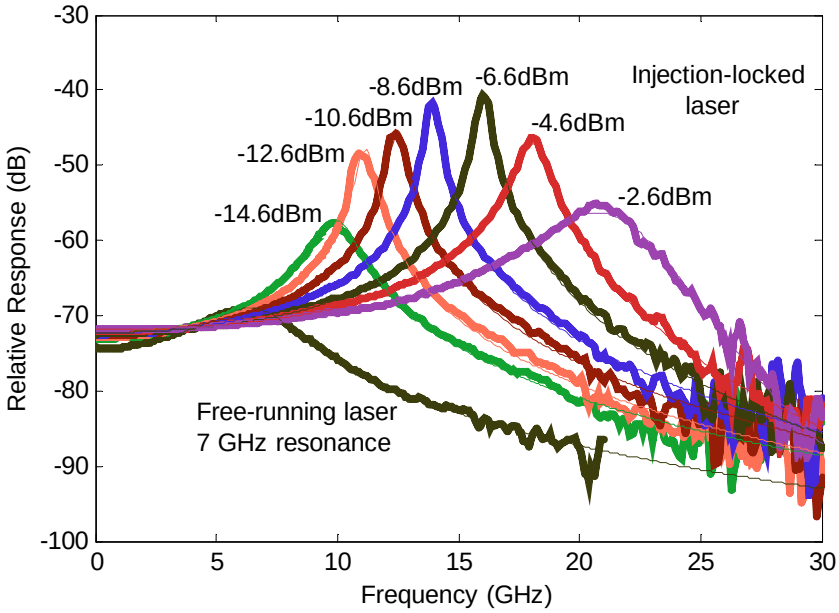

Figure 35 – Injection-locked frequency response of Amann VCSEL biased at 1.0 mA
The injection power is varied from -14.6 dBm to -2.6 dBm, for a fixed wavelength detuning of 0.10 nm. The free-running resonance frequency is enhanced from 7 GHz to between 10 and 22 GHz, depending on injection power. The small-signal responses are calibrated.

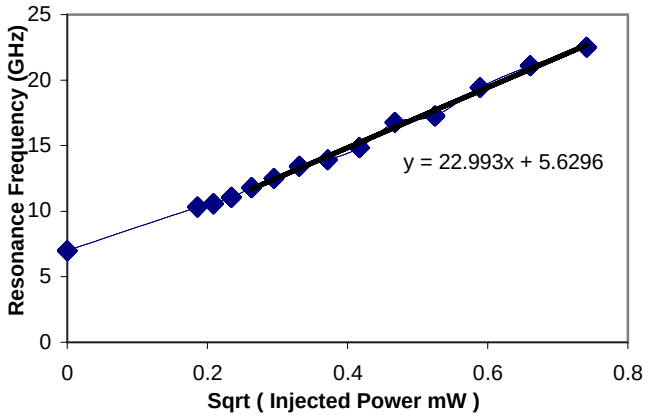

Figure 36 – Experimental resonance frequency vs. square root of the injection power.
Amann VCSEL is biased at 1.0 mA. The resonance frequency is the highest observed (i.e. at lowest locked detuning) for the given injection power.

The small-signal frequency response is plotted for varying injection power for a 0.10 nm detuning, in Figure 35. As seen, the resonance frequency is increased for increasing optical injection power.

It has been analytically predicted that the resonance frequency is expected to vary as the square root of injection power [81]:

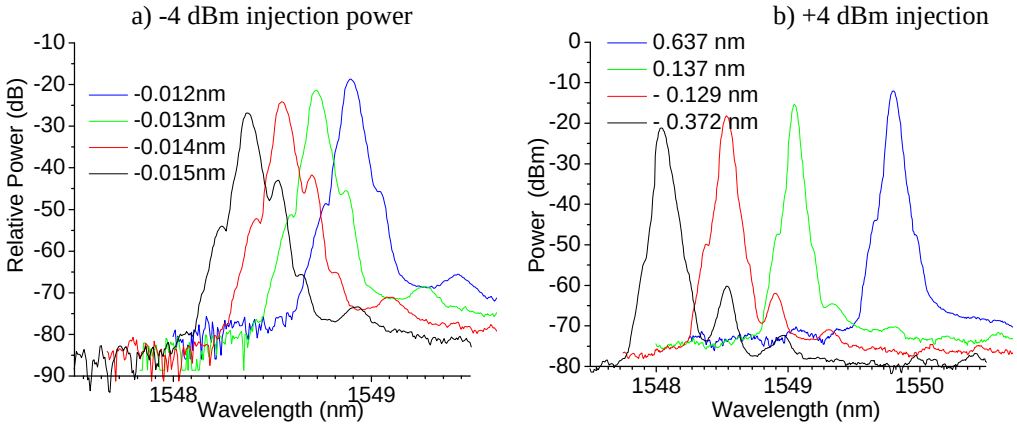

Figure 37 – Injection-locked optical spectra of Amann VCSEL biased at 1.0 mA
The spectra shown are near the unlocking edge for the lowest locked detuning. The injection power is a) -4 dBm, b) +4 dBm. The optical side-mode present in (a) correspond to the resonance frequency. Based on the spectra (b) for higher injection power, it is speculated that much higher resonance frequencies are present in the locked VCSEL.

$$w_r^{\,2} = \frac{v_g \frac{dg}{dn} S}{t_p} + k_c^{\,2} \frac{S_{inj}}{S} + \ldots \qquad (3.7)$$

This relationship is confirmed by these experiments, by plotting the resonance frequency versus the square root of the injection power. As seen in Figure 36, the resonance frequency increases with increasing power, and follows a square-root dependence, as predicted by equation (3.7). The line of best fit is also shown for reference. The slope of the line is related to the injection coupling parameter k_c and the magnitudes of the photon densities.

The S21 measurements were limited to < 30 GHz by the test equipment; however, locking at much higher powers was possible. A natural question to ask is if there is a limit to the resonance frequency enhancement for higher injection power, and if so, to what frequency.

The injection-locked optical spectra, measured near the low detuning locking edge, for an injected power of -4 dBm, are shown in Figure 37a. It was observed that the optical spectra for exhibited optical side-modes at a 0.15 nm spacing from the fundamental mode (or 19 GHz). This mode spacing corresponds exactly with the resonance frequencies observed in the RIN spectrum and S21 (~19 GHz). For a high injection power (8 dB more, or +4 dBm injected power), we find that the optical spectra have similar features, shown in Figure 37b. For a detuning of -0.372 nm, a side-mode appears at a difference of 0.50 nm (62.5 GHz). For -0.129 nm, it is at 0.37 nm (46.5 GHz), and for a detuning of 0.137 nm it is at 0.29 nm (36.5 GHz). For other conditions, a mode-spacing of 0.6 nm (75 GHz) was observed. At high injection power, a locking range as large as 1.9 nm was observed. Based on the observation of the optical spectra, it is predicted that much higher resonance frequencies, > 40 GHz, are possible.

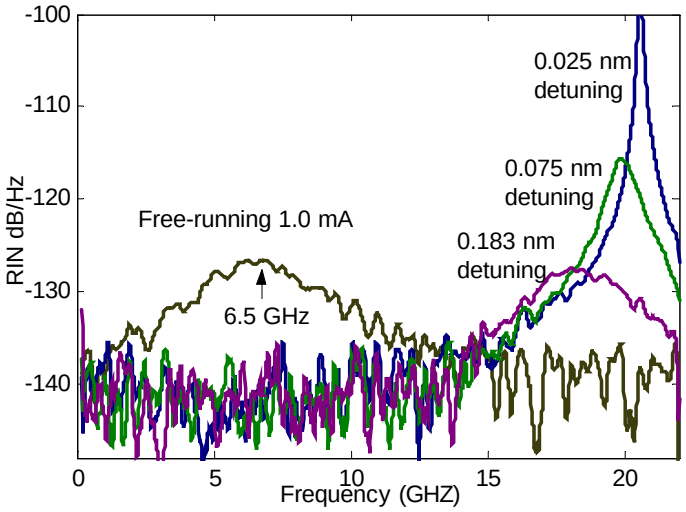

Figure 38 - Experimental relative intensity noise of Amann VCSEL
The VCSEL is biased at 1.0 mA, and the free-running response shows a resonance peak of approximately 6.5 GHz. The injection-locked resonance peaks are at approximately 20 GHz, depending on the detuning. A broadband reduction in noise is observed from 0 to 13 GHz.

The RIN of the injection-locked laser was characterized and compared to the free-running laser noise. It was verified that the RIN peak frequencies matched that of the S21 data. The locked RIN spectra at a 1.0mA bias for different detuning are shown in Figure 38, showing a broad-band noise reduction. Due to coupling loss, the RIN measurement was limited by the EDFA noise to a floor of ~ -142 dB/Hz.

3.2.4. Experiments using Infineon DFB lasers

Injection-locking using DFB lasers was also performed. The lasers used were from Infineon Technologies, and are similar to the lasers described in [88], except that the ones used did not have an electro-absorption laser and were not optimized for high-speed operation. In these experiments, the light injection was incident on one facet, while the output light was collected on the other. Thus, no circulator was necessary.

The small signal modulation response was measured, shown in Figure 39. The data was calibrated using the parastic extraction technique. Several free-running curves at various biasing conditions were used to calculate the device parasitic response. The injection-locked data was calibrated with this calibration.

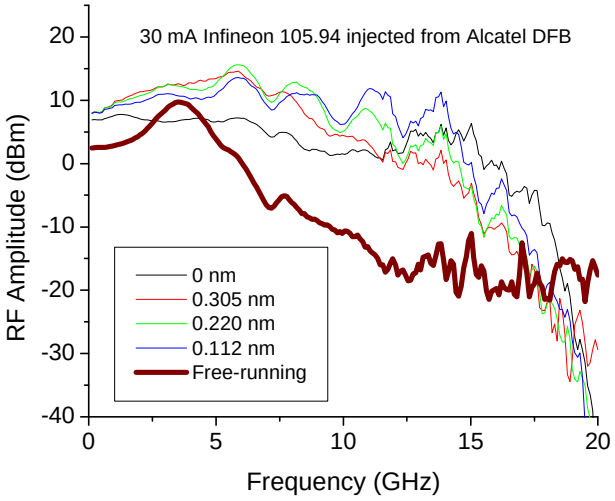

Figure 39 - Frequency response of injection-locked DFB

The data clearly shows a modulation current efficiency enhancement for the low frequency region (0-2 GHz), with an increase of ~5 dB. The resonance frequency is increased, though it is not clear from the data to what frequency.

3.2.5. Summary

Theoretical studies presented in this chapter have shown that an enhanced small-signal response is expected from injection-locking. Both analytic and numerical simulations have shown that the resonance frequency is increased for locked conditions, with higher power leading to higher resonance frequencies.

Experimentally, we have demonstrated a record high-speed VCSEL with 28 GHz resonance frequency using the injection locking technique. This resonance frequency is more than 3x higher than its free-running value. This is achieved with -1 dBm injection power using a polarization maintaining DFB. A small detuning and a higher injection power are desirable to maximize the resonance frequency improvement.

The injection locking technique has been shown to be yield small-signal frequency improvements in three different laser structures – two VCSELs and one DFB. The data demonstrates that the injection technique is not limited to a particular class of lasers, and can be considered universal.

The Arnold tongue resonance frequency data for the Amann VCSEL (Figure 34) and for the BW9 VCSEL (Figure 25) experiments agree in trend with the theoretical predictions (Figure 17). It is found that the highest resonance frequency is observed for the highest injection power, with highly damped frequency responses for large detuning values. Additionally, the resonance frequency enhancement is believed to not be limited, and will continue increasing with even higher injection powers. These observations suggest that even higher resonance frequencies will be possible in injection-locked lasers.

Chapter 4 Relative Intensity Noise

This chapter is concerned with the intensity noise in semiconductor lasers with the presence of injection-locking.

For analog fiber communication applications, where a large dynamic range is desirable, a low system noise is necessary. One of the sources of noise in a link is the laser noise, and is dominant in typical analog links. Considerable effort has been directed to reducing laser noise, with analog laser designs incorporating techniques to reduce the coupling and rate of spontaneous emission. Alternatively, it has been predicted that injection-locking may reduce relative intensity noise. This chapter presents the theoretical and experimental work to demonstrate that large reductions are indeed possible.

First, theoretical models for free-running laser noise are presented and extended to injection-locked lasers. Simulations are performed to predict the noise characteristics of locked lasers. Both the analytic model from Chapter 2, and numerical simulations to the rate equations are used. Finally, experimental characterization of laser noise demonstrates that the laser noise can be reduced significantly.

4.1. Noise in Semiconductor Lasers

The study of noise in lasers began as early as 1966 with work by McCumber [89], where the rate equations are modeled with the inclusion of Langevin noise terms. A study of noise begins with a clear understand of the Langevin noise terms introduced in the rate equations.

Noise in lasers is due to the discrete nature of the electrons and photons inside the cavity. Each change in the photon or electron number is a random event with a probability of the event occurring. Thus, all rates in the rate equation (ex. conversion of electrons to photons) are a random variable with a Poisson distribution. The noise spectral densities and cross-spectral densities are given by the shot-noise expression (variance of noise is equal to the signal). As shown by C. Harder [90], the noise terms can be written down from the rate-equations, by accounting for the rates entering and leaving the photon and electron reservoirs.

This is shown in Figure 40, where the changes in the electron (n_0) and photon (p_0) populations are associated with a shot noise term. This noise is termed Langevin noise.

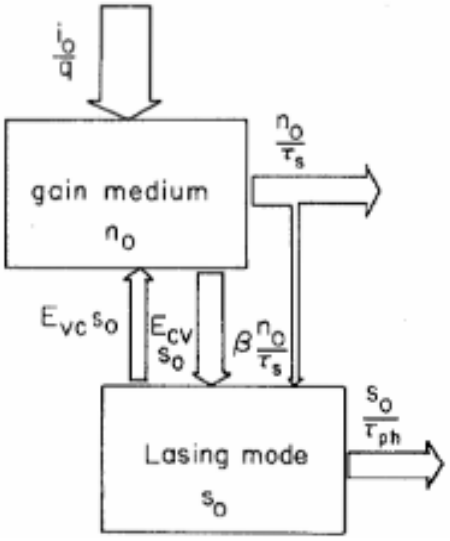

Figure 40 – Model for the shot noise in a semiconductor laser [90].

Using this model, one can model the rate equations using either analytic or numerical approaches. Numerical simulations of the noise driven rate equations have been presented leading to a circuit equivalent model [90]. As well, multi-mode laser noise has been studied [91].

Analytic solutions to the noise driven rate equations result in the following approximate result [92]:

$$RIN(w) \approx \frac{2R_{sp}\left\{\left(\Gamma_N^2 + w^2\right) + G_N P\left(G_N P\left(1 + N/t_c R_{sp} P\right) - 2\Gamma_N\right)\right\}}{P\left\{\left(\Omega_R - w\right)^2 + \Gamma_N^2\right\}\left\{\left(\Omega_R + w\right)^2 + \Gamma_R^2\right\}} \tag{1.1}$$

where w is the frequency, Ω_R and Γ_R and the frequency and the damping rate of relaxation oscillations, G_N is the modal differential gain, R_{sp} is the spontaneous rate of emission, P is the optical photon density, t_c is the carrier lifetime, and Γ_N is small signal carrier decay rate.

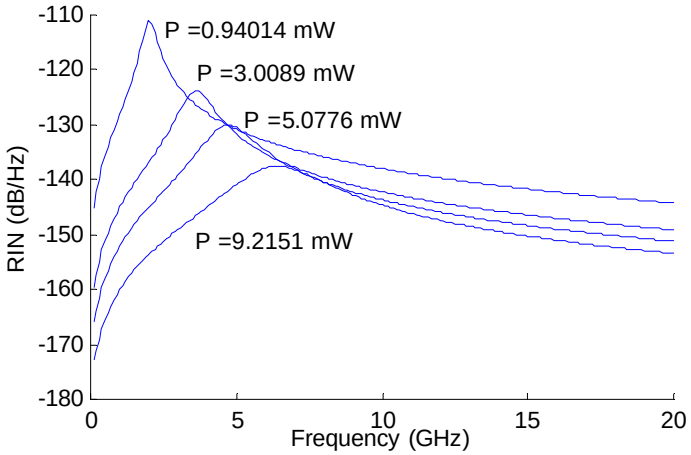

Figure 41 – RIN of a typical semiconductor laser

The RIN of a typical laser is plotted in Figure 41. As seen in the figure, the noise power is reduced for a higher optical power. At a low power level (and for high power level if the noise is shot-noise dominated), for frequencies below the relaxation oscillation frequency, the relative intensity noise is given by [92]:

$$RIN(w) \approx \frac{2R_{sp}w^2}{P\Omega_R{}^4} \tag{1.2}$$

Thus, in a free-running laser, the noise is decreased for an increasing optical power and for an increasing resonance frequency. Indeed, low RIN lasers typically feature a high output power and high oscillation frequency.

Injection-locking has been shown to lead to an increase in optical power and an increase in laser resonance frequency by a factor of 3. For such a large increase in resonance frequency, one would expect the noise to be substantially reduced at low frequency. This observation has motivated the study to follow of noise in injection-locked lasers.

VCSEL RIN was measured to be less than -150 dB/Hz up to 5 GHz [93]. Further demonstration showed that the RIN can be made lower than the Poisson shot noise [94].

4.2. Injection-Locked Laser RIN

Noise of injection-locked lasers has been studied by similar approaches as for free-running lasers [11, 19, 32, 95-100]. The first models [11, 95, 96] assumed that the follower laser was locked in the noise analysis. In 1986, N. Schunk and K. Petermann [19] extended the model by considering the general case where it was not assumed that the follower laser is locked. This allowed for the possibility that noise in the master or follower could lead to unlocking. Of the theoretical noise simulations, several models [19, 97, 98] did not predict a resonance frequency enhancement.

In the RIN simulations in [19], the authors chose to evaluate the RIN at 800 MHz. A reduction in RIN at that frequency is predicted in the range of -2.1 GHz < d < -1.75 GHz, for an injected power of 6 uW, with a linewidth enhancement factor, $\alpha = 3$. The improvement was seen over the full locking range, and is shown in Figure 42, where the

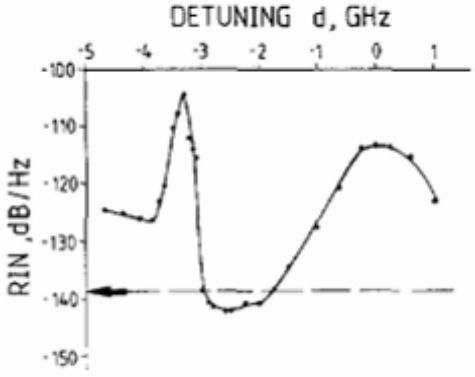

Figure 42 - Simulated RIN of injection-locked laser [19]

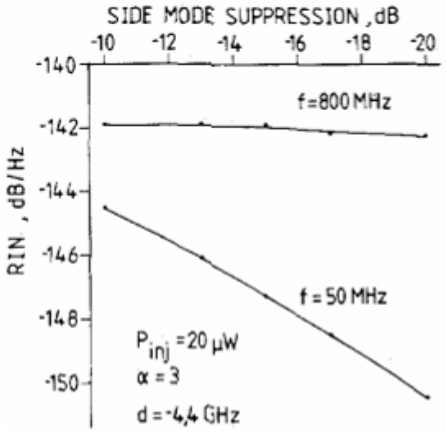

Figure 43 - Simulated influence of master side-mode suppression on laser RIN [19]

free-running RIN is -139 dB/Hz. For an injected power of 20 uW, the RIN improvement range increase to 1 GHz. For $\alpha = 6$, no RIN improvement was observed.

It was also predicted that the side-mode suppression of the master laser plays an important role in the low-frequency RIN of the follower laser. Additionally, for higher power injection, a low master side-mode suppression ratio (SMSR) leads to an even greater follower low-frequency RIN. Shown in Figure 43, the RIN at low frequency (50 MHz) decreases as the SMSR of the master increases. The high frequency RIN (800 MHz) is unaffected by SMSR.

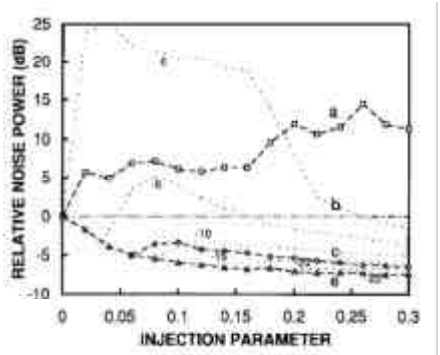

Figure 44 - Simulated RIN reduction [99]

Simulations using the noise driven rate equations have shown that it is possible to simultaneously achieve a bandwidth enhancement, noise reduction and stable locking [99]. In this analysis, the total noise was determined, and shown to decrease by about 5 dB relative to the free-running case, as shown in Figure 44. At this condition, -10 GHz detuning for an injection parameter of ξ=0.3, the resonance frequency was tripled to a value of 9 GHz. It was also pointed out that for a higher follower laser bias, the noise reduction would not be as dramatic since in that case, the follower laser is less noisy to begin with. The analysis considered Langevin noise terms only for the photon and phase, neglecting the noise terms for the electrons. Thus, no cross-correlation term between electrons and photons was included. Master laser noise was not included.

Further simulation results were obtained in [98], where the noise terms were included to model observed discrete jumps in the optical phase, attributed to momentary

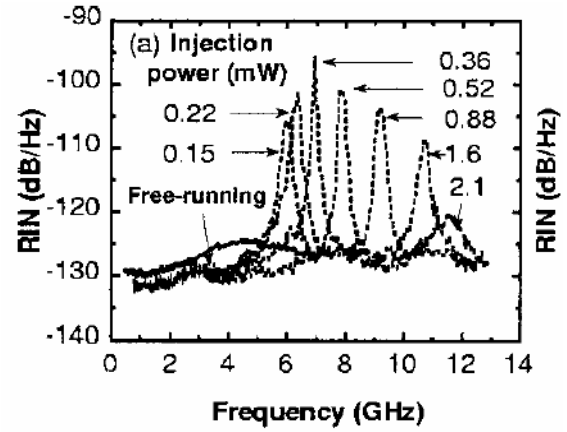

Figure 45 – Experimental and simulated injection-locked RIN [32]

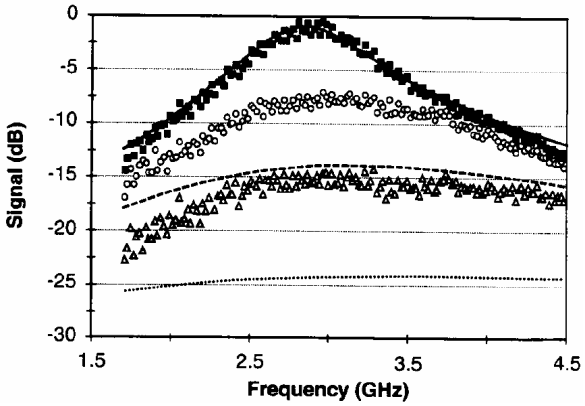

Figure 46 - Experimental injection-locked RIN [31]

lock loss owing to spontaneous emission.

In [100], linearization of the rate equations was performed to simulate the noise characteristics of locked lasers. The master laser noise was included in the analysis. A resonance frequency enhancement and RIN reduction was predicted. It was found that the locked laser exhibits lower noise than when free-running, but the noise is always higher than the master laser. The noise is related to the CNR for sub-carrier multiplexed systems (SCM). Important to reduce noise for AM SCM, but doesn't improve performance for FM-SCM. In the simulation, the free-running laser provides a CNR of only ~40 dB, which is increased to > 50 dB with injection-locking.

4.2.1. Prior experimental measurements of injection-locked RIN

Early experimental results [101] indicate that the laser RIN is always higher in the injection-locked case than in the free-running mode. The experiments were performed in the weak-injection regime with a large alpha parameter of 7.

Recently, experimental demonstration of injection-locked RIN was published [31]. The results indicate that a resonance frequency enhancement is present in the RIN spectra. For low frequency, a small decrease in RIN is observed, shown in Figure 46.

S. L. Chuang argues that RIN reduction is a result of the injected signal reducing the cavity gain and depleting the carrier density, therefore reducing the spontaneous emission rate [31]. As a result, more photons are coupled in phase into the amplified injection field, and enhance the relaxation frequency. Although this description provides some intuitive understanding, it does not present a complete explanation. Our simulations have shown that RIN is decreased even if the rate of spontaneous emission is assumed constant when the laser is locked. Thus, it is the dynamics of the injection-locked rate equations themselves that lead to a reduction in the RIN.

In experimental work by Simpson [32], a broadband noise reduction due to injection-locking was observed, shown in Figure 45. The top curve is for the free-running laser, while the other curves are for the injection-locked cases. The authors define an "injection parameter", ξ, which describes the amount of injection power relative to the cavity power. In the injection cases plotted, ξ=0.06 and 0.20. ξ = 0.05 corresponds to a locking range of 12 GHz.

4.3. RIN Simulations

In this section, the relative intensity noise of injection locked VCSELs is simulated. Two methods were used for the simulations: 1) an analytic small-signal model, and 2) a numerical solution of the injection-locked rate equations.

The analytic model is much faster to evaluate, and principle could be used to make predictions on trends for changes in parameters. Analytic formula could be used for this purpose. However, because of the complexity of the system, no easy analytic solutions to the small-signal model could be found. For RIN in particular, the expression is three times longer since it involves three Langevin modulation terms, whereas the small-signal response only involves the small-signal current modulation.

Although the numerical simulations are more computationally time consuming than the analytic model presented in Chapter 2, the results are more accurate since they include the photon number and carrier number changes due to locking. Additionally, the numerical model does not include any small-signal approximations, thus can be used for large signal digital modulation. The simulation code was implemented in Matlab, and is shown in Appendix A.

Throughout this thesis, the numerical model is used consistently, so that the noise calculations can be related to the distortions and meaningful dynamic range values can be determined.

4.3.1. Analytic RIN model

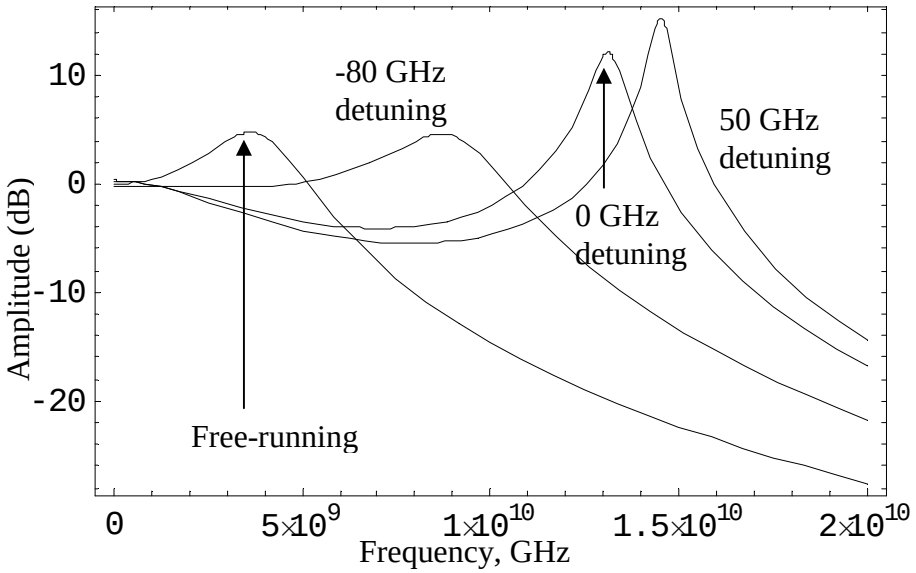

Figure 47 - Analytic simulation results for small-signal modulation
Detuning values are -80, 0, and 50 GHz, kc=3.8e12, Sinj/S = -30 dB, alpha=3

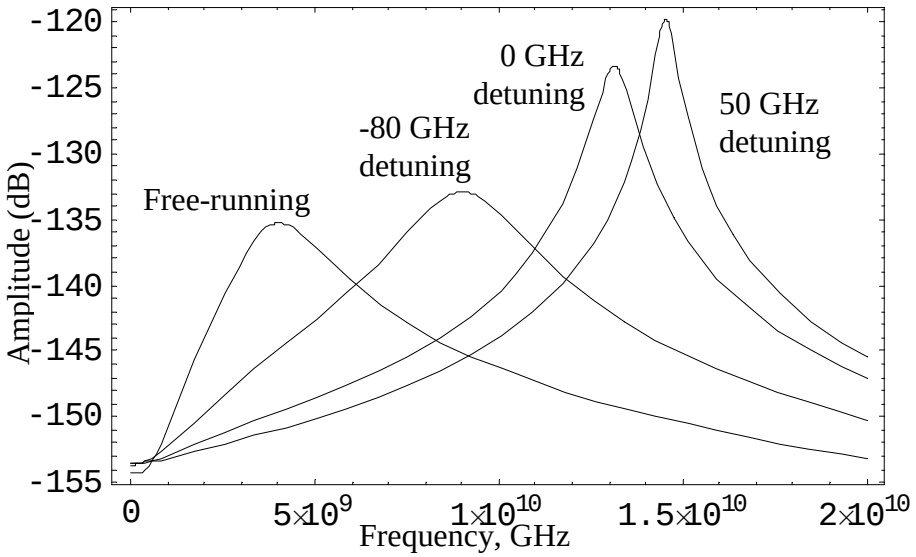

Figure 48 - Analytic simulation results for relative intensity noise
Detuning values are -80, 0, and 50 GHz, kc=3.8e12, Sinj/S = -30 dB, alpha=3

Using the small-signal analysis in Chapter 2, analytic results for the small signal current modulation and relative intensity noise are presented in this section. The small-signal amplitude modulation frequency response is shown for comparison, in Figure 47. The injection ratio is -30 dB, with detuning values of 50, 0, and -80 GHz chosen. The resonance frequency is increased from 4 to between 10 and 15 GHz, depending on the detuning.

Figure 48 shows the calculated noise spectra for the free-running and injection-locked cases. The noise of the injection-locked laser is reduced for the frequency range of 1-6 GHz, and the resonance frequency is increased as in the small-signal response.

In both figures, the damping rate is small for the 50 GHz detuning, and the locked frequency responses exhibit a sharp resonance peak. The damping rate is much higher the -80 GHz detuning case, leading to a flatter small-signal modulation frequency response curve.

From the analytic noise solution, it is also found that the various Langevin noise terms contribute to the total RIN.

4.3.2. Numerical RIN simulations

In our rate equation model, Langevin noise terms are included, and the equations follow the form similar to that used in [19]:

$$\frac{dS}{dt} = \frac{G_0(N-N_0)}{1+eS}\cdot S - \frac{S}{t_p} + 2k_c\sqrt{S\cdot S_{inj}}\cdot\cos(\,f(t)-f_{inj}\,) + R_{sp} + F_s$$

$$\frac{df}{dt} = \frac{a}{2}G_0(N-N_{th}) - 2p\cdot\Delta f - k_c\sqrt{\frac{S_{inj}}{S}}\cdot\sin(\,f(t)-f_{inj}\,) + F_f \qquad (1.3)$$

$$\frac{dN}{dt} = \frac{I}{q} - \frac{N}{t_s} - \frac{G_0(N-N_0)}{1+eS}\cdot S + F_n$$

$$F_s = \sqrt{\frac{2S\cdot R}{\Delta t}}x_e$$

$$F_f = \sqrt{\frac{R}{2S\cdot\Delta t}}x_f \qquad (1.4)$$

$$F_n = -F_s + \sqrt{\frac{2N}{t_s\cdot\Delta t}}x_n$$

R is the spontaneous rate of emission. The Langevin noise is modeled by the variables x_e, x_ϕ, x_n, which are uncorrelated Gaussian random variables with zero mean and unity variance, and Δt is the ODE solver step size. The cross-correlation between the photons and electrons is thus -1.

In the numerical solution, the integration step size, Δt, must be small enough so that the noise terms appear as a "white" noise source. For a step size of 50 ps, the noise power spectral density has a 3 dB cut-off at about 9 GHz [19]. Thus, the relaxation oscillation of the follower laser must be much smaller than $1 / 2\Delta t$. A fixed step size is preferred over a variable step size (as implemented in MatLab) since the variable step differential integrator will reduce it's step size to extremely small values leading to unreasonably long computation times.

In the simulations, the master laser rate equations were solved numerically. The steady state values of the photon number and lasing frequency were used as the injection terms. Thus, the noise in the master laser was not considered in the analysis. Such an analysis drastically increases the computational time.

Numerical simulations show that for the free-running laser, the dominant term in the noise calculations is F_S. For the injection-locking case, however, all Langevin noise terms are necessary in the noise calculation.

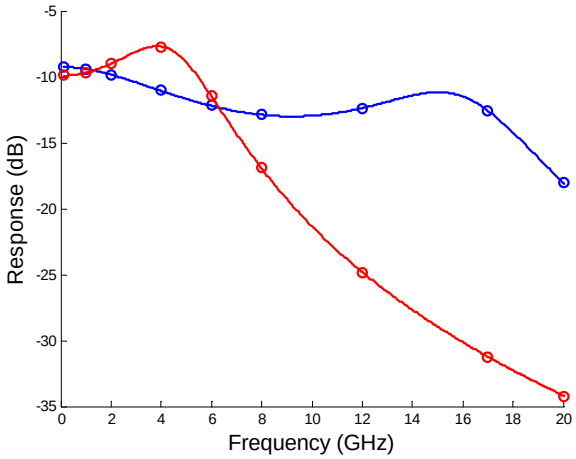

Figure 49 - Simulated S21 of an injection-locked laser

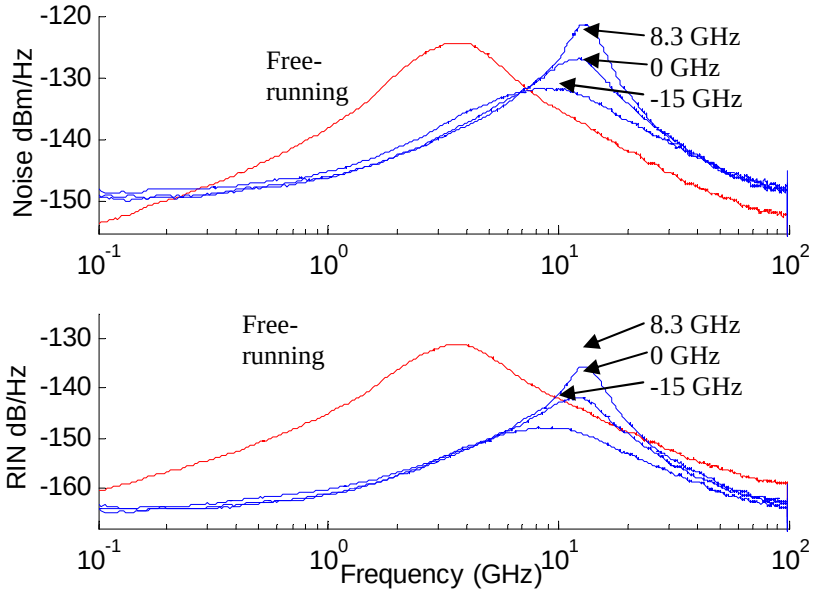

Figure 50 - Simulation of injection-locked laser noise and RIN
The top plot is the laser noise, free-running and injection-locked.
The bottom plot is the relative intensity noise, free-running and injection-locked.
Alpha = 3, injection ratio -30 dB; detuning values of 8.3, 0, -15 GHz, log frequency

Simulation results

For a detuning of 8.3 GHz, and injection ratio of 1e-3, the small-signal modulation response is shown in Figure 49. The gain compression factor was chosen to be 20e-8, which is higher than typically published values. It was chosen to give closer match to the S21 experimental results. The linewidth enhancement factor was α=3. The figure shows that the free-running resonance frequency (4 GHz) is increased to ~15 GHz for the locked case.

In Figure 50, the RIN for free-running and injection-locked cases are shown, for the

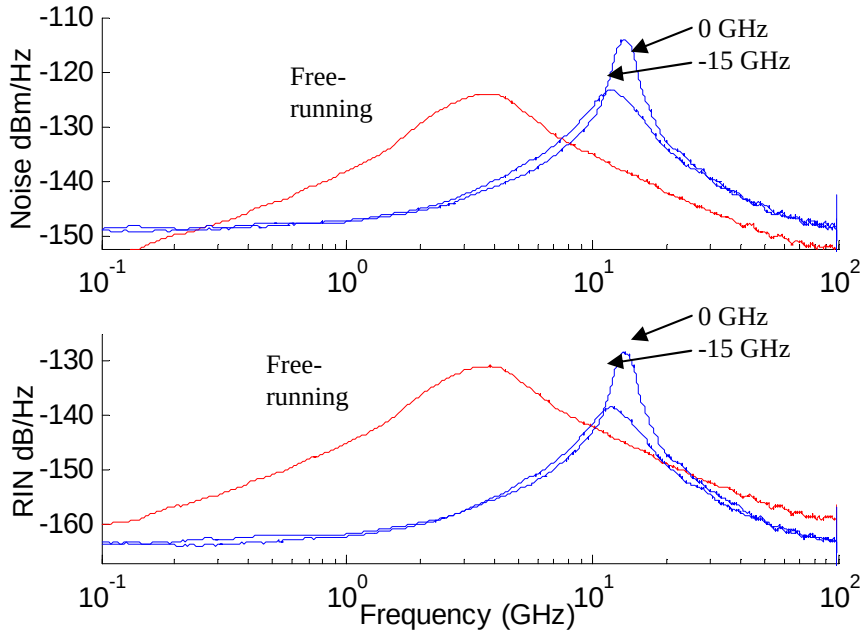

Figure 51 - Simulation of injection-locked laser noise and RIN
The top plot is the laser noise, free-running and injection-locked.
The bottom plot is the relative intensity noise, free-running and injection-locked.
Alpha = 6, injection ratio -30 dB; detuning values of 0, -15 GHz, log frequency

same conditions. The simulation was conducted for a time interval of 400 ns. The resonance frequency peak in the RIN spectra matches that of the small-signal modulation resonance peak. The top is the noise power, while the bottom plot is the relative intensity noise (i.e. noise power normalized by the optical power). The plots were also smoothed (with a 3% smoothing function). The injection-locking leads to an increase in optical power, which can further reduce the relative noise. As seen in the figure, the noise drops by 10 dB, while the RIN drops by ~20 dB at half the resonance frequency (2 GHz). We can clearly see that for these conditions, the low-frequency noise actually increases, while RIN stays the same.

Figure 51 shows a similar results, but for a linewidth enhancement factor of 6. The results are similar to the results for a linewidth enhancement factor of 3.

The noise simulations indicate that the relative noise and total noise power are reduced for a large frequency range. In the following simulations, we characterize the total noise power and the total RIN power for free-running and locked cases.

In Figure 52, the detuning is fixed at 0 GHz, and the injection power is varied from 1e-5 to 1e-2. The resonance frequency is shown in increase with injection power, and the noise is reduced from 0 to ~5 GHz for all locking conditions. As the resonance frequency increases, the noise observed at a particular frequency decreases. For example, at 2 GHz, the noise decreases monotonically with increasing injection power. Since master laser noise was not considered, this trend continues indefinitely, predicting that the laser noise continues decreasing as one increases injection power.

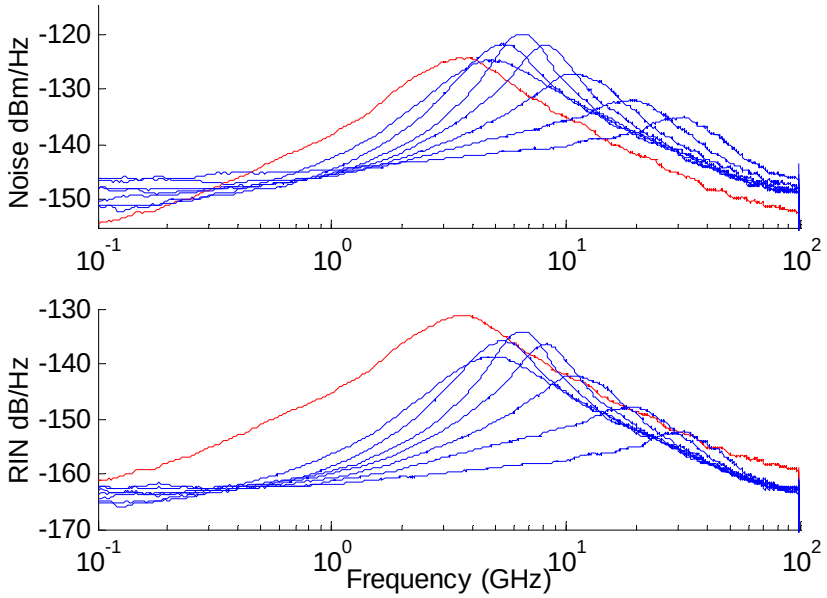

Figure 52 - Simulation of injection-locked laser noise and RIN
Alpha = 3, 0 GHz detuning, varying injection ratio from -50 to -20 dB

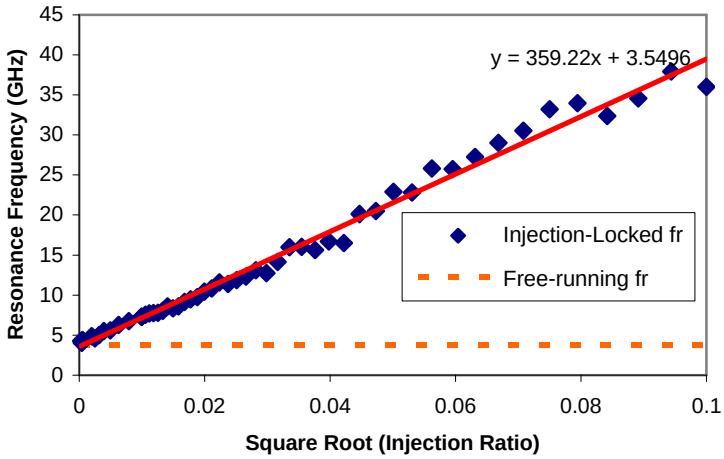

Figure 53 - Simulated resonance frequency vs. square root of injection ratio
The injection-locked resonance frequency is shown to increase as the square root of the injection ratio, for a 0 GHz detuning. The free-running resonance frequency of ~ 4 GHz

The resonance frequency of the injection-locked laser can be estimated by finding the peak of the RIN response shown in Figure 52. As the injection-power is increased, the resonance frequency increases. As shown in Figure 53, this increase does not appear to be bounded in our simulations, with a predicted resonance frequency enhancement from 4 to ~35 GHz for a 0.01 injection ratio. The results are plotted versus the square root of the injection power, since it has been analytically predicted that the resonance

frequency is expected to vary as the square root of injection power [81]:

$$w_r^{\,2} = \frac{v_g \frac{dg}{dn} S}{t_p} + k_c^{\,2} \frac{S_{inj}}{S} + \ldots \tag{1.5}$$

In Figure 54, the total noise power and RIN decrease with locking is plotted versus injection power. An integration of the noise was performed between 0 and 3.5 GHz. 3.5 GHz was chosen since it corresponds to the free-running resonance frequency. A monotonic and unbounded decrease is predicted for both quantities, for increasing injection power. The simulation did not, however, include the master laser noise. The master laser noise would limit how low the follower laser will become.

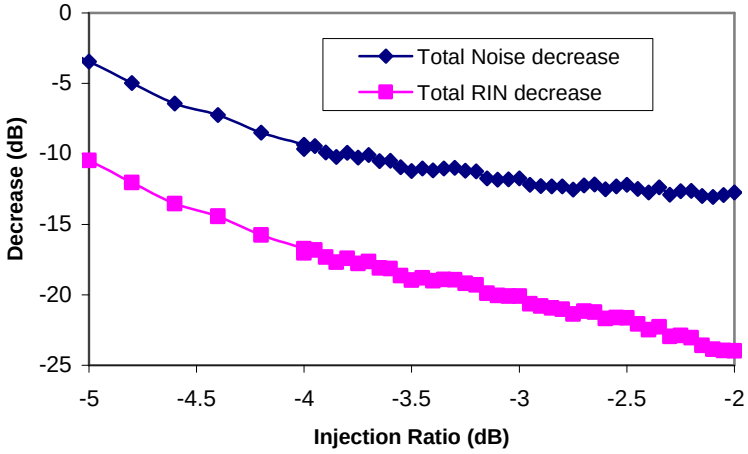

Figure 54 - Simulation of injection-locked total laser noise and total RIN decrease
Alpha = 3, 0 GHz detuning

Simulations were performed throughout the locking range. 10,000 locking conditions were simulated. The injection-locked results were compared to the free-running simulation results. The difference between the locked and free-running results serve as a comparison.

The results are plotted in Figure 55, for the total noise power difference between 0-3.5 GHz. In general, the noise is decreased for a higher injection power. The noise power is also smallest for a negative wavelength detuning (where the RIN spectra show a sharp peak due to the small damping frequency).

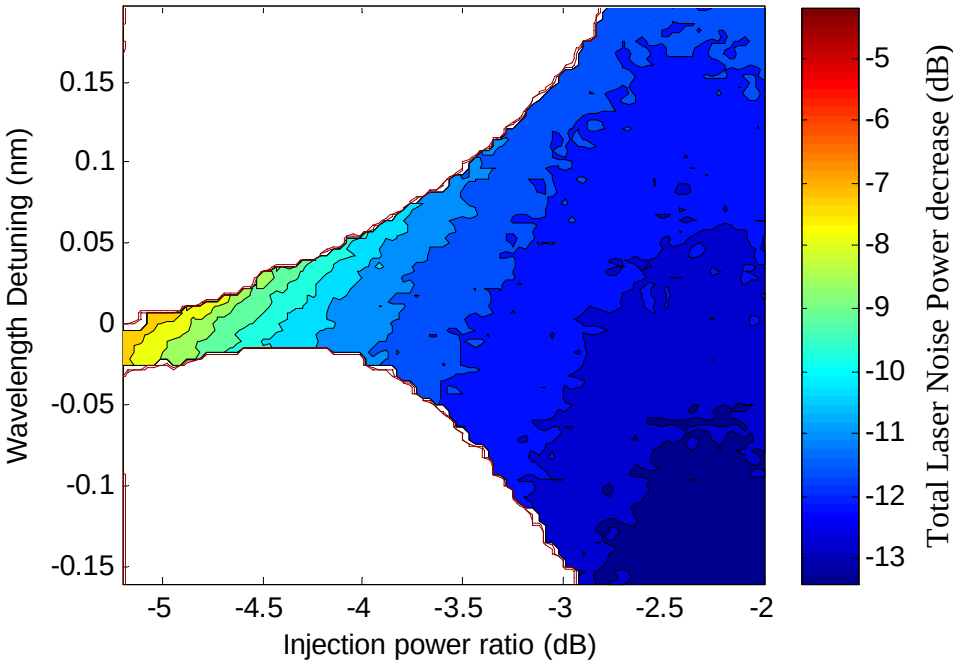

Figure 55 - Simulation of injection-locked total laser noise decrease
Noise integrated between 0-3.5 GHz, alpha = 3, for varying detuning and injection power.

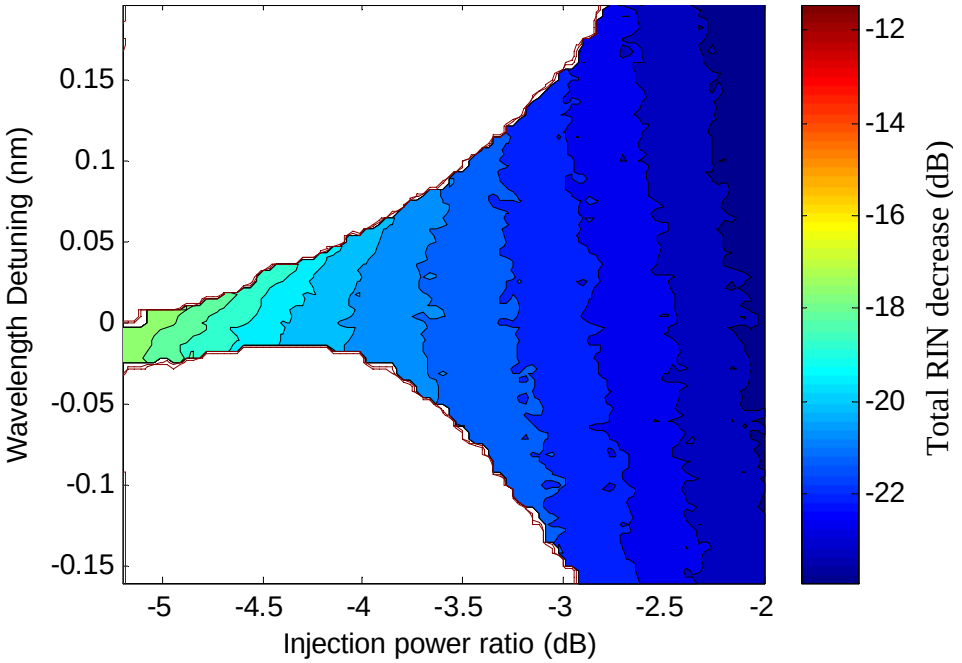

Figure 56 - Simulation of injection-locked total RIN decrease
Noise integrated between 0-3.5 GHz, alpha = 3, for varying detuning and injection power. Note that locked optical output power increases for increasing positive detuning, hence RIN, which is normalized to output power, actually decreases.

The RIN decrease is shown in Figure 56. Again, the RIN is integrated from 0 to 3.5 GHz, and compared to the free-running case. When considering total RIN, the trend is opposite to the total noise, in that the lowest total RIN occurs for the highest detuning.

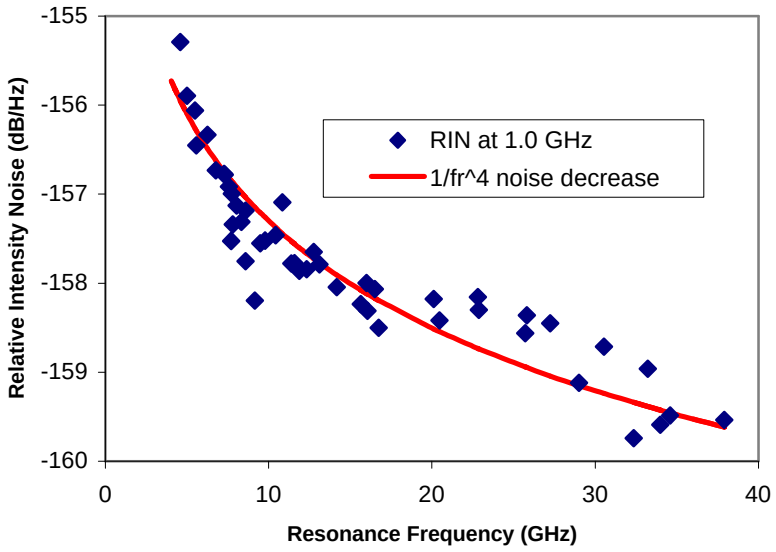

Figure 57 - Simulation of injection-locked RIN at 1.0 GHz vs. resonance frequency
The total noise decreases as $1/f_r^4$, even for injection-locking. Simulations were performed for alpha = 3, and a 0 GHz detuning. The injection power was varied and the resonance frequency observed.

This is because the locked laser output power is higher for the largest positive wavelength detuning. Since RIN is defined to be inversely proportional to the laser output power, we observe an overall decrease in the RIN for highest detuning.

For a free-running laser, the low frequency noise decreases as the fourth power of the resonance frequency, $1/f_r^4$, equation (1.2). It is interesting to determine how the injection-locked laser noise varies with resonance frequency. Simulations were performed at a 0 GHz detuning for varying injection power. The resonance frequency was determined by finding the peak in the frequency response, and the RIN was simulated for a 1.0 GHz frequency (below the free-running resonance frequency ~ 4 GHz).

The results are plotted in Figure 57. For reference, the free-running laser RIN at 1.0 GHz is simulated to be -144.5 dB/Hz. In the figure, the free-running low-frequency laser RIN dependence on relaxation oscillation frequency, following equation (1.2), is also plotted for comparison. As can be seen, the injection-locked laser RIN is in good agreement with the free-running laser behavior for an increasing relaxation oscillation frequency. Thus, we find that the injection-locked low-frequency RIN follows a behavior similar to a free-running laser, with

$$RIN_{Injection-locked,\ low\ frequency} \propto \frac{1}{f_r^{\,4}} \qquad (1.6)$$

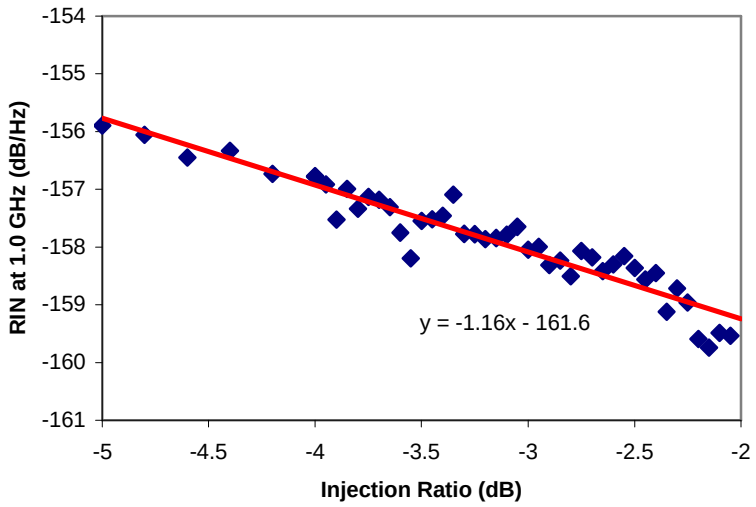

Figure 58 - Simulation of injection-locked RIN at 1.0 GHz
Alpha = 3, 0 GHz detuning, varying injection power.

For a free-running laser, the low frequency noise decreases as the inverse of the optical power, equation (1.2). In the case of injection-locking, the injection photons also contribute to an increase in the photon density of the cavity. Thus, it is interesting to determine how the injection-locked laser noise varies with injection power. The same simulations are plotted versus injection ratio, and shown in Figure 58. The results show a good linear fit with a slope of ~ 1, thus, for injection-locking,

$$RIN_{Injection-locked,\ low\ frequency} \propto \frac{1}{injection\ power} \tag{1.7}$$

4.4. RIN Reduction Experiments

Optical injection locking has been demonstrated to increase the laser bandwidth and reduce the laser chirp and distortion. Around 3x enhancement in relaxation oscillation with increased modulation efficiency at low frequencies was reported [102]. The improved frequency response, combined with the reduced laser nonlinearity, can be very attractive for analog modulation applications. This technique also has the potential to reduce the laser noise. For a RIN-limited analog system, this implies an even higher spur-free dynamic range (SFDR). Although the RIN reduction due to injection locking has been theoretically predicted [99], there have not been many experimental results [31]. Direct RIN measurement of an injection-locked laser for different injection conditions are described in this section.

Preceding the results, the following section describes the theory of RIN measurements using EDFAs.

4.4.1. Measuring laser noise (RIN) of low-power lasers using optical amplifiers

Measurement techniques for RIN have been well documented [103]. For example, using the Agilent 71401C Lightwave Analyzer, it is easy to measure RIN for high power signals (~0 dBm). However, for signals low as –10 dBm, the thermal noise of the detector and amplifier limit the RIN measurements to 120-130 dB/Hz. In this section, we first qualitatively study the problem of measuring lower power signals, and then describe a measurement technique for lasers with RIN values lower than this limit.

Noise sources in RIN measurements

Measurement of the laser noise requires an understanding of the various noise sources that play a role in the measurement. These include the detector thermal noise and the shot noise due to the quantum nature of the photon arrival at the detector. The thermal noise power spectral density is given by $N_{Thermal} = 4kT/R_L \cdot F_N$, where R_L is the receiver load resistance, F_N is the receiver noise figure. For an electrical bandwidth B_e, the variance of the total thermal noise is given by $s_{Thermal}^2 = 4kT/R_L \cdot F_N \cdot B_e$. Shot noise is proportional to the signal power, and is defined as $N_{Shot} = 2 \cdot e \cdot P_{Optical-Avg} \cdot R$, where R is the detector responsivity, and $P_{Optical\text{-}Avg}$ is the power incident on the detector.

One can define the contribution of the thermal noise and shot noise to the RIN measurement. These are called $RIN_{Thermal}$ and RIN_{Shot}, and follow the same definition as laser RIN, where $RIN_{Laser} = \frac{s_{Laser-Optical}^2}{P_{Optical}^2} = \frac{N_{Laser-Electrical}}{P_{Avg-Electrical}}$, where $P_{Avg\text{-}Electrical}$ is the average power of the optical signal converted to electrical units, and $N_{Laser\text{-}Electrical}$ is the laser noise power spectral density in electrical units. Thus, we define as $RIN_{Thermal} = \frac{N_{Thermal}}{P_{Avg-Electrical}}$ and $RIN_{Shot} = \frac{N_{Shot}}{P_{Avg-Electrical}}$. The total noise power measured is also normalized in the same way, and is the summation of the individual noise terms:

$$RIN_{System} = \frac{N_{System}}{P_{Avg-Electrical}} = RIN_{Shot} + RIN_{Thermal} + RIN_{Laser}$$

$$RIN_{System} = \frac{N_{Shot}}{P_{Avg-Electrical}} + \frac{N_{Thermal}}{P_{Avg-Electrical}} + \frac{N_{Laser}}{P_{Avg-Electrical}}$$

Figure 59 illustrates the measurement principle. The measured system noise is the summation of the individual noise terms. In this case, the laser noise is the dominant noise term for f < 15 GHz, and can easily be measured. For f > 10 GHz, the thermal noise is at the same order of magnitude as the laser noise, thus, needs to be subtracted from the measured system noise to give the laser noise value. This subtraction technique in practice can work for laser noise that is about 10 dB lower than thermal noise, though the measured data usually suffers from a high degree of noise.

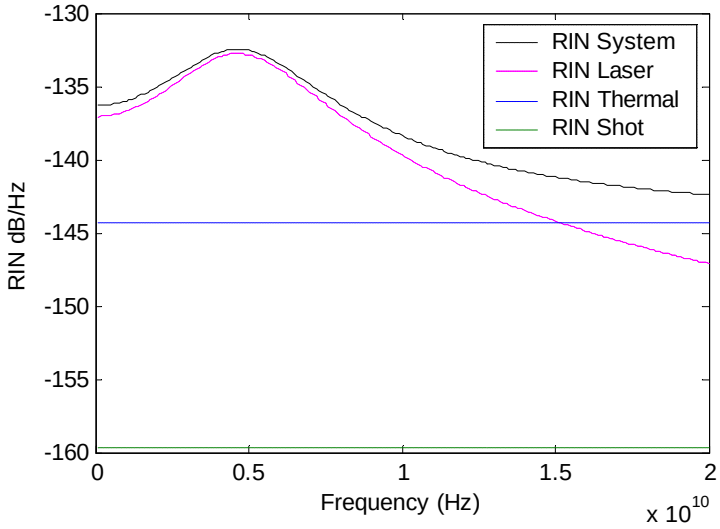

Figure 59 – Simulated measurement results of RIN for a 0 dBm output power VCSEL

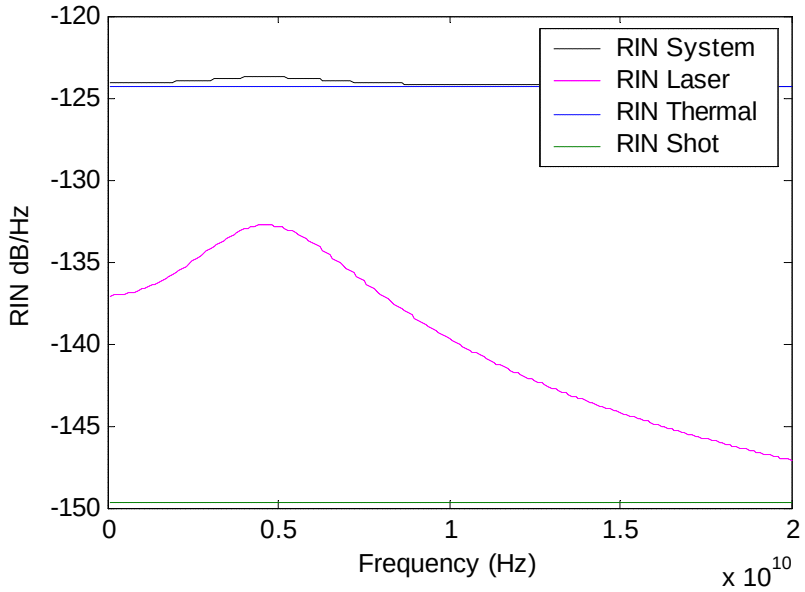

Figure 60 - Simulated measurement results of RIN for a -10 dBm output power VCSEL

Direct RIN measurements using a detector

In this section, we simulate the RIN measurement as would be performed using a detector and RF spectrum analyzer.

In Figure 60, simulations are shown for a RIN measurement performed with an HP Lightwave Analyzer, for a VCSEL with –10 dBm fiber coupled optical power. The laser RIN calculation is performed with the laser parameters adjusted to give results similar to measured values, and represents a hypothetical laser. For the thermal noise contribution to RIN, the values were matched to the specifications in the instrument manual.

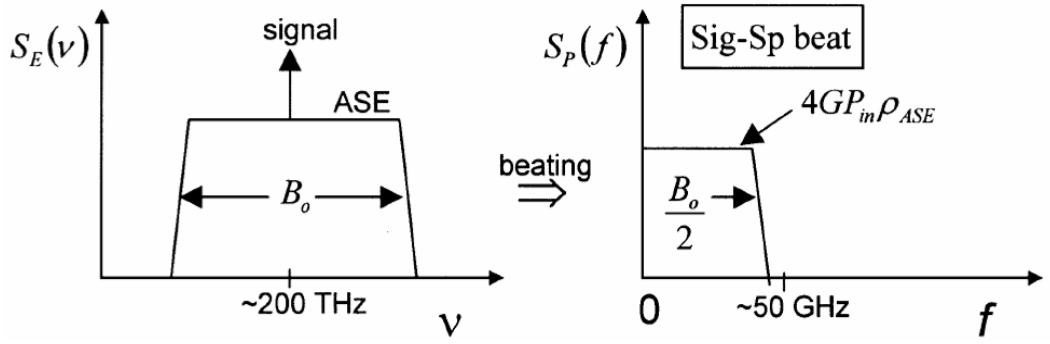

Figure 61 – Noise distribution due to signal-spontaneous emission beating. [104]

As shown in Figure 60, the laser RIN has a peak value of approximately -133 dB/Hz. The thermal noise contribution is -124.3 dB/Hz, which is much greater than the laser noise. Adding the noise terms, the total noise (RIN system) is -123.7 dB/Hz. In an experimental setup, the measurement of the system noise would be very similar to the thermal noise, thus an accurate measurement of the laser noise is difficult to achieve. A high amount of averaging could be employed; however, only the RIN peak would be observed, rather than the full RIN spectrum. Thus, the direct detection of laser noise for signals as weak at -10 dBm is difficult to achieve with the available equipment.

RIN measurements using optical amplifier

One method of increasing the RIN measurement sensitivity is to include an optical amplifier; an erbium-doped fiber amplifier (EDFA), or a semiconductor optical amplifier (SOA) can be used. The amplifier increases the optical power, thus the measurement should no longer be thermally limited. However, the optical amplifier introduces additional noise terms, with the signal-amplifier spontaneous emission being the dominant. In this section, simulated RIN measurements are calculated, demonstrating the applicability of the optical amplifier for these measurements.

The addition of an optical amplifier increases the optical signal. RIN is defined as the ratio of the noise power spectral density of the photocurrent to the average electrical power of the signal. Thus, RIN measurement is normalized to optical power, hence the measurement should be independent of the power incident on the detector. In the measurement system, the thermal noise is independent of optical power, hence as the optical power increases, the thermal noise contribution to RIN ($RIN_{thermal}$) decreases, as the square of the optical input power. Similarly, shot-noise RIN also decreases, proportional to the optical input power.

The optical amplifier does add amplified spontaneous emission (ASE), which when incident on the detector, contributes to the noise. The noise due to amplifier is apparent at the detector. Because optical intensity detectors (ex. PIN detectors) are square-law detectors, i.e. $i(t) \propto P(t)^2$, there is a beating of terms: signal-signal, signal-ASE, and ASE-ASE. The signal-ASE is usually the dominant amplifier induced noise term. The signal-ASE noise is $N_{Sig-Sp} = 4Gain \cdot P_{Sig-Sp} \cdot R \cdot N_{ASE} \cdot R$, where Gain is the optical amplifier gain, $P_{Sig\text{-}In}$ is the optical power input to the optical amplifier, and the ASE noise power spectral density is $N_{ASE} = P_{ASE} / B_O = 2n_{sp}(Gain - 1)hn$, where n_{sp} is

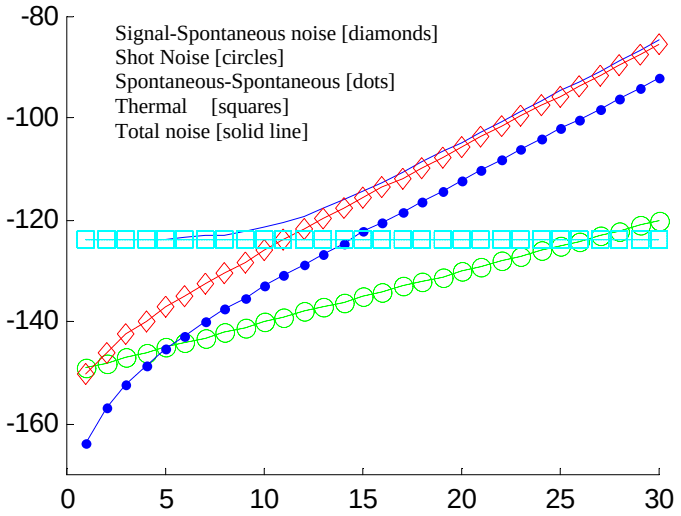

Figure 62 – Optical amplifier noise vs. optical gain

approximated to Noise Figure / 2 (assumption valid for high gain). Note that as shown in Figure 61, the signal-spontaneous emission beating noise has a uniform spectral density, with a magnitude that is independent of the optical bandwidth. In Figure 61, SE(ν) is the optical field spectral power density and SP(ν) is the electrical power spectral density at the detector. The optical bandwidth of the filter is assumed to be ~50 GHz in this case.

The noise figure definition for optical amplifiers has seen much debate and confusion regarding its definition. The most commonly used definition assumes a high gain optical amplifier (> 10 dB), and an electrical signal-to-noise (SNR) measurement using a shot-noise light source with a detector that is not thermally limited. In practice, this may not be the case, thus the noise contribution of the optical amplifier will not be a simple degradation in SNR. This is discussed in detail two papers [104, 105]. In practice, the SNR following an optical amplifier is usually dominated by thermal noise or by laser RIN. In the absence of these noise terms, the SNR is directly dependant on the noise figure.

Figure 62 shows a simulation of the optical noise power as measured by a typical PIN detector for the detection of a low power optical signal. The optical gain of the amplifier is varied (by varying the length of the optical fiber), and the fiber population inversion factor is maintained constant. The total noise is dominated by signal-spontaneous noise (RIN_{EDFA}) for a high optical gain, while it is thermal noise ($RIN_{Thermal}$) dominated for low optical gain. Spontaneous-spontaneous beating noise and shot noise do not contribute significantly to the total noise.

In Figure 63a, an EDFA (Optical Gain 20 dB, Noise Figure 4 dB) and an optical filter (100 GHz optical bandwidth) are introduced in the RIN measurement system. The signal-ASE noise contribution to RIN is $RIN_{EDFA} = N_{EDFA} / P_{Avg-Electrical}$ is –146 dB/Hz, which is much smaller than the laser RIN. Thus, compared to Figure 60, we see that the system is no longer thermally limited (RIN Thermal = -164 dB/Hz). The other noise terms are shot-noise RIN, at -170 dB/Hz (which is dependant on the optical bandwidth)

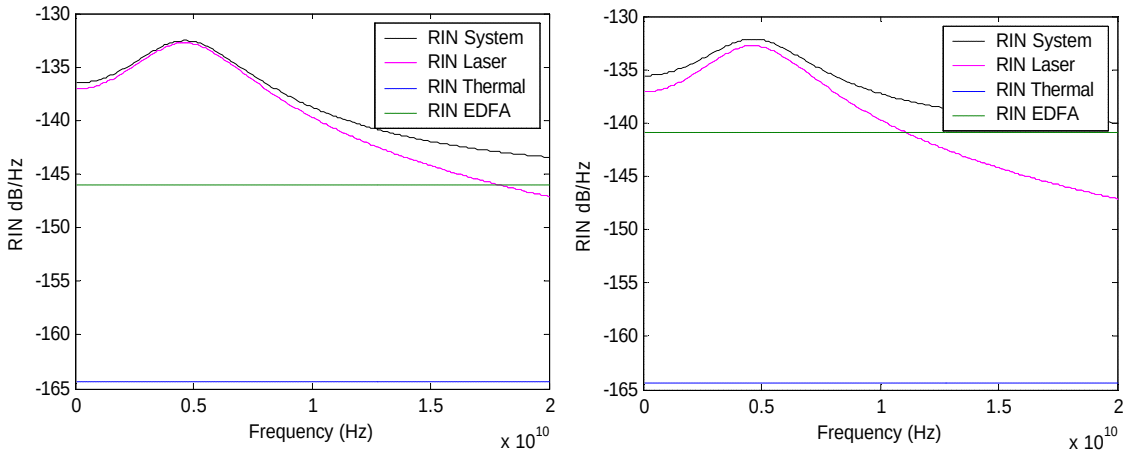

Figure 63 - Theoretical VCSEL RIN
Measured using: a) an EDFA (left), and b) an SOA (right).

and EDFA spontaneous emission beating, at -187 dB/Hz, which are both in the case negligible. Figure 63b shows the same calculation using a semiconductor optical amplifier (Optical Gain 20 dB, Noise Figure 9 dB). In this case, the signal-AES noise contribution to RIN is RIN_{SOA} = -141 dB/Hz and is 5 dB higher, but the signal is still visible. Thus, for this case, either an EDFA or SOA will allow a measurement of the laser RIN.

The optical filter in these measurements is unnecessary, since the noise is dominated by the signal-spontaneous beating noise, which is optical bandwidth independent. Even for the case of NF = 12 dB, Pin = -10 dBm, Bo = 40 nm, which represents a very noise optical amplifier without an optical filter, we find that the spontaneous-spontaneous beating term only contributes -151 dB/Hz to the RIN measurement. In this case, the sig-sp contribution is -138 dB/Hz, and again dominates the measurement. Thus, the use of an optical filter is unnecessary when measuring RIN using an optical amplifier.

4.4.2. Experimental Setup

The noise of the injection-locked laser was characterized using the experimental setup, shown in Figure 64.

A 1.55μm-VCSEL [7] is subjected to optical injection from a DFB laser through a circulator. The VCSEL and the DFB (master laser) are biased at 4mA and 100mA,

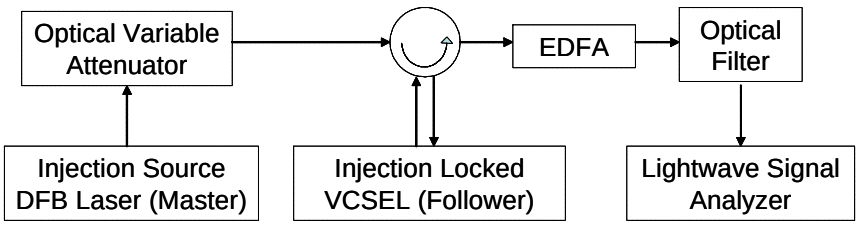

Figure 64 - RIN measurement experimental setup

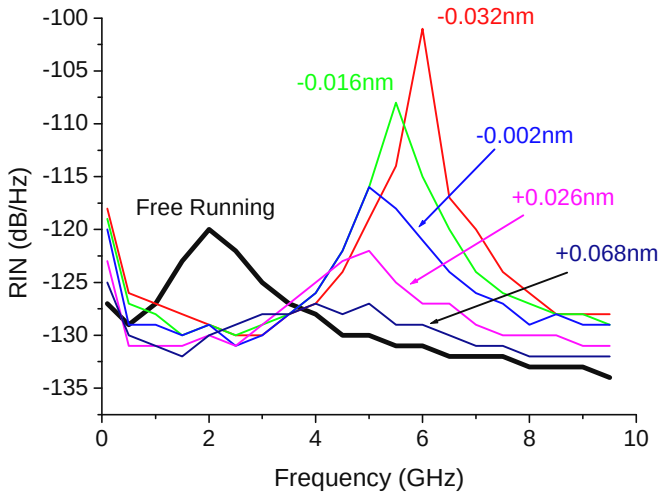

Figure 65 - Experimental Injection-locked RIN spectra. DFB attenuated by 10 dB.

respectively. The wavelength detuning (= λ_{DFB} - λ_{VCSEL}) between the two lasers are controlled by temperature tuning the DFB and the injection power is varied with an optical attenuator before coupling the DFB signal into the circulator. At the output port of the circulator, the signal is amplified by an EDFA and optically filtered to improve the measurement sensitivity, as described in the previous section. An HP 71401C Lightwave Signal Analyzer is then used to measure the RIN of the injection-locked VCSEL. The RIN spectra were averaged with 100 traces, and 20 frequency points were downloaded.

4.4.3. Measurement Results

In the injection-locking experiments, the master laser was a DFB with a 9 dBm optical power. The coupling loss of the VCSEL to fiber was ~ 10 dB, due to the lenses used for the coupling, connector loss, and circulator loss. Using this loss, the injected optical power was at most -1 dBm. The VCSEL had a peak power of 400 μW, and was biased at 4 mA, which is half peak power biasing point. Thus, the optical output power of the VCSEL was -7 dBm.

The optical injection power was attenuated by 10 dB, for an injected power of -11 dBm. Thus, the injection ratio was -4 dB. For this injection power, and for several detuning values, the RIN measurement is shown in Figure 65. The free running RIN (thick curve) is shown as the reference. The free-running resonance frequency is ~2 GHz. More than 10 dB of RIN reduction is observed at 2 GHz and the reduction is relatively insensitive to the amount of detuning. The RIN reduction in the low frequency regime (0.5 – 4GHz) is relatively constant at this injection power. For -0.032nm detuning, the RIN peak moves from 2 GHz to 6 GHz, which is a factor of 3 improvement in the resonance frequency. For the cases with negative detuning, the RIN peaks are very sharp with high amplitude, compared to the cases with positive detuning. The RIN peaks are in agreement with relaxation oscillation frequencies of small signal modulation (S21) of the laser. Additionally, the damping in the S21s follows the same trend as the

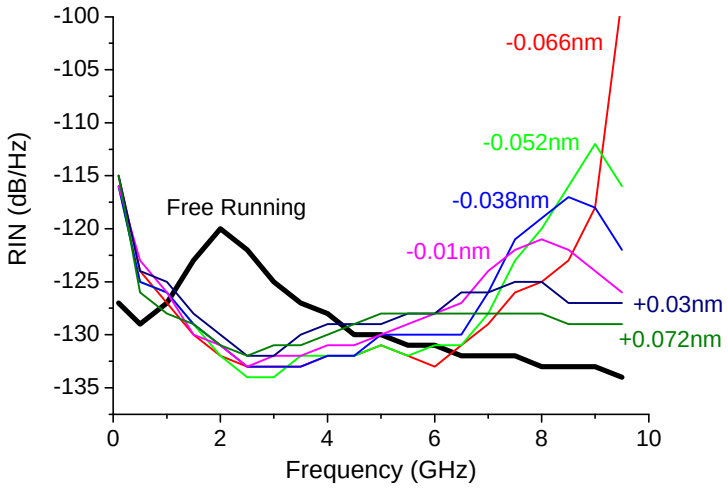

Figure 66 - Experimental Injection-locked RIN spectra. DFB attenuated by 5dB.

damping in the RIN spectra.

For a higher injection power of -6 dBm, corresponding to a 5 dB DFB attenuation and +1 dB injection ratio, the RIN peaks move to an even higher frequency, shown in Figure 66. The resonance frequency reaches a peak of ~10GHz for the –0.066nm detuning condition, which corresponds to a factor of 5 increase in resonance frequency. The reduced noise floor at low frequencies (1 – 4 GHz) appears roughly the same for different conditions, and is reduced for all detuning values. This implies the injection-locking technique can be rather robust for noise reduction. Again, the RIN spectra peak frequencies and shape match the small-signal modulation responses, showing the highest damping for large positive wavelength detuning values.

The measurements are limited due to the EDFA signal-spontaneous emission noise, which is approximately -135 dB/Hz. The EDFA noise was not subtracted in these figures, as the EDFA noise was not characterized at the time of measurement. Thus, the noise floor observed in the measurements is limited by the addition of the EDFA noise. Measurements using a higher power VCSEL would eliminate the need for the EDFA, hence a more accurate noise characterization could be performed.

The free-running RIN spectrum observed did not completely match the theoretical RIN spectrum, which has monotonically decreasing noise value when frequency decreases. An anomalous increase in RIN for frequencies below 1 GHz was observed. One possible reason for the higher noise at low frequencies could be mode-partition noise [106], as the particular VCSEL used in this experiment does not have a very high side-mode suppression ratio. A lower noise at low frequencies is expected if a higher side-mode suppression VCSEL is used. Multiple reflections [107] in the optical setup may also contribute to the increased low frequency noise. In particular, it was observed that FC/PC connectors can increase the low-frequency noise when not completely mated or not perfectly cleaned.

The injection-locked spectra exhibited an even higher noise at low frequencies. In addition to the possible causes discussed above, polarization of the master laser plays a role in the low frequency noise. In experiments performed with polarization maintaining

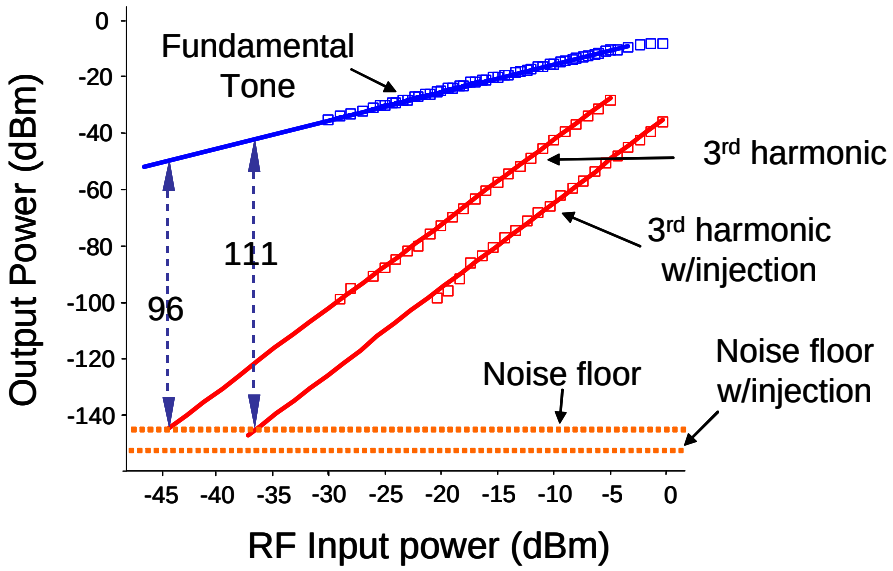

Figure 67 - SFDR Measurement

fibers, the low frequency noise was reduced. It is possible that a mismatch between the VCSEL preferred polarization and the master polarization may increase the low frequency noise; also, in a non-polarization maintaining fiber, the polarization can change rapidly, leading to the observed low frequency noise.

The RIN reduction can be intuitively understood as the following: when the laser is injection-locked, fewer carriers are needed to achieve lasing threshold. The spontaneous emission of the laser, and therefore its noise, is reduced. In addition, since the laser noise is highest at the relaxation oscillation frequency, the enhancement in resonance frequency with injection-locking further reduces the noise value in low frequency regime. The combination of these two factors results in the RIN reduction of an injection-locked laser.

Third harmonic spur-free dynamic range measurements were performed for the same injection-locked VCSEL, at 2 GHz. The measurements show an increase in the SFDR due to a modulation efficiency enhancement and a harmonic distortion reduction. Due to the noise reduction observed, it is expected that the SFDR value will be even further reduced due to the locking technique.

Similar experiments were performed on another laser. In this case, the optical amplifier noise characterized and subtracted from the measurements. The input into the optical amplifier was kept at a constant -8 dB. The optical amplifier was characterized by measuring the system RIN of a DFB laser (with a RIN of -155 dB/Hz) in conjunction with the EDFA. Based on the calculations in the previous section, the RIN spectrum (RIN_{sys}) is assumed to be dominated by signal-spontaneous emission. Thus, the noise measured is essentially the EFDA noise, termed RIN_{EDFA} ~ -135 dB/Hz. As expected, the spectrum is nearly spectrally uniform.

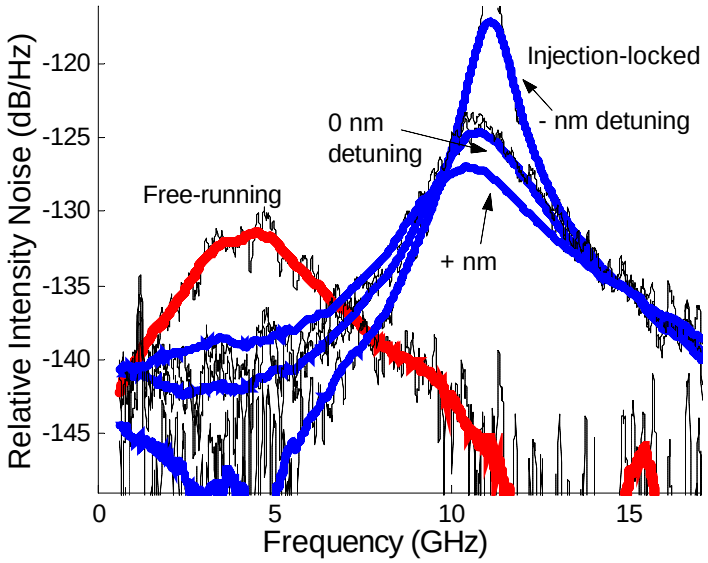

Figure 68 - Injection-Locking RIN Reduction

The measurement results are shown in Figure 68. As can be seen, the noise is lower over a large frequency range from ~0 to 7-8 GHz. For negative detuning values, the lower frequency noise reduction can be very large. For modulation at half the free-running resonance frequency (~2.5 GHz), the noise is found to decrease between 5 and 15 dB, depending on the detuning value.

4.5. Fiber Optic Link Induced Noise

Optical-injection locking in general appears to improve the system performance on all performance metrics. In this section, we discuss the analog fiber system impediment of increased detected noise due to interferometric reflections in the fiber link. It certain situations, it is possible that injection-locking could actually increase the received noise power.

It has been shown that interferometric noise can lead to an increase in detected laser noise [108]. Also, due to the interferometric nature, reflections in the fiber link due to connectors can lead to an increase in the received signal noise [109]. The magnitude of the reflection-induced noise is related to the linewidth of the laser source. The noise is highest for "medium" linewidth signals. The worst ("medium") linewidth depends on fiber length and subcarrier modulation frequency. For a 3 m patch-cord, an RF signal of 300 MHz, the highest noise occurs for a linewidth of 340 MHz, while a 50 MHz signal has a peak at a 34 MHz linewidth. In this study, the patch-cords had reflection coefficients of -30 dB, which is a typical FC/PC connector reflectivity. For negligible reflection-induced noise, the reflection must be less than -43 dB. Since most analog links employ angle-polished connectors (APC) with R= - 60 dB, this type of noise is generally not problematic.

Optical injection-locking has been shown to reduce the linewidth of the laser [96]. A change in the linewidth will change the reflection-induced noise amplitudes. Without

experimental verification, it is unknown whether this change of linewidth will increase or decrease the received noise. However, this noise can be completely eliminated by using low-reflection connectors. Rayleigh scattering in fibers, which is due to the random material inhomogeneities in fibers, has been shown to contribute to an increase in detected noise [110]. The scattering strength is proportional to the laser coherence length; thus, a large linewidth laser is preferred. The injection-locked linewidth reduction may be undesirable in this case, if double-rayleigh scattering induced noise is dominant in the optical link.

4.6. Summary

To conclude, the relative intensity noise spectra of injection-locked VCSELs was studied. A large reduction of the RIN has been predicted and observed. A technique for measuring the noise of low power lasers was developed and applied for the injection-locking experiments.

Laser intensity noise was studied by using a model where Langevin shot noise terms are added to the rate equations. Numerical simulations with the differential equation solver were performed by adding a random variable, evaluated at each time interval.

The reduction in noise is attributed mainly to the increased resonance frequency with injection-locking, leaving a reduced noise at frequencies away from the resonance. Similar to the small-signal modulation response (S21), noise is enhanced near the resonance frequency due to photon-electron coupling in the rate equations.

It was found that increasing the injection ratio increased the resonance frequency, which decreased the noise. These trends agree very closely to the expressions derived for a free-running laser. Thus, in terms of noise, an optically injection-locked laser behaves very similar to a free-running laser but with an increased resonance frequency and hence a noise peak shifted to higher frequency.

Experiments showed preliminary results of RIN reduction. Full characterization of RIN, especially at low frequency, was difficult to achieve since the VCSEL power was too low. EDFA noise masked the improvement in low frequency noise. Further studies in RIN decrease are thus needed, with more meaningful results to be obtained by: using higher power lasers; by increasing the coupling of the VCSEL to the fiber; or by using a lower noise optical amplifier.

With the noise measurements performed, a record SFDR value at 2GHz was reported using the injection locking technique. Combining the noise reduction with nonlinear distortion reduction allowed for a greater increase in the dynamic range.

Chapter 5 Laser Distortions

In this chapter, we study the laser distortions for high modulation frequencies for injection-locked directly modulated lasers, and compare with free-running laser results.

In the first section, background information on understanding laser non-linearities and their impact on multi-channel transmission is presented. We discuss the distortion induced noise term in the CNR definition. Transmitter distortion is introduced by considering a two channel system with intermodulation distortion, followed by a consideration for multi-channel systems.

5.1. Multi-channel distortion noise

In a multi-channel system, transmitter distortion results in signal cross-talk, whereby part of the signal power is transferred from one channel to another. The net result is that the signal to noise ratio is decreased.

The following simulation example demonstrates the effect of distortion on a directly modulated semiconductor laser. The laser is biased at 5 mA, modulated by N=11 channels at a center frequency of 250 MHz, with a modulation index of m ~ 0.02. The laser threshold is 4 mA. The signal applied to the laser is:

$$i(t) = I_{bias}\left(1 + \sum_{n=1}^{N} m_n s_n(t)\cos(w_n t + f_n)\right) \tag{5.1}$$

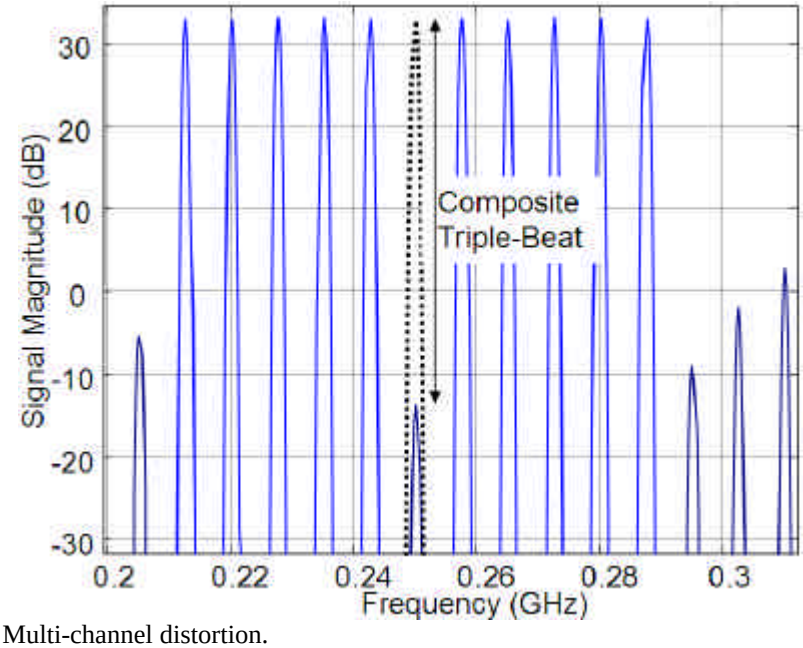

Figure 69 – Multi-channel distortion.
The composite triple-beat (CTB) is defined for each channel, and is the difference of the signal power and the distortion noise present at that frequency when the signal is turned off. In this case, the CTB = –14 dB – 32.8 dB = –46.8 dB.
(Simulation results were performed by Michael Moewe and Daniel Ceperley for the EE233 course)

Figure 69 shows the frequency spectrum of the laser output. When channel #6 is turned off, one still observes the presence of a signal. This signal is actually the distortion originating from the other 10 channels. The signal-to-noise ratio, or composite-triple-beat (CTB) is defined as the difference of the signal power and the distortion noise present at that frequency when the signal is turned off. In this example, the CTB = –14 dB – 32.8 dB = –46.8 dB.

Ideally, one would characterize a link by inputting many channels and measuring the CTB. However, in practice, device characterization is more often performed one or two channels. The distortion measurement in that case can be related to provide an estimate of the CTB.

5.1.1. Spur Free Dynamic Range

Direct modulation of semiconductor lasers for analog transmission has been a subject of active research for many years. In studying non-linearities, one of the most important figures-of-merit is the spur free dynamic range (SFDR). It is defined as dynamic range at the modulation power when the system noise floor equals the distortion noise [58]. The modulation power can be described either by the RF input power into the laser (or optical modulator) or by the modulation index (m). The RF input power will be used in this chapter. Dynamic range refers to the different between the signal and the noise terms (including distortion)

The distortion noise can originate from several sources: 2nd and 3rd harmonics of the signals, intermodulation distortion, and laser threshold clipping. For a two-tone

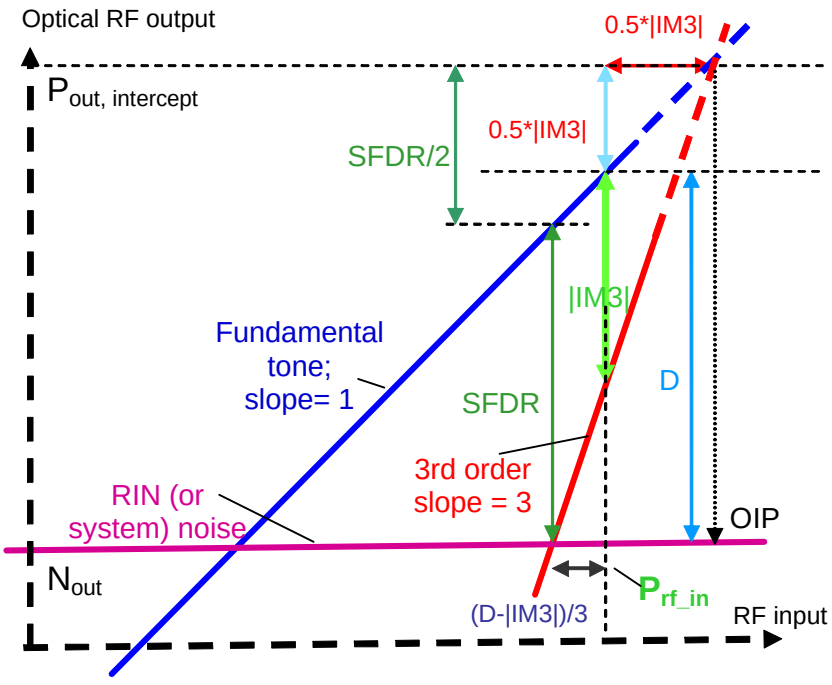

Figure 70 – Spur-free dynamic range determination
The fundamental tone power, distortion power, and noise vs RF input power determine SFDR.

analog modulated laser, SFDR is defined as the power difference between the signal and the system noise floor, at the point when the 3rd order intermodulation distortion (IMD3) power equals the system noise floor. Thus, SFDR is the dynamic range of the system when operated at the optimal input power level.

Shown in Figure 70 is a plot of RF output power for the signal, distortion, and noise, versus RF input power. The signal power, or fundamental tone, varies with a slope of 1, for low enough power. For higher input power exceeding the laser's maximum response, the output saturates, and the curve exhibits a roll-off. The third order distortion terms (either intermodulation distortion or 3rd harmonic distortion) vary with a slope of 3. The noise floor used in the figure can either be the laser RIN limited value, or the total link noise, including receiver thermal noise. In [111], the authors measure the total system noise, which is dominated by laser noise for low biasing current, and dominated by shot noise for high biasing current. For system experiments, an understanding of the total noise is crucial. However, for device characterization, understanding the device induced noise contributions (RIN and shot noise) is more beneficial since it allows for the prediction of the best possible link performance.

The relationship between the intermodulation distortion power, relative to the signal (IM3) and the spur-free dynamic range (SFDR) of the laser can be calculated with the help of Figure 70, and is as the following:

$$SFDR = \frac{IM3 + 2D}{3} \qquad (5.2)$$
$$where\ D = 20\log(m) - RIN(dB/Hz)$$

where m is the optical modulation index of the laser.

The SFDR can also be defined as [112]:

$$SFDR = \left(\frac{P_{\text{out,intercept}}}{N_{\text{out}}} \right)^{\frac{2}{3}} \qquad (5.3)$$

Previous Experimental Results

Distortion is typically measured on single-tone 2nd and 3rd order harmonics, as well as two-tone intermodulation products (IMD3). The distortion physically originates from the nonlinear characteristics of the laser, including nonlinearity of the light-current (LI) curve, the carrier-photon interaction or from spatial hole-burning [56, 57]. SFDR is a strong function of frequency, and has its lowest value at frequencies near the relaxation oscillation frequency. Thus, lasers are typically analog modulated at frequencies well below this frequency.

The highest reported IMD3 SFDR for a 1.3 um distributed feedback (DFB) laser is 100 dB-Hz$^{2/3}$ for frequencies below 1 GHz [59]. An 850 nm vertical cavity surface emitting laser (VCSEL) has achieved an IMD3 SFDR of 113 dB-Hz$^{2/3}$ [61] at 0.9 GHz. The highest 1.55 um VCSEL SFDR for 3rd order harmonic distortion (3f-SFDR) is only 81 dB-Hz$^{2/3}$ at 1 GHz [62].

Injection locking of semiconductor lasers has been actively investigated recently [20, 99]. It has been predicted theoretically that, when injection locked to a master laser, the follower laser's performance could be improved with a larger bandwidth, reduced chirp, and reduced distortion.

Theoretical work predicts that injection locking can increase the laser's relaxation oscillation frequency (f_r) and reduce the laser nonlinear distortion [100]. Experiments have demonstrated such improvements: a 1.5 μm DFB laser was locked to another DFB laser, and a 5 dB-$Hz^{2/3}$ improvement in IMD3 SFDR was reported, owing to a 15 dB-$Hz^{2/3}$ reduction in IMD3 power. In that experiment, the injection locked DFB had a 100 dB-$Hz^{2/3}$ SFDR at 2.0 GHz [18]. The 3rd harmonic distortion SFDR exhibited a similar trend with frequency as the IMD3 SFDR.

5.1.2. External Modulator Distortion

Transmitter distortion is introduced by considering a two channel system with intermodulation distortion, followed by a consideration for multi-channel systems. Distortion for the case of external modulation is considered first, as it is easiest to understand.

Origin of Intermodulation Distortion

Any component in a link that is not perfectly linear will introduce distortion. The impact of this distortion can by understood by considering a Mach-Zehnder modulator with a sinusoidal transfer function with a two-tone modulation. The input voltage to the modulator is *v(t)*, with a modulation index *m*, and the output signal is *p(t)*:

$$v(t) = m\sin(w_1 t) + m\sin(w_2 t) \tag{5.4}$$

$$p(v(t)) = \sin\{v(t)\} \tag{5.5}$$

The output signal can be expanded as a Taylor series to the third order, and expanded by using trigonometric identities:

$$\begin{aligned} p(v(t)) &\approx v(t) - \frac{1}{6}v(t)^3 \\ &= m\sin(w_1 t) + m\sin(w_2 t) - \frac{1}{6}\left\{m\sin(w_1 t) + m\sin(w_2 t)\right\}^3 \\ &= \left(m - \frac{3}{8}m^3\right)\left[\sin(w_1 t) + \sin(w_2 t)\right] \\ &+ \frac{1}{8}m^3\left[\sin(w_1 t - 2w_2 t) - \sin(2w_1 t - w_2 t)\right] \\ &+ \frac{1}{8}m^3\left[\sin(w_1 t + 2w_2 t) + \sin(2w_1 t + w_2 t) + \frac{1}{3}\left\{\sin(3w_1 t) + \sin(3w_2 t)\right\}\right] \end{aligned} \tag{5.6}$$

We see that the output consists of the two original sinusoidal signals at frequencies ω_1 and ω_2, with the addition of distortion terms being the third harmonics at frequencies $3\omega_1$, $3\omega_2$, $2\omega_1+\omega_2$, and $\omega_1+2\omega_2$, as well as intermodulation terms at frequencies $2\omega_2-\omega_1$, and $2\omega_1-\omega_2$. The frequency content of the output signal is shown in Figure 71.

The distortion term powers are usually described relative to the fundamental tones. For this sinusoidal transfer function, we find that the intermodulation power relative to carrier (IMD3/C) is $\sim\frac{1}{8}m^2$. For a modulation index of m=0.02, we find that IMD3/C in

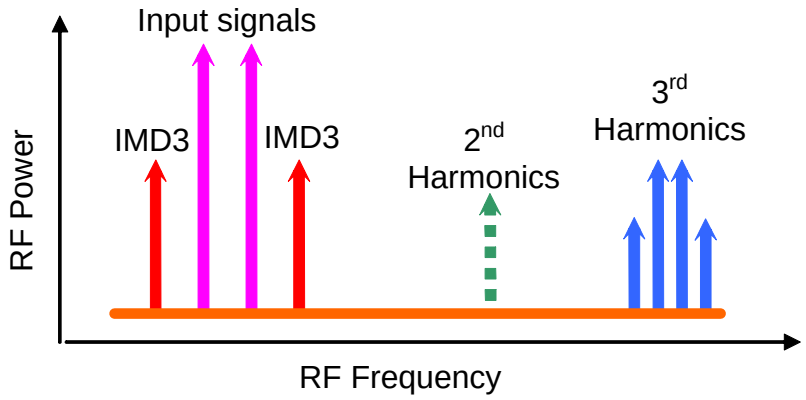

Figure 71 - Frequency generation due to distortion from a nonlinear transfer function.
Input signals at ω_1 and ω_2; IMD3: intermodulation distortion products at $2\omega_2-\omega_1$, and $2\omega_1-\omega_2$; 2nd harmonics at $2\omega_2$ and $2\omega_1$ but not present in the symmetric sinusoidal transfer function; 3rd harmonics at $3\omega_1$, $3\omega_2$, $2\omega_1+\omega_2$, and $\omega_1+2\omega_2$.

the optical domain is 43 dB, meaning that when the signal is optically detected (square-law detector), the intermodulation distortion is 86 dB lower than the signal. The single-tone 3rd harmonics, at frequencies $3\omega_1$ and $3\omega_2$ have relative powers of 3H/C of $\sim \frac{1}{24} m^2$, and are 9.5 dB lower than the intermodulation terms. This relationship between intermodulation distortion and 3rd harmonic power is true only for the case of a frequency independent response, as was assumed in (5.5). In general, for example with semiconductor lasers, the distortion types will not have a simple relationship; this is explored in a later section.

This analysis can be carried out for three-tone modulation, with triple beat frequencies $\omega_1\pm\omega_2\pm\omega_3$. It is found that the distortion powers for those terms will be $\sim \frac{1}{4} m^2$, that is 6 dB (electrical) higher than the $2\omega_1\pm\omega_2$ intermodulation terms.

As described in the next section, the distortion becomes problematic in a multi-channel system if the distortion terms overlap with other channels.

Multi-channel Distortion

The situation is more complicated to analyze when there are more than two channels to be transmitted with the transmitter. Because of the beating between the signals from multiple channels, distortion will increase the $\sigma_{Distortion}$ term in the carrier-to-noise equation and thereby reduce the dynamic range of the system. The most important distortion term will be the composite triple beat (CTB) that originates when the $f_1\pm f_2\pm f_3$ frequencies fall on other carrier frequencies. This type of distortion is most significant in systems that lie in a frequency range that is less than one octave (i.e. the 2nd harmonics lie outside the communication band). In a broadband system with many carriers, the distortion adds up quickly with an increasing number of channels.

For N equally spaced carriers, the total number of distortion terms of the $f_1\pm f_2\pm f_3$ type (CTB) present at the M^{th} channel is estimated to be [113]:

$$\text{Number of beats} = \frac{(\text{N-1})^2}{4} + \frac{(N-M)(M-1)}{2} - \frac{N}{2} \tag{5.7}$$

This can be approximated to be:

$$\begin{aligned} \text{Number of beats (mid band)} &= \frac{3N^2}{8} \\ \text{Number of beats (band edge)} &= \frac{N^2}{4} \end{aligned} \tag{5.8}$$

Assuming that the carriers are not phased-locked, the distortion power will add. Since we know that the intermodulation distortion terms are 6 dB lower than the triple beat powers, the composite triple beat can thus be found. The approximate formula for relating CTB and IMD3 has been determined to be [114]:

$$\begin{aligned} CTB(dBc)bandedge &= IMD3(dBc) + 10\log\left(3N^2/8\right) + 6 \\ CTB(dBc)midband &= IMD3(dBc) + 10\log\left(N^2/4\right) + 6 \end{aligned} \tag{5.9}$$

Cable television (CATV) signals are presently commonly distributed using optical subcarrier multiplexing, with the signals using a band between 50 and 550 MHz for 42 channels. The requirements on the linearity of the transmitter are a composite-triple-beat (CTB) of better than -65 dBc and a carrier-to-noise (CNR) ratio of >55 dB [115]. For a 42 channel system, using equation (5.9), these requirements lead to a minimum of -99 dBc intermodulation distortion. Additionally, -75 dBc is required for composite second-order distortion.

Clipping Distortion

Distortion at the transmitter can occur due to the clipping of the signal [116-119]. In directly modulated semiconductor lasers, the source of clipping is the threshold of the laser. For external modulators, the clipping can be symmetric for both too high and too low signals. For a signal with a Gaussian probability distribution (PDF) with a mean μ, the probability density function for the normalized signal $i(t)/I_{bias}$ is:

$$p(x) = \frac{1}{\sqrt{2p}\,m} e^{-\frac{x^2}{2m^2}} \tag{5.10}$$

As shown in Figure 72, if the signal amplitude is too large, the signal will be clipped due to the laser threshold. This distortion can be understood as a white noise source, approximated by impulses for each time the signal is clipped.

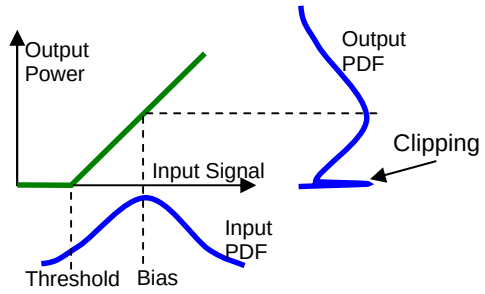

Figure 72 – Distortion due to laser threshold clipping.

This source of distortion has been modeled and experimentally verified. The Carrier to nonlinear distortion ratio (CNLD) is given by the modified Saleh model, given by Darcie [117]:

$$CNLD = \sqrt{2p}\left(1+6m^2\right)m^{-3}e^{\frac{1}{2}m^2} \tag{5.11}$$

In CATV directly modulated laser links [120], laser linearity can be made low enough such that clipping is the fundamental limit. The clipping distortion sets a limit on the maximum allowed effective modulation index. For a CNLD of < 60 dB, the modulation index must be less than 0.26 [51]. This places limits on the total number of channels that can be transmitted in a given link.

5.1.3. Semiconductor Laser Distortion

In multi-channel signal transmission applications, the signal contains a many high-frequency carriers. In the presence of transmitter non-linearity, distortions will interfere with signal transmission. The highest impact originates in the intermodulation distortions, with certain systems exhibiting susceptibility to second and third order harmonics.

Semiconductor lasers, modulated at low frequencies, exhibit signal distortions due to the non-linearity of the light output-current curve. For lasers with very linear LI curves, very low distortions have been observed at low frequency [121]. However, for high frequency modulation (GHz), distortions increase significantly, and originate from the nonlinear rate equations.

Intermodulation distortion in directly modulated lasers has been studied experimentally and theoretically [78], using a linearization of the rate equations. Simulations indicate that second harmonics increase as the square of the modulation index, while intermodulation distortion products (IMD3) and third harmonics increase as the cube of modulation index. For frequencies below the resonance frequency, the amplitude of the IMD3 relative to the signal amplitude (IMD3/C) increases at a rate of 40 dB/decade as frequency increases. Typically, the distortion is largest at the resonance frequency, and for some laser parameters, a peak at half the resonance frequency is observed. This distortion originates in the laser rate equations.

The origin of nonlinear distortion can be the non-ideality of the LI curve, carrier leakage, spatial hole burning and the nonlinear interaction between photons and carriers inside the laser cavity. When the laser is operated in multi-GHz range, it is the latter that dominates the nonlinear distortion. The distortion is especially prominent when the modulation frequency is in the proximity of the relaxation oscillation peak.

For free-running lasers, harmonic distortion analyses have been conducted, by linearizing the rate-equations and solving for the distortion terms [78], originating from the nonlinear interaction between photons and carriers. This work was extended to provide a formula for the intermodulation distortion [122]:

$$\frac{IMD}{C} = \frac{1}{2} m^2 \frac{\left[\left\{ \left(\frac{f}{f_r} \right)^4 - \frac{1}{2} \left(\frac{f}{f_r} \right)^2 \right\}^2 + \left(\frac{f}{f_r} \right)^6 \left\{ 2p \, f_r t_p \right\}^2 \right]^{1/2}}{g(f) g(2f)} \tag{1.12}$$

$$where \; g(f) = \left[\left\{ \left(\frac{f}{f_r} \right)^2 - 1 \right\}^2 + \left\{ \frac{2pe \, f}{g_0} \right\}^2 \right]^{1/2}$$

A reduction in the IMD3 power will improve the SFDR, evident in equation (5.2). A 10 dB reduction in IMD3 will shift the optimal input power point (to higher power) by 10 / 3 dB = 3.3 dB. Thus, SFDR will be increased by 3.3 dB for a 10 dB reduction in IMD3.

An inspection of the IMD3 free-running laser formula shows that a higher laser relaxation oscillation frequency will lead to a lower distortion at a given frequency. Because injection-locking of lasers can lead to an increased resonance frequency, the IMD3 formula suggests that injection-locking could reduce the distortion and SFDR.

Indeed, this is the case and has been shown theoretically by a performing a linear analysis on the injection-locked rate equations [79]. As shown in Figure 73, the distortion peaks at the resonance frequency, which is increased with injection-locking. Additionally, the distortion power is reduced at low frequencies for certain locking conditions. This has also been verified experimentally [18].

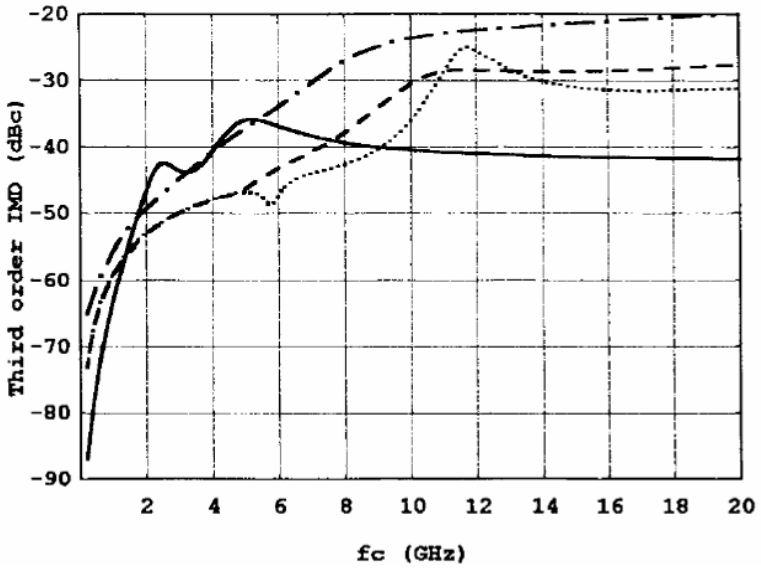

Figure 73 – Simulated intermodulation-distortion for various frequency detuning [79]

Distortion in semiconductor lasers with optical feedback has been studied experimentally and theoretically. For low feedback levels (between -70 and -40 dB), the distortions increase with increasing feedback. Thus, low reflections are generally desirable for low-distortion communications [123]. Although not pointed out by the authors, for higher levels of feedback, -30 to -20 dB, it was observed experimentally that feedback can in fact reduce the distortion levels. This is similar to the situation of injection locking, except that 1) the feedback occurs at zero detuning, 2) the feedback path length plays a role in determining the stability of the system.

5.2. Injection-Locking Distortion Numerical Simulations

Numerical simulations were performed using the injection-locked rate equations. In Figure 74, the small signal frequency response for both free-running and injection-locked lasers is shown. For each frequency, intermodulation distortion powers are also plotted. The results were obtained by modulating the laser with two tones, separated by 200 MHz. The simulation is conducted for 160 ns, and the time signal is Fourier transformed and the spectral components are analyzed.

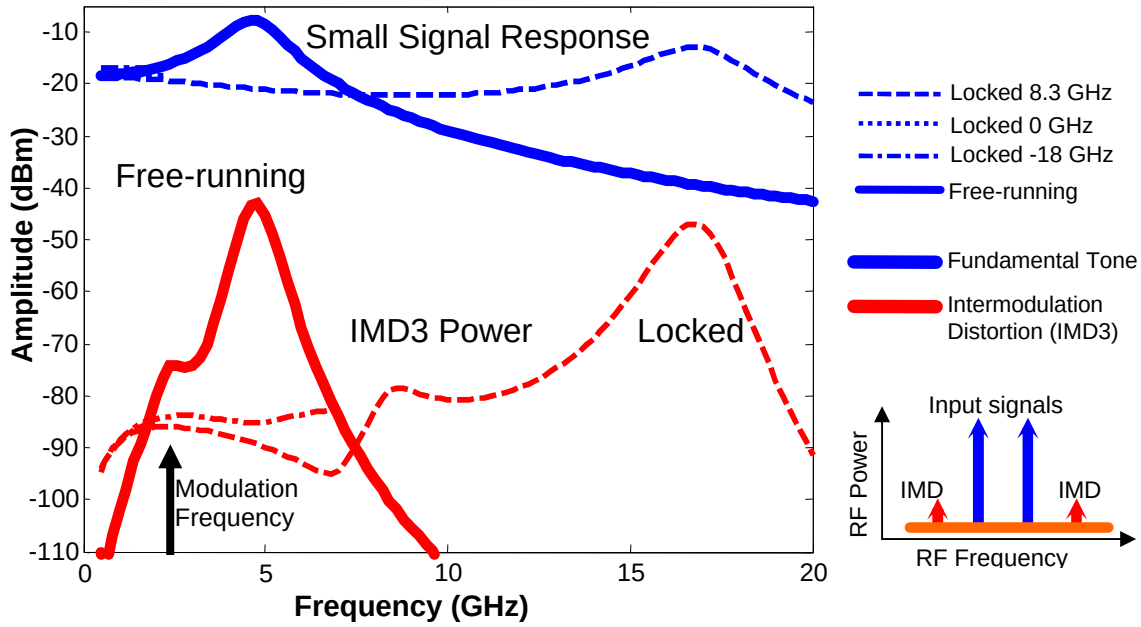

Figure 74 - Numerical simulations of intermodulation distortion vs frequency

As seen in the figure, the distortion is highest near the relaxation oscillation frequency. At ½ the relaxation frequency, a second peak appears. This peak appears because signals at that frequency have a second order distortion term that is equal to the resonance frequency, thus sees a high amplitude and distortion.

For the injection-locked cases, it is seen that the peak in the distortion occurs at the new relaxation oscillation frequency. For the -8.3 GHz case, the resonance peak is now at ~17 GHz. Since the distortion peak has been moved to a higher frequency, the distortion is significantly reduced for frequencies near the free-running resonance frequency (~5 GHz). Thus, a broadband IMD3 reduction is observed for frequencies ranging from ~2 to ~7 GHz. For low frequencies, however, the injection-locked distortion is much higher than the free-running laser case. In particular, the free-running laser follows a 40 dB/decade decrease in IMD3 with decreasing frequency, whereas the injection-locked IMD3 appears to not decrease as quickly.

Figure 75 shows the simulations for the second and third order distortion terms. Similar to the IMD3 terms, the 2nd and 3rd order distortion for the free-running case show that the highest distortion occurs at the resonance frequency, with smaller peaks at half the resonance frequency, as well as at one third the resonance frequency.

It is observed that the 3rd harmonic is similar to the IMD3, with the peak amplitude differing by ~10 dB for the two cases. This can be understood by considering a device

with a uniform frequency response H(ω). An analytic analysis has shown that for Mach-Zehnder modulators, with a sinusoidal transfer function, the distortion terms are given by [124], with the IMD3 being 10 dB higher:

$$D_{3rd\ harmonic} = 20\log\left(\frac{m^2p^2}{96-9m^2p^2}\right),\ D_{IMD3} = 20\log\left(\frac{m^2p^2}{32-3m^2p^2}\right) \tag{5.13}$$

In the case of a directly modulated laser, the situation is more complicated since there is a frequency dependence to the amplitude response. Thus, it is expected that in general, the 3rd harmonic power is different from the IMD3 power. Further comparison of the analog transmission performance differences between direct and external analog modulation is described in [125].

For the injection-locked traces, again, regions of high distortion are observed at the injection-locked resonance frequency, at a half and at one third the frequency. There is a broad frequency band, 1 to ~7 GHz, where the 2nd and 3rd harmonic distortion powers are reduced with injection, compared to the free-running powers.

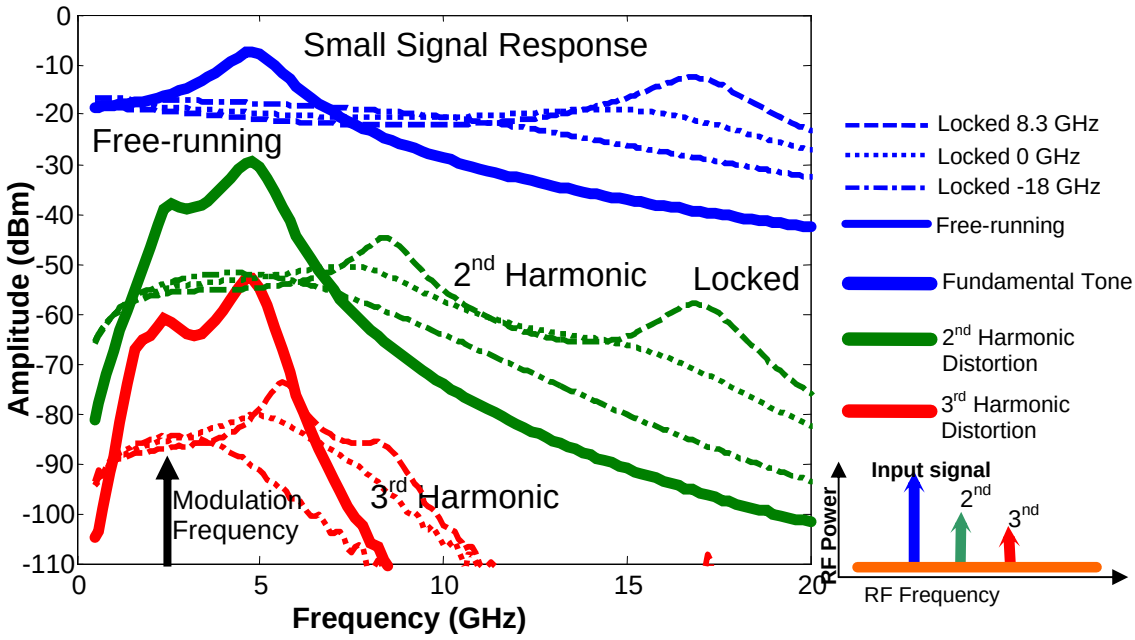

Figure 75 - Numerical simulations of 2nd and 3rd harmonic distortion vs frequency

Spur-free dynamic range measurements are performed using the same parameters as the above simulations. The injection condition is -18 GHz detuning for a 0.001 injection ratio. Figure 76 shows both the free-running and the injection-locked IMD3 powers at 2.0 GHz, showing that the IMD3 power is reduced by 10 dB while the noise is reduced by 15 dB. This results in an increase in the SFDR by 12 dB/Hz$^{2/3}$.

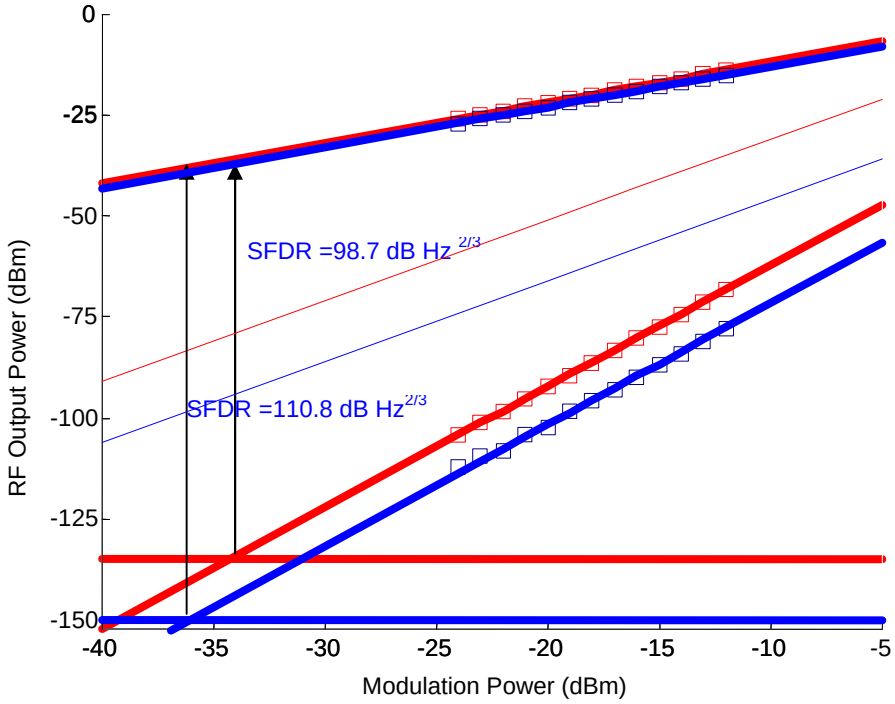

Figure 76 - Numerical simulations for the Spur-Free Dynamic Range.

5.3. Experiments - 3rd Harmonic Distortion

Injection locking is experimentally demonstrated to enhance the analog modulation performance of 1.55 μm VCSELs. A detailed study of injection locking over a range of detuning and injection power is performed. For all detuning conditions, analog distortion measurements are performed, by observing the 3rd harmonic generation. A ~20 dB-Hz$^{2/3}$ improvement in 3rd harmonic dynamic range was achieved at 1.0 GHz. The improvement in dynamic range is observed over a large range of wavelength detuning and injection power.

5.3.1. Experiment

The experimental setup is shown in Figure 77. A tunable, directly modulated 1.55 um VCSELs [7] was used as the follower laser. In this experiment a DFB laser was used as the master laser. A circulator (with angle-polished connectors) was used to couple the master laser into the follower VCSEL. Two lenses in a confocal arrangement (f = 3 mm, 5 mm) on micro-positioning stages were used to couple light between the circulator FC/APC connector and the TO-48 packaged VCSEL. The modulated VCSEL signal from the third port of the circulator was coupled into a high-speed (10 GHz) analog photo-detector, followed by a 20 GHz low-noise RF amplifier. An RF spectrum analyzer was used for the harmonic distortion studies. Each data point taken using the spectrum analyzer was averaged for approximately 1 minute because large power fluctuations (~10 dB) were observed for the 3rd harmonics. The optical spectrum at the output of the circulator was monitored to ensure the injection locking condition was obtained.

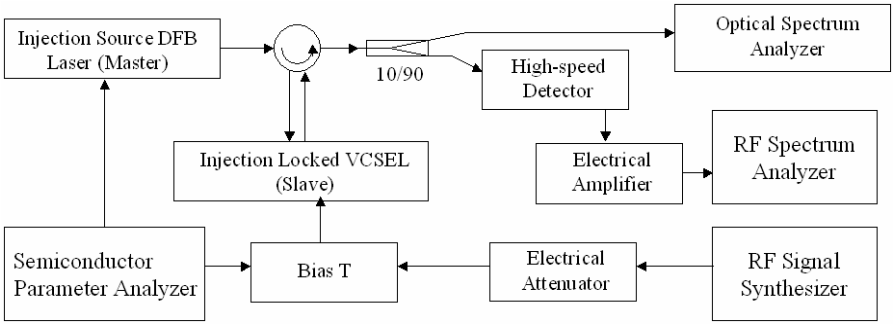

Figure 77 – System Diagram

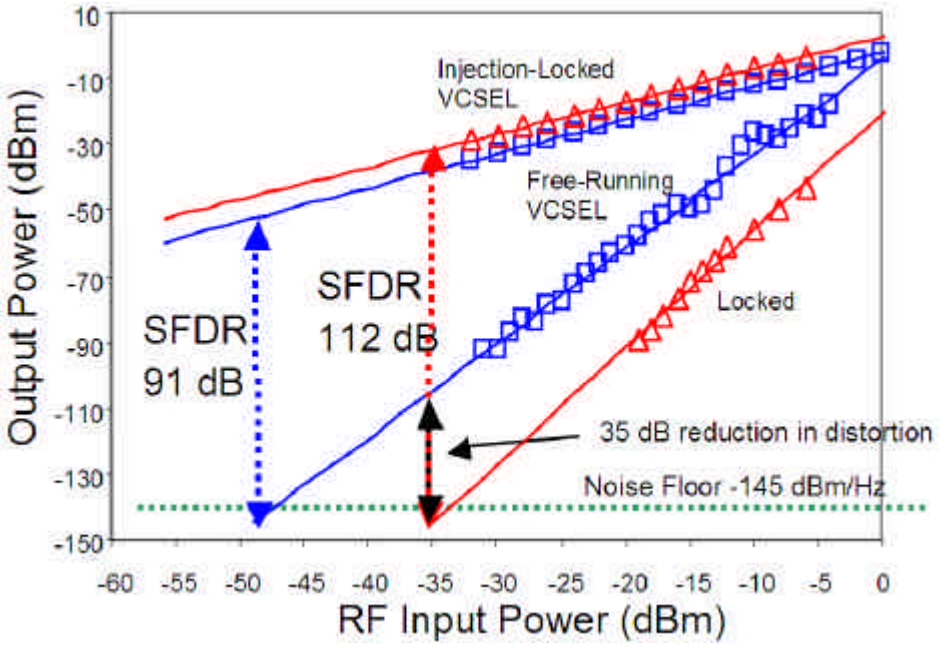

Figure 78 – Single-tone 1 GHz 3f-SFDR for the 1538.4 nm VCSEL.

More than ten VCSELs were characterized in this setup and all showed SFDR improvements with injection locking. In this experiment, the VCSEL was biased at 4.0 mA, resulting in a light output of approximately half of the peak power (~50 μW fiber coupled power). This bias was chosen to maximize the useful linear range of the VCSEL. The VCSEL was electrostatically tuned [126] to approximately match the DFB wavelength.

The DFB optical output power was first adjusted by varying the DC bias (from 10 mA to 100 mA). To achieve the locking conditions, the wavelength detuning was varied by adjusting the DFB temperature while monitoring the optical spectrum on the optical spectrum analyzer. In the following, detuning is defined as master laser wavelength minus the free-running follower laser wavelength.

Figure 78 show shows fundamental and 3rd harmonic power vs. RF input power for the 1538.4 nm VCSEL. The follower VCSEL was modulated by a single-tone carrier at 1 GHz. The incident DFB power was ~ -4 dBm (strong injection locking regime) and the detuning was +0.24 nm.

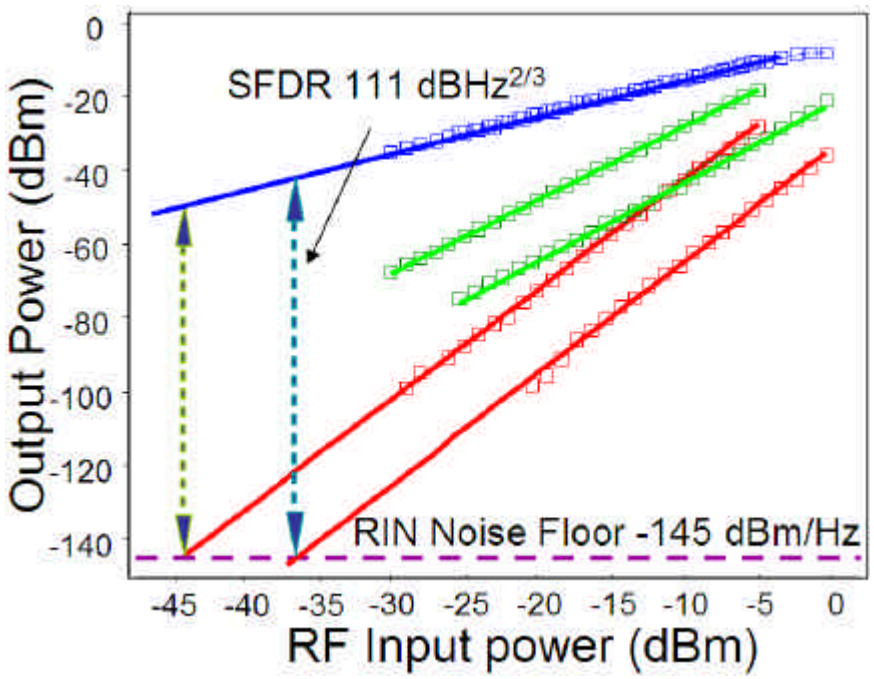

Figure 79 – Single-tone 2 GHz 3f-SFDR for the 1538.4 nm VCSEL
The injected power is -7 dBm with a detuning of 0.2 nm, 3.1 mA VCSEL bias, device FAR146

A 5dB enhancement of the fundamental tone power and a 35dB reduction in the 3rd harmonic distortion power were obtained with injection locking. The change in fundamental tone is due to injection dynamics and can be an increase or decrease depending on detuning values. The 3f-SFDR is determined to be 91dB-Hz$^{2/3}$ and 112dB-Hz$^{2/3}$ for the free-running and injection locked cases, respectively. This was determined by fitting a line to the fundamental and 3rd harmonic data. The slopes of the free-running and injection locked 3rd harmonic lines were 2.9 and 3.6 respectively, which deviate from the theoretical value of 3.0. Fitting using a slope of 3 yields 3f-SFDR values of ~90dB-Hz$^{2/3}$ and 108dB-Hz$^{2/3}$. The fundamental tone slopes were 1.0, as expected. The noise floor of –145dBm/Hz was based on the separately measured VCSEL RIN.

Figure 79 shows a similar measured but performed at 2.0 GHz. In this case, the free-running SFDR is 96 dB-Hz$^{2/3}$, and is improved to 111 dB-Hz$^{2/3}$ with injection. This represents a 15 dB-Hz$^{2/3}$ improvement in 3rd harmonic SFDR. The enhancement is due to a 4.5 dB increase in the modulation efficiency and a 22 dB reduction in 3rd harmonic relative to carrier. The results were shifted in the x-axis so that the fundamental tones co-incide, thus the modulation efficiency enhancement is not visible on this plot. The 2nd harmonic dynamic range is also improved by 18 dB-Hz$^{1/2}$.

SFDR Measured over the locking range

The following experimental results show the effect of wavelength detuning and input power on the locking stability and analog improvement. The injection power and detuning of the master DFB laser were adjusted and analog measurements were performed for a fixed VCSEL RF input power of –8 dBm at 1.0 GHz. 10 different injection powers were chosen, and for each, the detuning was varied 5-20 values, providing ~100 data points per plot. Surface plots were generated by interpolation.

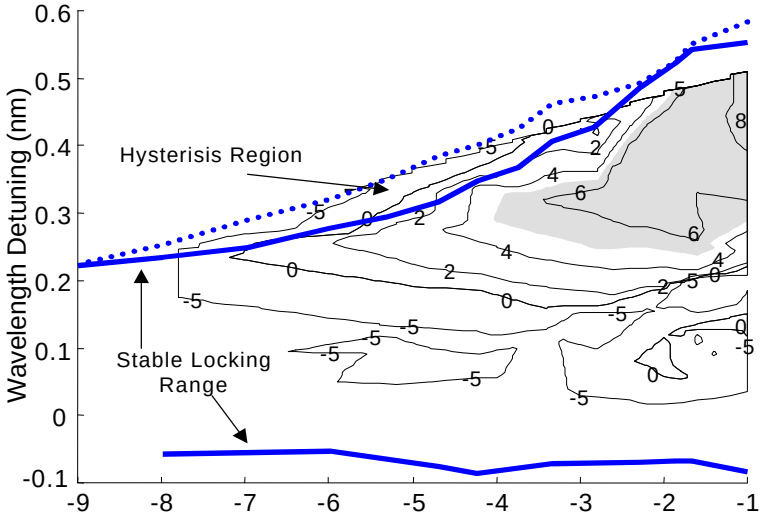

Figure 80 – Stability plot showing modulation efficiency enhancement
The wavelength detuning and injection power are varied, and the contour lines refer to the 1.0 GHz fundamental tone power increase (free-running vs. injection-locked). The shaded area are conditions where increase >5dB. The data is plotted over the injection locking range, for the 1538.4 nm VCSEL.

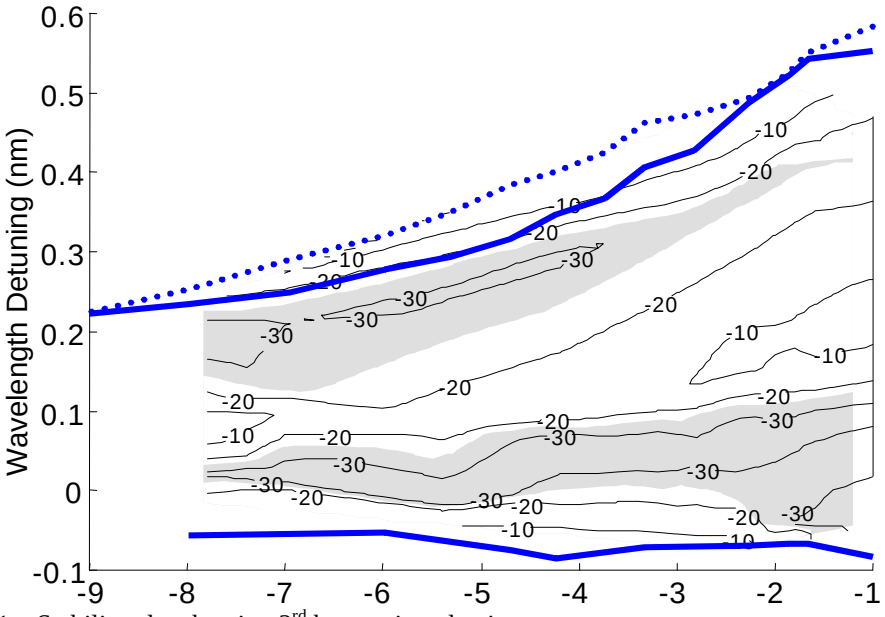

Figure 81 – Stability plot showing 3rd harmonic reduction
The wavelength detuning and injection power are varied, and the contour lines refer to the 3rd harmonic reduction (free-running vs. injection-locked). The shaded area are conditions where the reduction > 25 dB. The data is plotted over the injection locking range, for the 1538.4 nm VCSEL.

Using the distortion powers, estimates of dynamic range are given.

In all three plots, the region between the thick lines corresponds to stable locking range. The region at the top of the plots, between the dotted and upper thick curve, corresponds to a hysteresis region, where stable locking is achieved only by first locking the follower, then increasing detuning to longer the wavelength. For low injection powers, stable locking can be made for a small detuning range; e.g. at –9 dBm injection

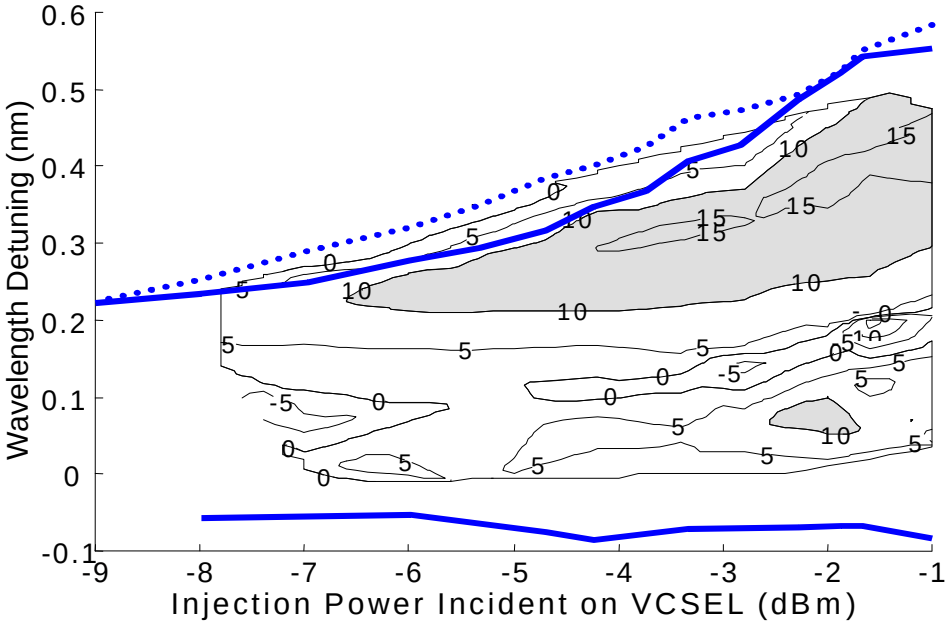

Figure 82 – Stability plot showing estimated 3f-SFDR improvement
The wavelength detuning and injection power are varied, and the contour lines refer to the estimated 3f-SFDR improvement (free-running vs. injection-locked). The shaded area are conditions where the improvement > 10 dB. The data is plotted over the locking range, for the 1538.4 nm VCSEL.

power, detuning needs to be 0~0.2 nm. However, for high injection powers at –1dBm, a larger detuning range of 0~0.6nm is observed. In our experiments, injection locking is typically easily achieved.

Figure 80 shows the increase in the fundamental tone power of the injection locked VCSEL as compared to the free-running case. Improvements as high as 8 dB were observed, with the greatest improvement for high optical injection power. It is possible that even higher injection powers would further increase the RF fundamental tone power.

Figure 81 shows the reduction in 3rd harmonic distortion, again compared to the free-running VCSEL. The highest reduction observed in the vicinity of the fundamental tone power increase peak was 40 dB, and had a maximum value within our measurement range, at roughly –5 dBm injection power. It appears that higher optical injection powers reduce the improvement harmonic distortion. The highest fundamental tone increase and the greatest 3rd harmonic reduction do not occur at the same injection condition (different detuning and injection power values), hence the maximum 3f-SFDR will occur at a point between the two respective maxima.

Based on the extrapolated data, we can estimate the 3f-SFDR improvement assuming a 3rd harmonic slope of 3.0, a fundamental slope of 1.0, and a noise floor of –120 dBm/Hz. The SFDR improvement over the locking range is shown in Figure 82. The greatest estimated 3f-SFDR improvement at this RF input power was 17 dB. The actual 3f-SFDR improvement value is sensitive to the slope of the line. This explains why we actually observed a ~20dB-Hz$^{2/3}$ improvement in Figure 78.

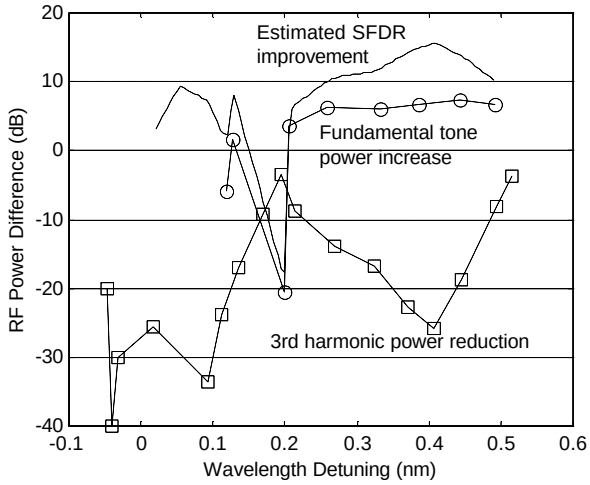

Figure 83 – Change in 3f-SFDR versus detuning.
An SFDR improvement is observed between 0.2 and 0.5 nm detuning, for a –2 dBm optical injected power.

In Figure 83, data from Figure 82 is re-plotted for a single optical injection power of –2 dBm. The bottom curve corresponds to the 3rd harmonic distortion reduction, the center is the fundamental tone power increase, and the top is the estimated 3rd harmonic SFDR improvement. As can be seen, a >10 dB improvement in 3f-SFDR occurs for a wavelength detuning range of 0.25 nm to 0.5 nm. This demonstrates that DFB-VCSEL locking is insensitive to wavelength detuning, and an improvement in analog performance can be readily achieved. A peculiar "W" pattern is observed for the 3rd harmonic reduction, showing two minima. Reductions as great as 50 dB were observed for the first minima, but do not coincide with a large improvement in fundamental tone. We understand that the improvement in fundamental tone power is most important to increasing 3f-SFDR (1 dB fundamental tone increase = 1 dB 3f-SFDR increase), while the 3rd harmonic reduction provides a lesser improvement (1 dB reduction = 1/3 dB 3f-SFDR increase) due to the slope of 3 in the 3f-SFDR plot.

As discussed in theory section, non-linear distortion is reduced because injection locking increases the resonance frequency. A larger offset between the modulation and resonance frequencies reduces the carrier-photon interaction, which in turn reduces the 3rd harmonic distortion. Although we observed an enhancement in the fundamental power, it was not predicted in any publications and the physical origin is still unknown.

5.3.2. Two-Tone Distortion Measurements

Although more difficult to perform, two-tone distortion measurements are preferred over single-tone ones. The difficulty arises from the necessity of maintaining an identical power for both modulation signals, for all input power conditions. Additionally, the two modulation sources must be isolated sufficiency so that the measurements are not limited by the intermodulation distortion of the instrument.

Two-tone modulation experiments are preferred, especially for directly modulated lasers, since they can be related to composite-triple-beat values. 3rd harmonic

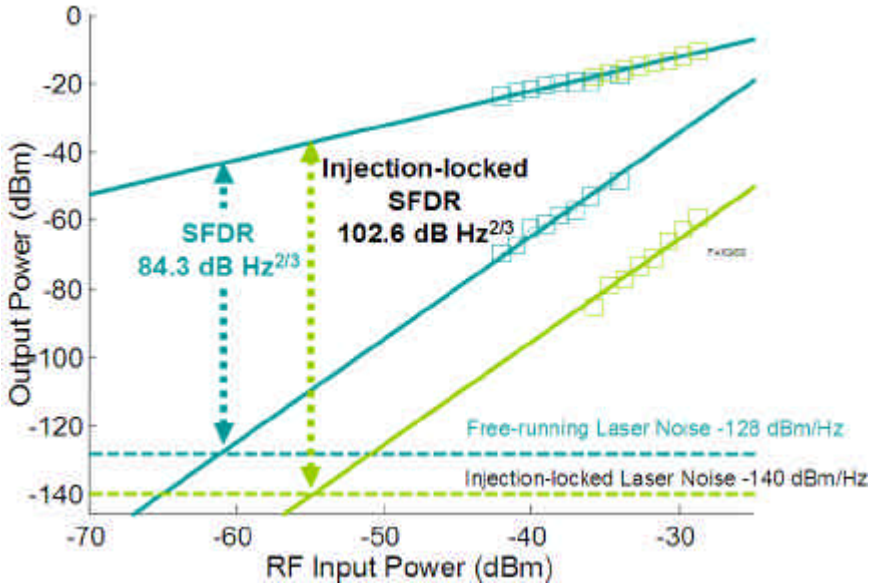

Figure 84 – Two-tone experimental SFDR, at 2 GHz.

measurements do not have a simple relationship to CTB, except for the case of external modulation where the frequency response is flat.

Two-tone measurements were performed on a different device, FAK968. This device did not exhibit the modulation efficiency enhancement that was observed in several other devices. Measurements were performed at 2.0 GHz, with a tone spacing of 100 MHz. The results are shown in Figure 84.

5.3.3. Conclusion

We demonstrate that injection locking improves the analog performance of 1.55 um VCSELs. We show that injection locking can improve the modulation bandwidth by a factor of two and reduce modulation non-linearities. The 3rd harmonic SFDR was improved by ~20dB-Hz$^{2/3}$ to be 112 dB-Hz$^{2/3}$ at 1 GHz and 111 dB-Hz$^{2/3}$ at 2 GHz. This is the highest reported 3f-SFDR for a long-wavelength VCSEL. The dependence of locking on detuning and injection power was investigated. 3f-SFDR improvement is achieved over a reasonably large range of injection conditions.

5.4. Fiber Optic Link Induced Distortion

In analog fiber optic communication, the principle source of distortion originates in the transmitter. However, other distortions can be introduced in the fiber link. Fiber dispersion, in particular, can be a source of distortion.

5.4.1. Distortion from Fiber Dispersion

Optical modulators generally have some unwanted phase modulation, which is termed residual signal chirp. This chirp can lead to fiber induced distortion for long link length (100 km) for large modulation indexes [127]. Significant composite second order

(CSO) distortion was observed for lengths of 100 km [127]. As expected, the use of dispersion shifted fiber eliminates the observed distortion. The addition of composite triple beat (CTB) distortion due to fibers is understood to be minimal [128], but experimentally, it was seen that there is a quasi-coherent interaction between the fiber induced CTB and the transmitter CTB, leading to a large degradation in total CTB. Additionally, this CTB degradation was highly dependant on link length and transmitter modulation index.

The CSO distortion introduced by fiber dispersion has been theoretically modeled [129] and experimentally verified [130]. The analysis of the time delay introduced due to dispersion is shown to give rise to a distortion. The total distortion becomes the summation of the intrinsic laser distortion and the distortion due to the fiber. The dispersion induced CSO is proportional to distance, fiber dispersion, and laser chirp.

The distortion induced by fiber dispersion can be reduced to acceptable levels by several methods: limiting the transmission distance to several kilometers, using dispersion-shifted fiber (DSF), compensating the dispersion using dispersion-compensating fiber (DCF), by generating the analog signals using a low chirp source such as an external modulator [128, 130], or by using a single sideband signal [131].

Dispersion can be reduced by using a single sideband (SSB) optical signal, instead of the standard direct amplitude modulated double-sideband signal [131]. The generation of SSB signals is performed by modulating the two branches of a mach-zehnder modulator with signals phase shifted by pi/2. This results in cancellation of one of the side-bands in the optical signal. In ordinary direct modulation, a double-sideband (DSS) signal experiences dispersion in the fiber between the two side-bands. Thus, at the detector, the beating between the sidebands and the carrier tone can lead to a cancellation of the signal. In the SSB technique, since there is only one signal, no such problem exists. Thus, the transmission distance will not be limited by dispersion as in the DSS case.

Optical Injection Locking

Optical injection-locking has been shown to reduce the chirp of the laser [132, 133]. Since the dispersion induced CSO is proportional to laser chirp, injection-locking is predicted to reduce the CSO.

Single Sideband Transmitter

Optical injection-locking could be used to generate single-side band signals. Two injection-locked lasers, modulated at a pi/2 phase shift apart, could be optically combined, resulting in a cancellation of one of the optical side modes.

5.4.2. Distortion from Optical Amplifiers

Optical amplifiers can also introduce distortion, through the process of FM-AM conversion [134]. When the chirped modulated signal passed through the EDFA with wavelength dependent gain, it experiences undesired amplitude modulation converted from the frequency modulation superimposed upon its desired amplitude modulation. The 2^{nd} harmonic distortion will be greatest where the slope of the optical gain vs. wavelength is highest. Thus, gain-flattened optical amplifiers would reduce this

distortion source. The distortion is also proportional to the frequency chirping of the signal, thus a laser source with low chirp is desirable.

5.4.3. Reduction of Chirp due to Injection-Locking

Injection-locking of semiconductor lasers has been shown to reduce the chirp of the modulated signal. We have demonstrated this both experimentally and with simulation [135, 136]. Simulation results are shown in Figure 85. In the simulation, the injection-locked rate equations were current modulated with a 2.5 Gb/s digital signal. The frequency deviation was found by taking the derivative of the optical phase. In a free-running laser, it can be expressed as the following, where α is the linewidth enhancement factor, S is the photon number, g is the gain, and N is the carrier density:

$$n = \frac{a}{4p}\left(\frac{1}{S}\frac{dS}{dt} + e\, g_0 N_0 S\right) \tag{5.14}$$

These results predict a reduction in the optical frequency deviation, known as chirp. Similar simulation results have also been published in. Experimental results, as shown in Figure 86, show that the frequency chirp is significantly reduced. The adiabatic and transient chirp are reduced by a factor of ~5, which implies that effectively, the linedwidth enhancement factor, α, has been also reduced. For the lasers used in the experiment, the α parameter was measured to be between 4-7. Thus, the injection-locked α is ~1.

From the discussions on fiber dispersion induced chirp and from optical amplifier non-flat gain induced chirp, it is clear that a low-chirp optical analog signal is desired. As shown experimentally and by simulation, injection-locking can significantly reduce the chirping of the frequency, and thus would lead to dramatic reduction in these fiber-induced distortions.

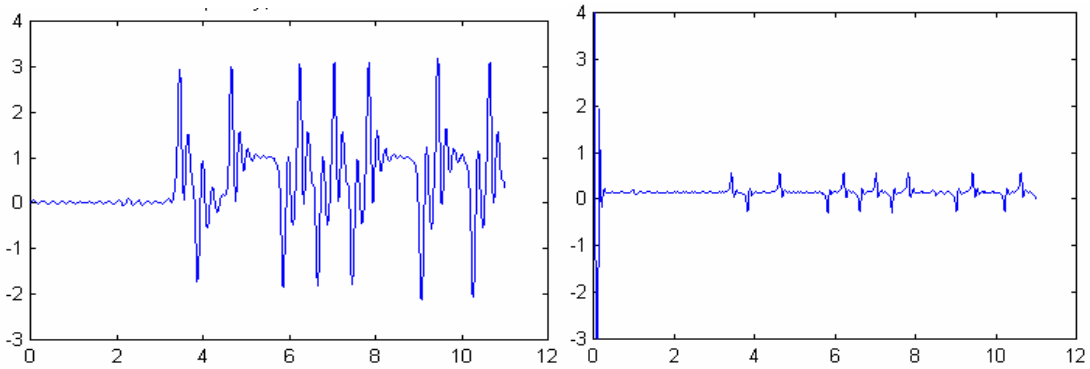

Figure 85 – Simulations of the reduction in chirp.
Left: free-running laser frequency, right: injection-locked laser frequency.
Note: scales are the same as in Figure 86.

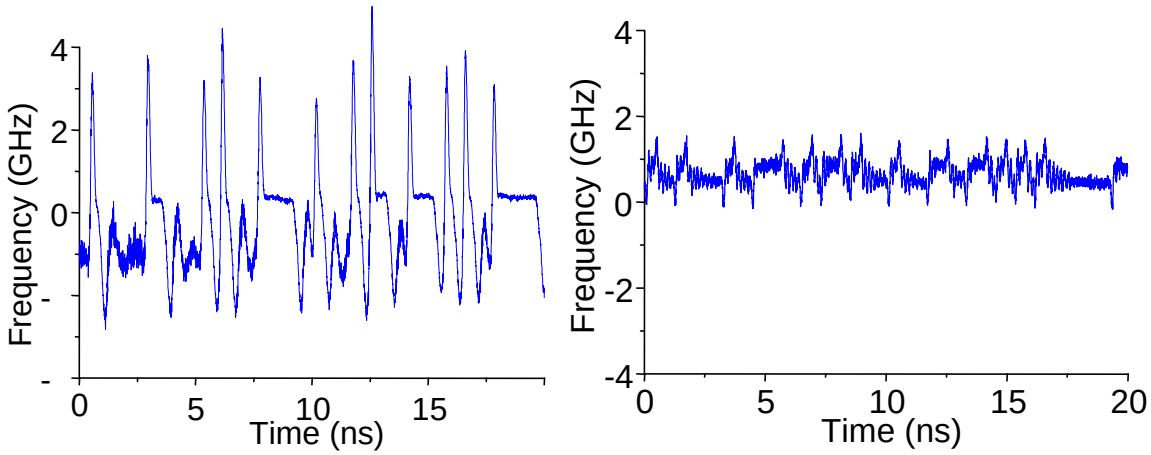

Figure 86 – Experimental reduction in chirp.
Left: free-running laser frequency, right: injection-locked laser frequency. The reduction in chirp corresponds to an effective reduction in the linewidth enhancement factor from 5 to ~1.

5.5. Summary

This chapter opened with an introduction to distortion, and its impact on multi-channel links. The composite-triple-beat is the most common metric used for multi-channel distortion characterization. The spur-free dynamic range is used to determine the largest possible dynamic range in the presence of noise and distortion in the link. Distortions in external modulators were described, with intermodulation distortion related to the composite-triple-beat. Clipping distortion was described. Next, directly modulated laser distortion was discussed, with theoretical results shown for free-running and injection-locked cases. It was shown that injection-locking can reduce the distortion for a broad frequency range. Both 3rd harmonic distortion and intermodulation distortion was studied.

Experimental results were presented demonstrating that injection-locking is an effective technique at reducing distortion. 3rd harmonic reduction was shown to be reduced for a broad range of injection parameters (wavelength detuning and injection power). The record 3f-SFDR results were shown for 1 and 2 GHz, with values of 112 dB-Hz$^{2/3}$ and 111 dB-Hz$^{2/3}$ respectively. A two-tone measurement was shown with an SFDR value of 103 dB-Hz$^{2/3}$.

Finally, fiber induced link distortion was considered. This distortion can be reduced with a small linewidth enhancement factor. Experimental evidence of injection-locking chirp reduction was presented, suggesting that fiber-induced distortion may be reduced with injection-locking.

Chapter 6 Applications

6.1. Uncooled Transmitter Using Locked Tunable VCSEL

The wavelength in current WDM transmitter lasers varies with temperature. This necessitates accurate temperature control as well as a wavelength stabilization system to ensure that each laser operates on the WDM grid. The addition of temperature and wavelength feedback control leads to a high power consumption, large size, and an increase in system complexity. Uncooled WDM-grid transmitters are thus extremely attractive for large systems and for applications involving a high number of low-cost transmitters (ex. fiber to the home). In contrast to a DFB laser, the wavelength of a tunable VCSEL can be maintained even as the temperature drifts, since we have an independent electrostatic control of the cavity length. Injection-locking of semiconductor lasers can be used for wavelength stabilization as well as performance improvement. We propose a new transmitter configuration that uses an uncooled injection-locked tunable VCSEL for maintaining wavelength stability over a range of temperatures. Furthermore, we propose using a mode-locked laser or an optical comb generator as the master laser to simultaneously lock an array of uncooled tunable lasers onto the WDM grid. In this work, we demonstrate for the first time that it is possible to achieve wavelength stability concurrently with an analog modulation performance improvement.

The injection locking technique has been demonstrated to enhance laser bandwidth, reduce non-linearities [137] and reduce chirp for direct current digital modulation applications [76, 138]. These properties can potentially lead to an increase of the bandwidth-distance product, and for analog applications, lead to an increase in dynamic range. The locking phenomenon occurs when an injection master laser is slightly detuned in wavelength relative to the follower laser. Depending on the frequency detuning and the injection power, the injection locked laser can be stably locked, unstably locked or exhibit chaotic behavior. A DFB laser injection locked with another DFB was demonstrated to have a three times enhancement in the small signal modulation and reduced dynamic distortions [18]. We have demonstrated that a large locking range (greater than 0.5 nm) is possible for VCSELs with high injection ratio conditions [137]. In analog transmission systems, the parameters of interest are the 3rd order distortions, fundamental tone power (RF gain), and noise floor (RIN). With injection locking, we have observed an increase in the spur-free dynamic range from 75 $dB \cdot Hz^{2/3}$ to 96 $dB \cdot Hz^{2/3}$ [137], with a detector thermal limited SFDR. An improvement in SFDR is observed over a very large detuning range of 0.2 nm to 0.5 nm.

6.1.1. Experiments

In this experiment, we study the analog performance of injection-locked VCSELs for ambient temperatures ranging from 20 to 50°C, demonstrating that the VCSEL wavelength can be locked to a WDM channel wavelength. The VCSELs are from Bandwidth 9 Inc., have a tuning range of ~20 nm and a threshold current of ~2 mA [7].

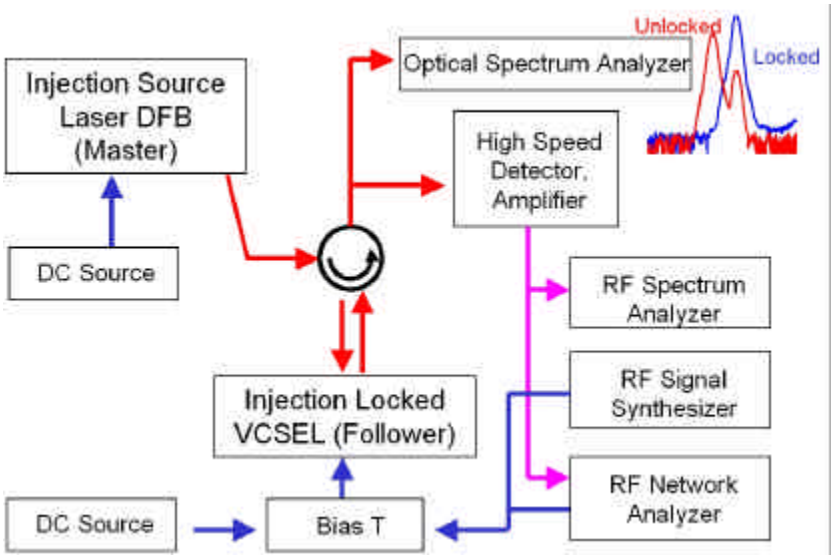

Figure 87 – Un-cooled transmitter; measurement system diagram

The experimental setup is shown in Figure 87. The output of the master DFB laser is injected through a circulator to the tunable VCSEL, which is actively temperature controlled to provide the ambient temperature in the range of interest. The performance of the tunable VCSEL is measured at the output port of the circulator, including small signal modulation response (S21) and spur free dynamic range (SFDR).

The DFB is biased at 100 mA and the DFB temperature tuned at a lasing wavelength of 1545.15 nm. The cantilever tuning voltage of the VCSEL controlled the detuning between the master and follower lasers. The VCSEL ambient temperature was controlled by a TEC, in a range of 20°C to 50°C. The VCSEL bias current was chosen to be 5 mA, which gives the peak power for the VCSEL at 50°C. It was found that the analog distortion observed at a peak power bias was similar to that for ½ peak power biasing. In other words, the non-linearity of the LI curve does not play a major role in RF

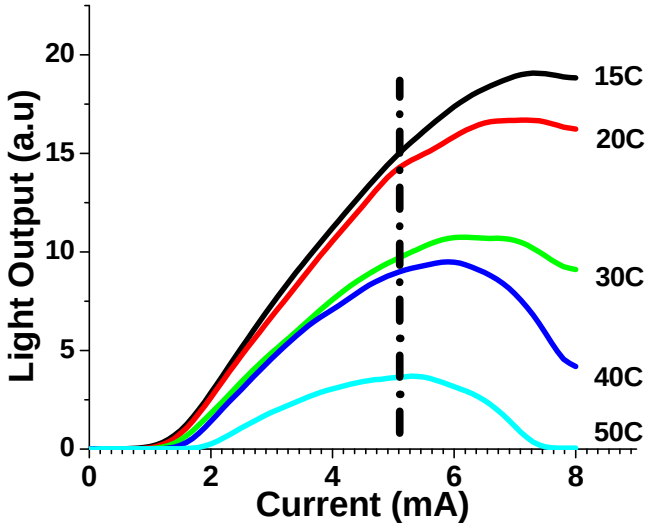

Figure 88 – Light output vs. current plots for temperatures 15-50°C

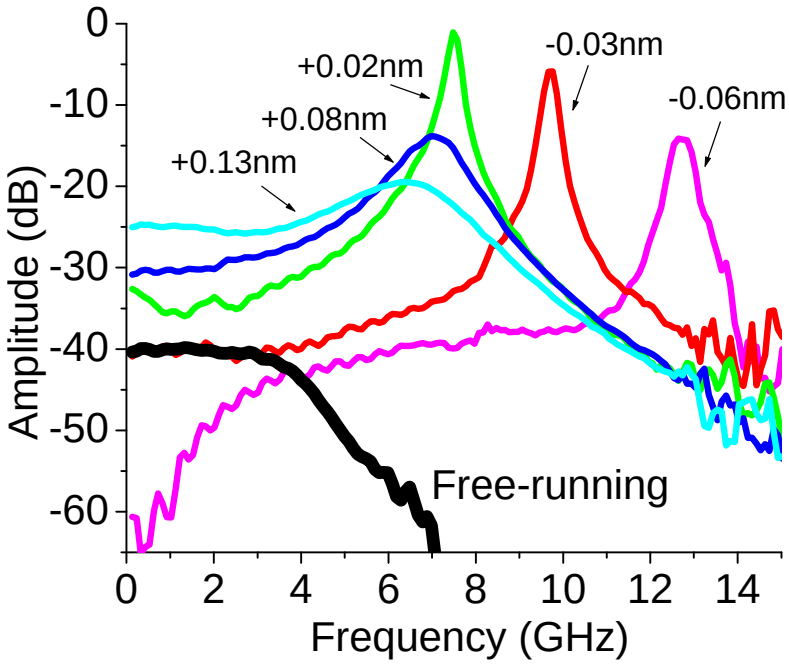

Figure 89 – Injection-locked VCSEL frequency response at 40°C
Free-running (3.8 GHz resonance frequency), and injection-locked (7-14 GHz) for detuning values ranging from -0.06 nm to +0.13 nm.

modulation distortion.

Figure 88 shows the LI curves for the chosen conditions indicating the 5 mA bias point.

The measured frequency responses (S21s) were calibrated for the device and packaging parasitics. The parasitic response was determined by the method used in [86], using the theoretical injection-locked frequency response [75] rather than the typical small-signal modulation response. The difference of two experimental injection-locked curves is curve-fitted with the difference of two theoretical injection-locked responses. The ideal response is then compared to the measured response, and the difference is the parasitic term. This procedure was performed several times to find the average parasitic response.

In Figure 89, the calibrated frequency response of the VCSEL at 40°C for various detuning values is shown. The free-running VCSEL shows a resonance frequency (f_r) of nearly 4 GHz, while the injection-locked f_r ranges from 7 to 14 GHz. The largest red-side detuning values (ex. -16 GHz or +0.13 nm detuning) result in the flattest frequency responses, with as much as 15 dB RF gain at lower frequencies (<4 GHz); this has been observed in several devices. The reason for the tremendous increase (and decrease for small detuning) in modulation efficiency is unknown, and has never before been predicted or observed.

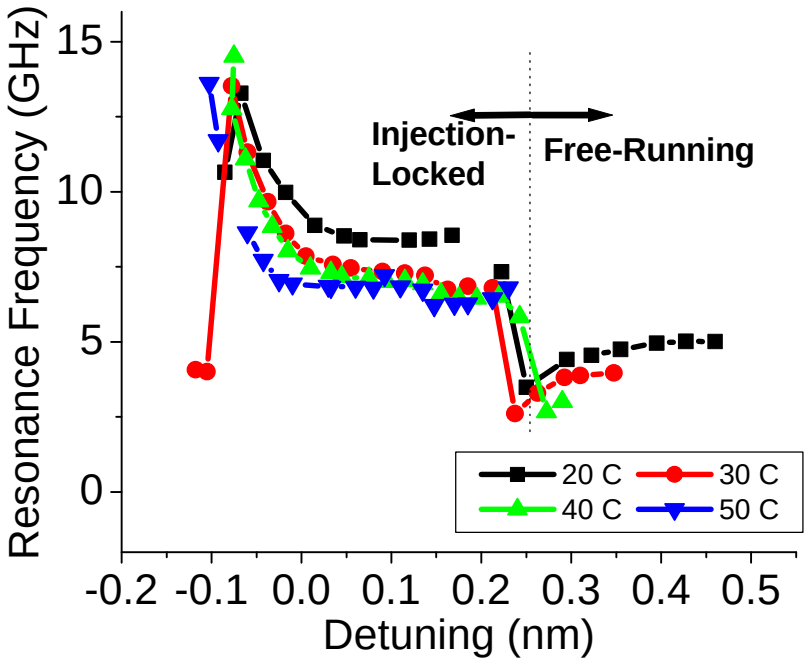

Figure 90 – Injection-locked VCSEL resonance frequency vs. detuning for 20-50°C.

In Figure 90, the resonance frequency is plotted versus wavelength detuning (as adjusted by the VCSEL tuning voltage), for temperatures 20-50°C. For all temperatures, we see a peak frequency of ~14 Ghz as well as a broad range of detuning values (0 to ~0.2 nm) that yield a uniform frequency response. For detuning values outside the locking range (approximately -0.1 nm to 0.25 nm), the VCSEL is unlocked, and the resonance frequency returns to its free-running value.

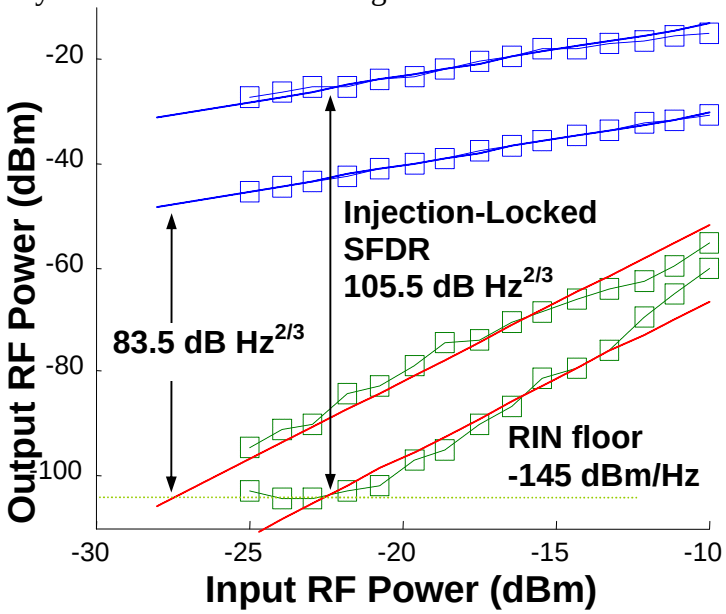

Figure 91 – Two-tone spur-free dynamic range improvement at 50°C
The detuning is ~0.2 nm. Inner lines (free-running), outer lines (injection-locked).

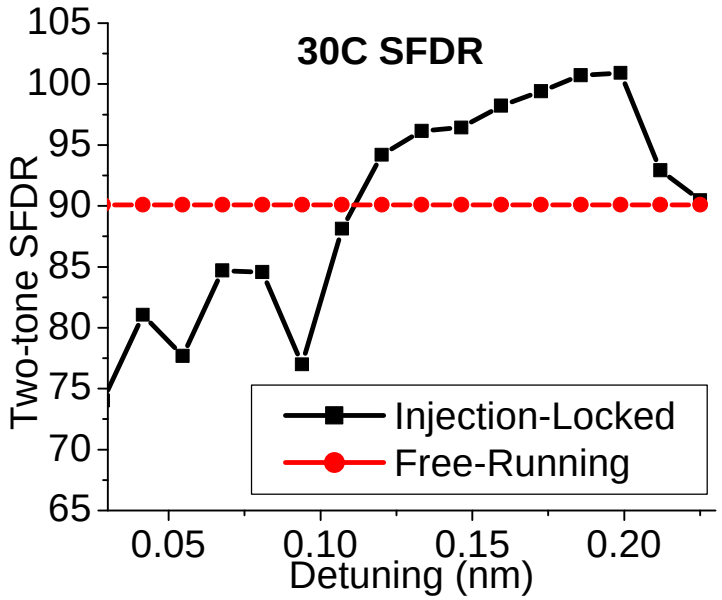

Figure 92 – SFDR, free-running and injection-locked versus detuning for 30°C.

Two-tone intermodulation distortion (IMD3) as well as single-tone third harmonic measurements were performed for 20-50°C. The data was collected in a separate experiment than the S21 data. A typical two-tone measurement, performed at 1.0 GHz (10 MHz tone spacing) is shown in Figure 91 for 50°C. The noise floor, at –105 dB/100 Hz, was limited by the detector noise, rather than laser RIN. The VCSEL RIN was measured to be -130 dB/Hz, which gives a RIN-limited noise floor of -145 dBm/Hz; this value is used in the SFDR calculations. The fundamental and IMD3 powers were fitted to slopes of 1 and 3 respectively. The spur-free dynamic range improved from the free-running value of 83.5 $dB \cdot Hz^{2/3}$ to an injection-locked value 105.5 $dB \cdot Hz^{2/3}$. A fundamental tone power increase of 17 dB and a distortion reduction of 15 dB were observed in this case. The fundamental tone power increase can be seen in the frequency response curves in Figure 89, where large detuning values result in the highest RF gain.

In Figure 92, the SFDR at 30°C is shown to improve for detuning values ranging from ~0.1 to ~0.2 nm.

For each injection condition and temperature, dynamic range and frequency response measurements are performed and compared to the free running references, shown in Figure 93. The top two curves are the two-tone spur-free dynamic range measurements. The free-running SFDR degrades with higher temperature, while the best-case injection-locked SFDR remains reasonably uniform between 98-103$dB \cdot Hz^{2/3}$, with an improvement ranging from 8-20$dB \cdot Hz^{2/3}$. The bottom curves are the resonance frequencies for free-running and locked cases. The free-running resonance frequency decreases with increasing temperature, while the injection-locked (for 0.1 nm detuning) resonance remains nearly constant at ~7.5 GHz.

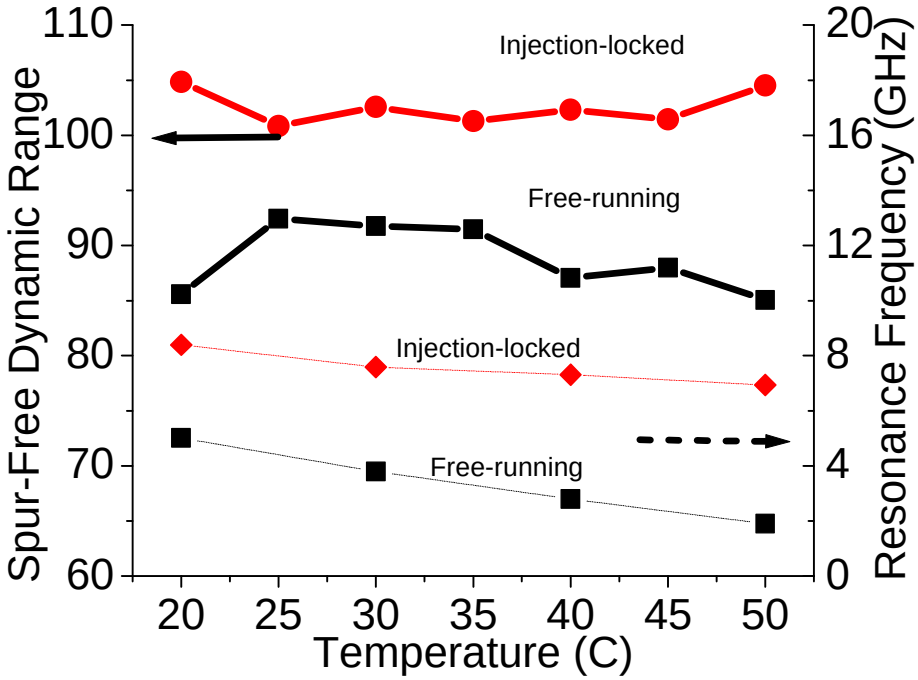

Figure 93 – Two-tone (1 GHz) Spur-free dynamic range at various temperatures
Top curves are the SFDR for both free running and injection locked cases.
The bottom curves are for resonance frequency, free-running and injection locked.

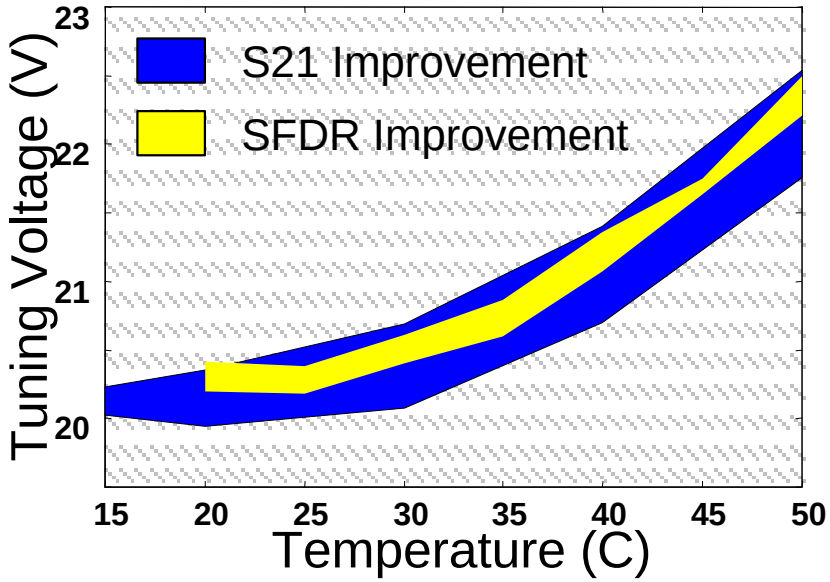

Figure 94 – VCSEL tuning voltage range for S21 and SFDR improvement.

In this experiment, the wavelength was not optimized and this condition did not yield the highest SFDR or resonance frequency values. For example, at another wavelength of 1543.5 nm with a large positive detuning, an injection-locked SFDR value of 108 dB·Hz$^{2/3}$ was observed at 15°C.

To address the issue of whether the injection-locking technique is plausible in a real-world system, we examine the locking range as it relates to the tuning voltage and

temperature reading parameters. The accuracy in detuning between the master and follower is not as stringent as one may imagine: an improvement in S21 is typically observed over a ±0.15 nm range, and a dynamic range improvement for ±0.06 nm. The S21 improvement is usually observed throughout the entire locking range. Figure 94 shows the tuning voltage applied to the VCSEL cantilever, for the temperature range 15-50°C. In the figure, the S21 and SFDR improvement ranges are shown. A bandwidth improvement is typically seen for a ±0.3V voltage range, while the SFDR improvement occurs over a ±0.1V range. Importantly, the region where the SFDR improves overlaps the S21 improvement region, and is for high detuning values.

6.1.2. Proposed Injection-locked Transmitter

We propose a novel architecture that exploits the injection locking technique to lock an array of tunable lasers to the ITU grid, while improving the modulation performance. Recently, a semiconductor mode locked laser at 1.55 um has been demonstrated to have a very stable amplitude and phase relation between different modes [139]. The mode spacing for the mode locked laser can be designed to match the ITU WDM grid. It is therefore possible to use this kind of mode locked laser to lock several channels simultaneously. Alternatively, an optical frequency comb generator [140] can be used as the master laser. Shown in Figure 95, the output of the mode locked laser is sent into a demultiplexer following a circulator, and each optical finger feeds and locks one laser, similar to our experimental setup. Because of the stable output from the mode locked laser, we expect that this 1-N injection locking architecture will have similar performance as to the experiment where each follower laser is injection-locked by its own master laser. In this application of the injection locking technique, only one temperature and wavelength controller will be required for the master laser, rather than for each transmitter.

The VCSEL tuning voltage would be adjusted according to curves similar to Figure 94, in the range where both the SFDR and S21 improve, ensuring that the wavelength of the VCSEL would be locked to the master ITU grid. Because the improvement range is relatively large, some error in the detuning control is tolerable (±0.1V) and the temperature reading does not have to be accurate.

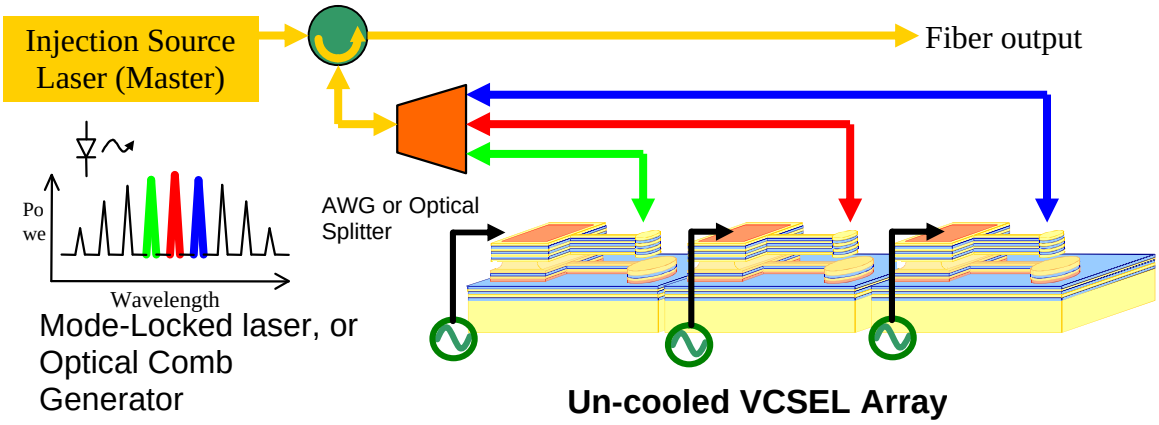

Figure 95 – 1-N locking architecture

6.2. VCSEL Design for Injection-Locking

In VCSEL injection-locking experiments, a very large locking range (0.6 nm) was observed. This large range is attributed to the large coupling coefficient (kc) of the VCSEL. The DBR sections in the VCSEL create a mode profile that yields the highest optical intensity in the quantum wells. This increases the injection optical field coupling into the VCSEL cavity, which leads to a large locking range, large resonance frequency improvements, and higher linearity.

The importance of the k_c parameter in determining the injection-locked laser characteristics is confirmed by the theory developed. The larger this parameter, the larger the locking range, the resonance frequency enhancement, and the lower the noise. A VCSEL designed for injection-locking would have a high k_c, which can be achieved by having a low mirror reflectivity.

This design consideration is opposite to designs for feed-back insensitivity. It has been shown experimentally that the mirror reflectivity plays an important role in the feedback sensitivity of a VCSEL [141]. A large reflectivity is desired for low feedback sensitivity. This corresponds to a small k_c coefficient.

Finally, the quantum wells can be designed with the most suitable alpha parameter. A large alpha parameter gives a larger locking range.

6.3. Monolithic Integration

Shown in Figure 96, the use of photonic crystals in VCSEL arrays is proposed. Photonic crystals can be designed to allow coupling of light from the horizontal direction to the vertical one. Thus, a master laser light propagating in the in-plane direction in a waveguide can be coupled to the vertical emission of the VCSEL, and lock the individual lasers.

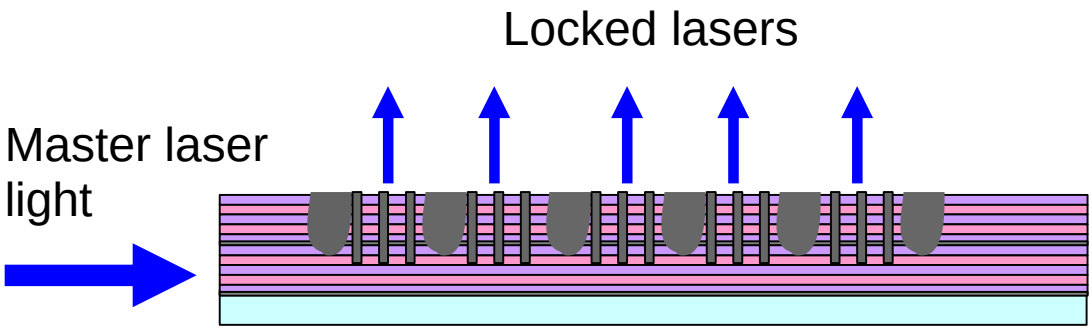

Figure 96 – VCSEL array with photonic crystals for vertical coupling.

6.4. Isolator-Free VCSEL Injection-Locking

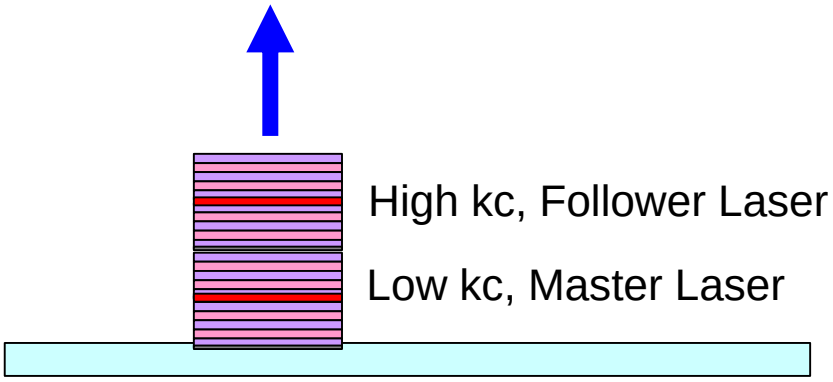

Figure 97 – Monolithic integration of master and follower VCSEL

Simulations are performed using two cavities, and two sets of injection-locked rate equations. Each laser has 3 equations. The coupling between the lasers is symmetric, with the assumption of zero phase delay between the lasers. The wavelength detuning is defined as the locked wavelength minus the original free-running wavelength of the first laser.

Figure 98 shows the stability plot for the case of the two lasers having a kc parameter differing by a factor of 100. The stability plot considers the wavelength detuning and the coupling coefficient between the two lasers. In the left figure, the o symbols represent a stable locking, while the x represents an unlocked situation. The resulting frequency (wavelength) of the locked system is shown in the right figure. In this case, the resultant wavelength is approximately that of the original laser (with the smaller kc value).

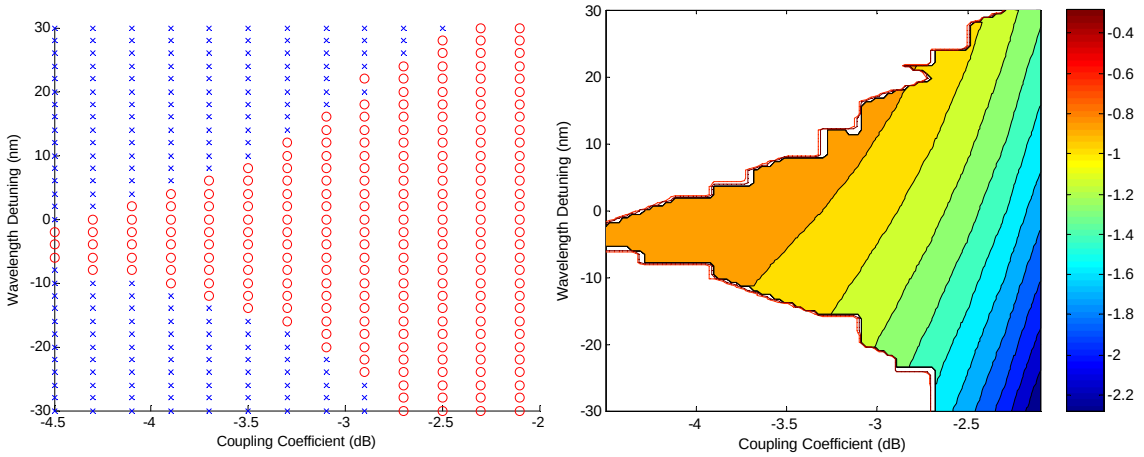

Figure 98 – Isolator-free injection stability plot
kc of laser 1 = 1/100 kc laser 2

Figure 99 shows the case where the two lasers are identical, in terms of the kc parameter. As can be seen in Figure 99, the wavelength deviation from the original free-running wavelength can be as high as 120 GHz (> 0.8 nm). The system of two lasers can be used as a tunable laser source.

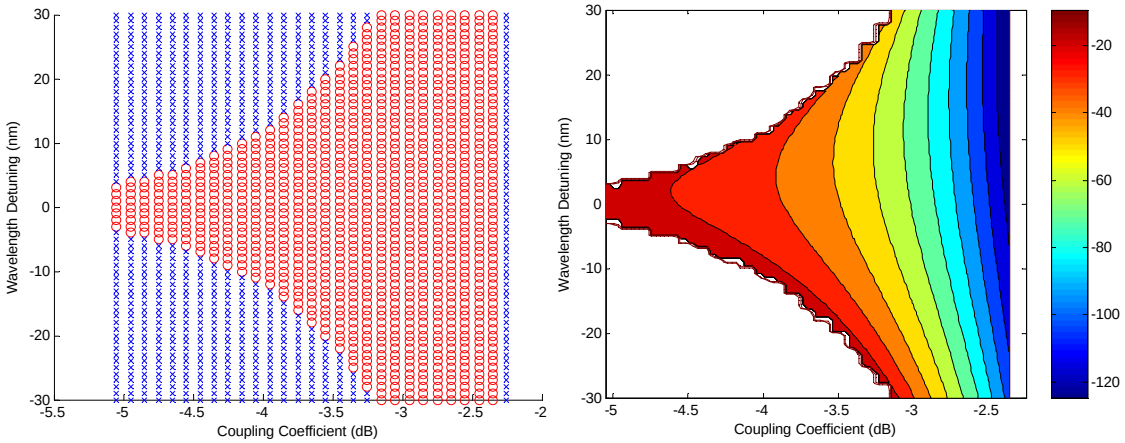

Figure 99 – Isolator-free injection stability plot, equal kc

6.4.1. Conclusion

In this work, we have proposed an un-cooled VCSEL transmitter for WDM applications. The highest reported SFDR of 105.5 dB-Hz$^{2/3}$ was achieved for a VCSEL at 1 GHz. We have demonstrated that it is possible to choose tuning voltage parameters for a tunable VCSEL such that its wavelength remains locked and yields performance enhancements for temperatures in the range of 20°C to 50°C. The spur-free dynamic range was improved and is greater that 100 dB·Hz$^{2/3}$, while the frequency response showed an RF gain with a flat response and a nearly uniform resonance frequency of ~8 GHz. We demonstrate that with a continuously tunable VCSEL, it is possible to use the tuning voltage to ensure wavelength locking and performance enhancements through temperature variation. This demonstrates the feasibility of un-cooled VCSEL transmitters injection-locked to a WDM reference grid, and suggests possible future work in monolithic integration of WDM injection-locked tunable VCSEL arrays. A transmitter architecture is proposed, that uses one master laser to lock several lasers.

Chapter 7 Conclusion

This thesis discussed the technique of optical injection-locking, involving a transmitter laser locked in wavelength to a master laser. With the transmitter laser locked in phase to the master due to the coherent non-linear interaction, the laser characteristics fundamentally change and can result in far better device performance.

Unlike locking experiments with edge-emitting structures, locking VCSELs proved to be much easier than expected due to the high Q cavity in a VCSEL, resulting in a large locking range and a low required injection power. In agreement with our models, the VCSEL resonance frequency increased from 4 to a stellar 28 GHz, yielding a record VCSEL bandwidth of nearly 40 GHz.

Analog fiber optic communication, or radio-over-fiber, is gaining popularity and is useful for CATV and wireless-networking signal distribution, and cellular telephone access. These applications necessitate that links have a high linearity and dynamic range. To improve laser transmitter performance, optical injection-locking can be employed; we have reduced laser distortion by up to 35 dB, increased modulation efficiency by 5-10 dB, and measured a record VCSEL spurious-free dynamic range (SFDR) value of 111 dB $Hz^{2/3}$ at 2 GHz. We have also observed a broadband noise reduction in VCSELs, as high as 10 dB, further improving the dynamic range.

The wavelength and temperature control is the bulkiest and most energy consuming component in a transmitter module, and we have shown that injection-locking can be used to eliminate these burdens. Using tunable VCSELs with injection-locking, we have shown that the devices become temperature insensitive and remain locked in wavelength over an ambient temperature range, with an improved frequency response and linearity. With the demonstrated improvements in directly modulated laser transmission, high performance transmitters using injection-locking can be accomplished.

The thesis work has shown a complete set of evidence indicating that the injection-locking technique can be extremely effective at improving the performance of semiconductor lasers for analog applications, in particular, vertical cavity lasers. This technique will enable higher speed analog and digital fiber communications, reaching much higher modulation speeds, with reduced noise and distortions.

7.1. Future Work

Recent experiments suggest that resonant frequencies as high as 60 GHz may be possible using the BTJ-VCSELs, leading the way for further studies that may reveal a new understanding of laser physics no longer constrained by previous limitations. As the experiments in this thesis were limited by a 22 GHz detector, future experiments should be performed with higher speed detectors and signal analyzers. Small-signal modulation results demonstrating the 60 GHz resonance frequencies would be very exciting indeed!

The research completed to date on optical injection-locking is just the tip of the iceberg. A natural extension is to consider using arrays of VCSELs as a high channel count wavelength division multiplexed (WDM) transmitter. Optical injection-locking could give the necessary performance boost to the VCSELs. Integrated with flip-chip bonded CMOS RF driving circuitry, coupled into optical fiber, and using only a single

master laser, such a transmitter would drastically decrease the cost and size of a 100 wavelength channel transmitter. Device research should be directed at monolithic integration of the master laser with an injection-locked array, which has also never been done, and could be implemented by using photonic crystals.

Optical injection-locking experiments on quantum dot lasers could be performed. The higher differential gain of these materials may yield even more impressive modulation results.

Appendix A – Matlab Simulation Code

7.2. Injection-locking VCSEL rate equations

```
% Injection locking equations:
function dy = injection_eqs(t,y,ss2, Tinj, arrays)
% ss2 = [ detune  Im  I_follower digitalanalog freq1 freq2  phi_fit_off  phi_fit_sl
Sinj_av  Nth_follower];
% arrays: [ Sinj phi_inj signal ];

% physical parameters for typical VCSEL
Lcavity = 1e-4;        % cavity length in cm
Lactive = 24e-7;       % active region length in cm, assume 3 QW, 8nm each
Amesa = 4e-6;  % mesa size in cm^2, assume 20um x 20um
Vactive = Lactive*Amesa;      % active region volume in cm^3
R = 0.998;             % mirror reflectivity for the output/injection DBR
N0_density = 1.8e18;  % transparency carrier number
Jth = 1005;    % in A/cm^2
dgdn = 2e-16;  % differential gain, cm^2
vg = 8.5;              % group velocity, cm/ns
epsilon = 20e-8;       % gain compression factor
%epsilon = 5e-8;       % gain compression factor
Tp = 2e-3;             % photon lifetime, in ns
Rsp = 2e3;     % spontaneouse emission rate, 1/ns
alpha = 3;     % linewidth enhancement factor
Ts = 2;        % carrier lifetime, in ns
Fs = 0; Fphi = 0; Fn = 0;     % noise terms
e = 1.6e-19;
Vactive = Lactive*Amesa;      % active region volume in cm^3
kc = sqrt(1-R)*vg/Lcavity;    % derived definition, coupling rate 1/ns
gamma = 2*Lactive/Lcavity*0.9;        % 2 is the enhancement factor, assume 90%
confinement in the transverse direction
G0 = gamma*dgdn*vg/Vactive;
N0 = N0_density*Vactive;              % convert density to carrier number
if ss2(10) == 0
    Nth_density = Jth*Amesa*Ts/e/Vactive/1e9;    Nth = Nth_density*Vactive;
    Ith = Jth*Amesa;  % in A
else;    Nth = ss2(10);    Ith = ss2(10)/Ts*e*1e9;end
% convert to coulumb/ns
if ss2(2) == 0 % DC analysis
    I=ss2(3)*Ith*1e-9;
else   % analog modulation
    signal = sin(2*pi*ss2(5)*t)+sin(2*pi*ss2(6)*t);
    I = (ss2(3)+ss2(2)*signal)*Ith*1e-9;
end
phi_inj_t = ss2(7) + ss2(8) * t;   Sinj_t = ss2(9);
global inj_noise
if inj_noise
    global stepsize
    dt=abs(stepsize);
    Fs =   sqrt ( 2 * y(1) * Rsp / dt ) * randn;
    Fphi = sqrt ( Rsp / dt / 2 / (y(1)+realmin) ) * randn;
    Fn =   sqrt ( 2 * y(3) / dt / Ts ) * randn - Fs;
end
if imag(Fs)~=0;dy=[NaN;NaN;NaN];break;end

% Let y(1) = s(t); y(2) = phi(t); y(3) = n(t)
dy = [0;0;0];
dy(1) = (G0*(y(3)-N0)/(1+epsilon*y(1))-1/Tp)*y(1) + Rsp...
    +2*kc*sqrt(y(1)*Sinj_t)*cos(y(2)-phi_inj_t) + Fs;
dy(2) = alpha/2*G0*(y(3)-Nth)-ss2(1)*2*pi...
    -kc*sqrt(Sinj_t/(realmin+y(1)))*sin(y(2)-phi_inj_t) + Fphi;
dy(3) = I/e-y(3)/Ts-G0*(y(3)-N0)/(1+epsilon*y(1))*y(1) + Fn;
return % injection_eqs
```

7.3. Free-running VCSEL rate equations

```
function dy = rate_eqs(t,y)
global  I_master t_start tf
e = 1.6e-19;
mLcavity = 1e-4;              % cavity length in cm
mLactive = 24e-7;     % active region length in cm, assume 3 QW, 8nm each
mAmesa = 4e-6; % mesa size in cm^2, assume 20um x 20um
mR = 0.998;           % mirror reflectivity for the output/injection DBR
% material properties
mN0_density = 1.8e18;  % transparency carrier number
mJth = 1005;   % in A/cm^2
mDgdn = 4e-16; % differential gain, cm^2, e.g. 2e-16
mVg = 8.5;            % group velocity, cm/ns
mEpsilon = 5e-8;      % gain compression factor
mTp = 2e-3;           % photon lifetime, in ns, e.g. 4e-3
mRsp = 2e3;    % spontaneouse emission rate, 1/ns
mAlpha = 3;    % linewidth enhancement factor, e.g. 2
mTs = 2;              % carrier lifetime, in ns

% physical parameters for typical VCSEL
mVactive = mLactive*mAmesa;   % active region volume in cm^3
% material properties
gamma = 2*mLactive/mLcavity*0.9;      % 2 is the enhancement factor, assume 80%
confinement in the transverse direction
G0 = gamma*mDgdn*mVg/mVactive;
N0 = mN0_density*mVactive;            % convert density to carrier number
Nth_density = mJth*mAmesa*mTs/e/mVactive/1e9;
Nth = Nth_density*mVactive;
Ith = mJth*mAmesa;     % in A

% convert to the correct unit, coulumb/ns
I = I_master*Ith*1e-9;
% Let y(1) = s(t); y(2) = phi(t); y(3) = n(t)
dy = zeros(3,1);
dy(1) = (G0*(y(3)-N0)/(1+mEpsilon*y(1))-1/mTp)*y(1) + mRsp;% + mFs;
dy(2) = mAlpha/2*G0*(y(3)-Nth); %- mFphi/y(1);
dy(3) = I/e-y(3)/mTs-G0*(y(3)-N0)/(1+mEpsilon*y(1))*y(1); % + mFn;
```

7.4. Injection-locked small-signal modulation response

```
function [fr,f3db,locked]=frequency_response( detuning, inj_eff, ff,t_start, phi_fit,
Sinj_av, Nth_follower, I_follower, t_resolution, init, locked, PLOT_S21 )

% calculate the S21 frequency response, point by point, using rate equations.
global INJECTION
Im=.1;
t_start=1;
result = zeros(length(ff),2);
result(:,1) = ff';
for ii = 1:length(ff);
    fmod = ff(ii);
    tf = max(t_start+1,t_start+3/fmod);      % calculate at least 3 periods
    tf = t_start+3/fmod;      % calculate at least 3 periods
    t_resolution = .021/fmod;
    ss2 = [ detuning Im I_follower 0 fmod 0 phi_fit Sinj_av Nth_follower];
    tol=1e-10;options=odeset('AbsTol',tol,'RelTol',tol,'MaxStep',0.025); %1e-7: noise ~85
    tic;[t,y] =
ode113(@injection_eqs,[0:t_resolution:tf],init,options,ss2);ode_time3=toc;
    Tp = 2e-3;        % photon lifetime, in ns
    y(:,1) = y(:,1)*6.626e-34*3e8/1.55e-6*1000/Tp/1e-9*0.6/2;      % mW
    %     figure;plot(t,y(:,1))
    t1 = find(t>tf-1.2/fmod);    % use the 2 ~ tf as the guage for the frequency response
    t1 = t1(1);
    % get rid of the NaN in case the solution of ode doesn't come out right
    result(ii,2)=-inf;
    for jj = 1:length(t)
        if y(jj,1)/y(jj,1)==1;            t2 = jj;        else;            break;
end
```

```
    end
    [X,RESNORM,RESIDUAL,EXITFLAG,OUTPUT]=lsqcurvefit(@sine_eq,[0
mean(y(t1:t2,1))],t(t1:t2),y(t1:t2,1),[-pi -inf],[pi
inf],optimset('MaxIter',2e2,'MaxFunEvals',5e6,'Display','off'),fmod);
    %     figure;plot( t(t1:t2),y(t1:t2,1) );      plot
(t(t1:t2),sine_eq(X,t(t1:t2),fmod),'g');
    result(ii,2) = max(y(t1:t2,1))-min(y(t1:t2,1));
    result(ii,3) = X(1); if ii>1;if (result(ii,3)-result(ii-
1,3))>0.6*2*pi;result(ii,3)=result(ii,3)-2*pi;end;;if (result(ii-1,3)-
result(ii,3))>0.8*2*pi;result(ii,3)=result(ii,3)+2*pi;end;end
end
% result(:,2) = 20*log10(result(:,2)/result(1,2));
result(:,2) = 20*log10(result(:,2));        % 2 for converting E field to # photons.
t=find ( result(:,2) <= -3 + result(1,2) );  if ~isempty(t);f3db=result(t(1),1);
else;f3db=0;end % 3dB frequency
if f3db < 5; locked=locked-.1;end     % check to see if the frequency is high enough.
if ( ( min (result(:,2) ) - result(1,2) ) < -20 ); locked=locked-.5; end   % check for
strange/lousy S21

if ~INJECTION %Save free-running S21, load if injection calculation.
    dlmwrite ('free-running.s21',result);
else;     result_free=dlmread('free-running.s21');[Xf]=fit_s21_inj
(result_free(:,1),result_free(:,2)
);freqs_free=result_free(1,1):.05:result_free(end,1);YDATA_fit_free =
fit_modulation_inj(Xf,freqs_free);        dlmwrite ('inj.s21',result);
end

[X]=fit_s21_inj (result(:,1),result(:,2) );
global PLOT_S21_Phase fmax_plot
freqs=result(1,1):.05:result(end,1);YDATA_fit = fit_modulation_inj(X,freqs);
t=find ( YDATA_fit <= -3 + YDATA_fit(1) );  if ~isempty(t);f3db=YDATA_fit(t(1));
else;f3db=0;end % 3dB frequency
fr=X(3);
S21_LOG=0;
if PLOT_S21 % plots
    figure;ax(1) = newplot;
    set(gcf,'nextplot','add')
    if S21_LOG;    semilogx(result(:,1),result(:,2), 'bo');hold on;    semilogx
(freqs,YDATA_fit,'b','linewidth',2);else;    plot(result(:,1),result(:,2),
'bo','linewidth',2);hold on;    plot (freqs,YDATA_fit,'b','linewidth',2);end
    if INJECTION;if S21_LOG;    semilogx(result_free(:,1),result_free(:,2), 'ro');hold
on;    semilogx (freqs_free,YDATA_fit_free,'r','linewidth',1);else;
plot(result_free(:,1),result_free(:,2), 'ro','linewidth',2);hold on;    plot
(freqs_free,YDATA_fit_free,'r','linewidth',2);end;end
    set(ax(1),'box','off')
    title(strcat('I_bias = ', num2str(I_follower),' xIth','  Im = ',num2str(Im),'
xIth',...
        ' inj_eff =  ',num2str(inj_eff),', detuning =  ',num2str(detuning),'
GHz'),'FontSize',14);
    xlabel('Frequency (GHz)','FontSize',14);ylabel('Response (dB)','FontSize',14);xlim([0
fmax_plot])
    if PLOT_S21_Phase
        ax(2) = axes('position',get(ax(1),'position'));hold on;
        if S21_LOG; semilogx (result(:,1),result(:,3)/pi,'g','linewidth',1);else;plot
(result(:,1),result(:,3)/pi,'g','linewidth',1);end;hold on;
        if INJECTION;if S21_LOG; semilogx
(result_free(:,1),result_free(:,3)/pi,'m','linewidth',1);else;plot
(result_free(:,1),result_free(:,3)/pi,'m','linewidth',1);end;end
        set(ax(2),'YAxisLocation','right','color','none',
'xgrid','off','ygrid','off','box','off');
        ylabel ('RF Phase (x Pi)','FontSize',14);xlim([0 fmax_plot])
    end
end

function [y]=sine_eq (x,xdata,fmod)
% x(1)=phase, x(2)=DC
y=sin ( 2*pi*fmod*xdata+x(1)) +x(2);
```

7.5. Small-signal modulation response function fit

```
function [y] = fit_modulation_inj (x,xdata)
% modulation function with parasitic rolloff term.  This is the same as injection-locked
% modulation function with parasitic rolloff term.  This is the same as injection-locked
S21
% | H(f) | ^2   --- thus 10 magnitude coefficient.
% x(1) = f_o
% x(2) = gamma
% x(3) = f_r
% x(4) = constant offset
% x(5) = mag
% x(6) = numerator 1
% x(7) = numerator 2
x=real(x);
y=x(4)+x(5)*log10 ( 1  ./ (1 + ( xdata / x(1) ) .^2 ) ./ ( ( 1 - ( xdata ./ x(3) ) .^2 )
.^2 + ( x(2)/2/pi./x(3).*xdata./x(3) ).^2 ) );

function [X]=fit_s21_inj (XDATA, YDATA)
if length(YDATA)>0
    X0=[5   5  5  YDATA(1) 10 1 1];

[X,RESNORM,RESIDUAL,EXITFLAG,OUTPUT]=lsqcurvefit(@fit_modulation_inj,X0,XDATA,YDATA,[1 1
1 -150 0 -inf -inf],[200 200 50 150 20 inf
inf],optimset('MaxIter',2e2,'MaxFunEvals',5e6,'TolFun',1e-16,'TolX',1e-
6,'MinAbsMax',1e52, 'Display','on'));
    if RESNORM >
1000;[X,RESNORM,RESIDUAL,EXITFLAG,OUTPUT]=lsqcurvefit(@fit_modulation_inj,X0,XDATA,YDATA,
[1 1 1 -50 0 -inf -inf],[50 50 30 15 20 inf
inf],optimset('MaxIter',1e3,'MaxFunEvals',5e6,'TolFun',1e-16,'TolX',1e-
7,'MinAbsMax',1e52, 'Display','on'));end
    [X    RESNORM]
end
```

7.6. Distortion analysis

```
function [distortion,simulation_pt,solve_time]=frequency_response_distortion( detuning,
inj_eff, frequencies, delta_freq,t_start, phi_fit, Sinj_av, Nth_follower, I_follower,
t_resolution, init, locked, PLOT_FREQ_IMD, PLOT_TIME_TRACE,
PLOT_SPECTRUM,simulation_pt,solve_time, Im,ODE_TIME_MAX,tf,
sTp,distortion,INJECTION_FULLSOLN )
% calculate the distortion frequency response, point by point, using rate equations.
global INJECTION

for freq1=frequencies;
    Nyquist =  3.25* (freq1+delta_freq/2);   % aliasing in the frequency domain causes
overlap of the 3rd harmonics...
    if delta_freq~=0; tf=tf*2;else;tf=tf*2;end
    f_sample = 2 * Nyquist; t_resolution = 1/f_sample;             % in ns, time spacing
for the solutions from laser rate equations

    % solve the rate equation and keep only the part after t_start
    clear t y;
    tol=2.3e-14; tol=1e-5; options=odeset('AbsTol',tol,'RelTol',tol,'Stats','off');
       %1e-7: noise floor ~85
    if delta_freq~=0; freq2=freq1+delta_freq; else;freq2=0;end
    ss2 = [ detuning Im I_follower 0 freq1 freq2 phi_fit Sinj_av Nth_follower];
    tic;[t,y] = ode113(@injection_eqs,[0 .01],init,options,ss2); ode_time=toc;
    if ode_time > ODE_TIME_MAX/2;locked=locked-2;disp('locked-2: too long');end
    if locked>0;
        tic;[t,y] = ode113(@injection_eqs,[0 1],init,options,ss2); ode_time=toc;
        %            if PLOT_TIME_TRACE2     ;        plot_result(t,y);       end
        % check if it is locked:
        tt = t; tt(1)=[]; tt = tt-t(1:length(t)-1); phi = y(:,2); phi(1)=[]; phi = (phi-
y(1:size(y,1)-1,2));u=find(t>0.6)-1;frequency_deltamax=max(phi(u)./tt(u)/2/pi)-
min(phi(u)./tt(u)/2/pi)
        if frequency_deltamax > 10; locked=locked-8;disp('frequency delta to big');end
    end
    if ode_time > ODE_TIME_MAX;locked=locked-4;disp('locked-4: too long');end
```

```
    if locked > 0 & (~INJECTION | INJECTION_FULLSOLN )
        % tol = 1e-6: fast and good enough for most IMD3/3rd harmonic.
        % tol=2.3e-14;  best, tol = 1e-9, good for 3rd harmonic.
        tol=2.3e-14;     tol=1e-6;            options=odeset('AbsTol',tol,'RelTol',tol);
       %1e-7: noise floor ~85
        tic;[t,y] = ode113(@injection_eqs,[0 t_start],init,options,ss2);
ode_time2=toc;solved_ODE=1;
        init = y(length(t),:);
        tic;[t,y] = ode113(@injection_eqs,[t_start:t_resolution:(tf+t_start-
t_resolution)],init,options,ss2); ode_time2=toc;solved_ODE=1;
    else
        solved_ODE=0;                    ode_time
    end
    solved_ODE
    if solved_ODE==1;
        % convert to mW, sTp in ns, assume 1.55um
        % also assume 60% photon loss is the mirror loss and half of it output from the
top mirror
        y(:,1) = y(:,1)*6.626e-34*3e8/1.55e-6*1000/sTp/1e-9*0.6/2;
%         % remove the turn on transient portion. real signal starts from t_start
         index = find(t >= t_start);     index = index(1);
         t = t(index:length(t));        y = y(index:size(y,1),:);
        Pave = mean(y(:,1));  % Pout = [Pout, Pave];      % output power.
        if PLOT_TIME_TRACE           % plot the laser output as a function of time
            plot_result(t,y);
        end

        [f, specdata, RIN]=spectral_analysis (t,y, f_sample,2);
        [distortion1]=SFDRcalc (freq1, freq2, f, specdata, Im, INJECTION);
        distortion=[distortion; distortion1];

        if PLOT_SPECTRUM
            figure;hold on;                subplot(2,1,1);hold on;
            plot(f,specdata);xlim([0 Nyquist])      % plot out the typical spectrum
            subplot(2,1,2);hold on;plot(f,RIN); xlim([0 Nyquist]) % plot out the RIN
spectrum
            if INJECTION; cond = [inj_eff detuning];else; cond = [0 0]; end
            title(num2str(cond));
        end

    end % solved_ODE
end % frequencies
% simulation time data
simulation_pt=simulation_pt+1;        solve_time (simulation_pt,:)=[ detuning inj_eff Im
ode_time ode_time2  ]
if PLOT_FREQ_IMD
%     figure; %         distortion=[freq1 freq2 Im p1 p2 p3 pimd3];
  hold on;  plot ( distortion(:,1),distortion(:,4:7)); distortion = [];
end

function [distortion]=SFDRcalc (freq1, freq2, f, specdata, Im, INJECTION)
% Find the 1st, 2nd, 3rd harmonics.
if freq1~=0    % if modulated
    temp = abs(f - freq1);
    p1 = find(temp==min(temp));p1=p1(1);     % find closest frequency point.
    p1 = specdata(p1(1)); p3=0;pimd3=0;p2=0;
    if freq2 ~= 0     % two tone modulation
        temp = abs(f - freq2);
        p1b = find(temp==min(temp));p1b=p1b(1);     % find closest frequency point.
        p1b = specdata(p1b); p1=(p1b+p1)/2;
        temp = abs(f - 2*freq1+freq2);
        p12 = find(temp==min(temp));p12=p12(1);
        p12 = specdata(p12);
        temp = abs(f - 2*freq2+freq1);
        p21 = find(temp==min(temp));p21=p21(1);
        p21 = specdata(p21);pimd3=(p12+p21)/2;
        disp([freq1 Im p1 pimd3])
        if length(find(f==2*freq1-freq2)) == 0      % when the 3rd order intermodulation
is on the frequency grid
            disp('Warning: 3rd order intermodulation frequency not on the grid')
        end
```

```
    else       % single tone modulation, find the 3rd order power
        temp = abs(f - 2*freq1);
        p2 = find(temp==min(temp));p2=p2(1);
        p2 = specdata(p2);
        temp = abs(f - 3*freq1);
        p3 = find(temp==min(temp));p3=p3(1);
        p3 = specdata(p3);
        disp([freq1 Im p1 p2 p3])
    end
    distortion=[freq1 freq2 Im p1 p2 p3 pimd3];
end    % if modulated
fid = fopen('simul-oct2803-3rd harmonic.txt','a');
fprintf(fid,'%10.2f %10.2f %10.2f %10.2f %10.2f %10.2f\n',[freq1 freq2 Im p1 p2 p3
pimd3]);
fclose(fid);

function SFDR=SFDRcalc2 ( distortion, PLOT_IMD, detuning, inj_eff, SFDR_free )
disp ('Plotting IMD3')
distortion
    figure; %         distortion=[freq1 freq2 Im p1 p2 p3 pimd3];
    plot ( distortion(:,3),distortion(:,4:7));

col1 = 3;   % modulation power
col2 = 4;   % fundamental tone
col3 = 7;   % IMD3 or 3rd harmonic
col2nd = 5; % 2nd harmonic
distortion(:,col1)=10*log10(distortion(:,col1));
distortion
m1 = fit_line1(distortion(:,col1),distortion(:,col2));
m2 = fit_line2(distortion(:,col1),distortion(:,col2nd));
[m3,sfdr_error] = fit_line3(distortion(:,col1),distortion(:,col3));
Nfloor=-120; % noise floor for SFDR
x = (Nfloor - m3(1))/3;       % interception point of 3rd order line with noise floor
SFDR = (m1(2)-3)*x+ m1(1)-m3(1);
if  PLOT_IMD
    figure;hold on
    plot(distortion(:,col1),distortion(:,[col2]),'rs');
    plot(distortion(:,col1),distortion(:,[col3]),'ks');
    t=axis;shift=(t(2)-t(1)) *.5;
    plot(distortion(:,col1),distortion(:,col1)*1+m1(1),'b')
    text(distortion(1,col1)+shift, distortion(1,col1)*1+m1(1)+5,strcat('y =
',num2str(1),'x +',num2str(m1(1))),'Color','b');
    plot(distortion(:,col1),distortion(:,col1)*2+m2(1),'b')
    text(distortion(1,col1)+shift, distortion(1,col1)*2+m2(1)+5,strcat('y =
',num2str(2),'x +',num2str(m2(1))),'Color','b');
    plot(distortion(:,col1),distortion(:,col1)*3+m3(1),'b')
    text(distortion(1,col1)+shift, distortion(1,col1)*3+m3(1)+5,strcat('y =
',num2str(3),'x +',num2str(m3(1))),'Color','b');
    text(distortion(1,col1)+shift, distortion(1,col1)*3+m3(1)+8,strcat('SFDR =
',num2str(SFDR),' dB Hz^2^/^3'),'Color','b');
    text(distortion(1,col1)+shift, distortion(1,col1)*3+m3(1)+11,strcat('delta SFDR =
',num2str(SFDR-SFDR_free),' dB Hz^2^/^3'),'Color','r');
    text(distortion(1,col1)+shift, distortion(1,col1)*3+m3(1)+14,strcat('Detuning=
',num2str(detuning),'  Injection_eff',num2str(inj_eff)),'Color','r');
end   % PLOT_IMD
```

7.7. RF spectrum analysis

```
% return the RIN and RF spectrum.
function [f, specdata, RIN, spec_tot, RIN_tot]=spectral_analysis (t,y, f_sample,window)
global MATLAB_NOLICENCE
if MATLAB_NOLICENCE;window=4;end
switch window
    case 1
        w = chebwin(length(y(:,1)), 1000);
    case 2
        w = chebwin(length(y(:,1)), 100);
    case 3
        w = kaiser(length(y(:,1)),0.1102*(100-8.7));        % best one.
```

```
    case 4
        w = dlmread (strcat('window',num2str(length(y(:,1))),'.dat'));
    otherwise
        w=ones(length(y(:,1)),1);
end
if 0; dlmwrite (strcat('window',num2str(length(y(:,1))),'.dat'),w);end  % write window to
file.

% spectral analysis of output spectrum
Pave = mean(y(:,1));
y(:,1)=y(:,1)-Pave; % remove DC component
FFTY = fft(y(:,1).*w);
unique = ceil((length(y)+1)/2);
FFTY=abs(FFTY(1:unique))*2; % remove the redundant part and scale back the amplitude
(single sided)
FFTY(1)=FFTY(1)/2;   % Account for endpoint uniqueness
FFTY(length(FFTY))=FFTY(length(FFTY))/2;
%FFTY=FFTY/length(y);  % fft scaling - works if you don't have a window function
FFTY=FFTY/sum(w);% fft scaling - divide by the integral of the window function...
f=(0:unique-1)'*f_sample/length(y);

% drop 0 freq point.
FFTY=FFTY(2:end);f=f(2:end);

% RIN power:  <i(f)> ^ 2.  Average current a frequency, then squared.
% RIN = FFT of photons - average # photons - normalization to /Hz

specdata = 20*log10(FFTY) + 10*log10 ( unique / f_sample/1e9);   % updated oct 27/03

RIN = specdata   - 2*10*log10(Pave);
output_power_dBm = 10*log10(Pave)

global fr_index
if ~size(fr_index);    t=find ( specdata==max(specdata) ); fr_index=t(1),fr=f(fr_index)
else
    f(fr_index)
end;
spec_tot= 20*log10(sum ( smooth3(FFTY (1:fr_index),0.03) ) ); % total noise below
resonance frequency, over total bandwidth
RIN_tot= spec_tot   - 2*10*log10(Pave)
```

7.8. RIN calculations

```
        clear t y;
        inj_noise=INJ_NOISE;
        stepsize=1/f_sample;  % need 2x max freq.
        te=0.01;   numsteps=(te)/stepsize;
        tic;[t,y] = rk4fixed(@injection_eqs,[0 te],init',numsteps,ss2);ode_time=toc
        %           if PLOT_TIME_TRACE2     ;        plot_result(t,y);       end
        if ode_time > ODE_TIME_MAX/2;locked=locked-2;end
        if locked>0;
            te=1;   numsteps=(te)/stepsize;
            tic;[t,y] = rk4fixed(@injection_eqs,[0 te],init',numsteps,ss2);ode_time=toc
            if PLOT_TIME_TRACE2      ;        plot_result(t,y);       end
            % check if it is locked:
            tt = t; tt(1)=[]; tt = tt-t(1:length(t)-1); phi = y(:,2); phi(1)=[]; phi =
(phi-y(1:size(y,1)-1,2));u=find(t>0.6)-1;frequency_deltamax=std(phi(u)./tt(u)/2/pi)
            if frequency_deltamax > LINEWIDTH_MAX; locked=locked-8;end
        end
        if ode_time > ODE_TIME_MAX;locked=locked-4;end

        % RIN ...
        if locked > 0 & (~INJECTION | INJECTION_FULLSOLN )
            inj_noise=INJ_NOISE;
            te=SimulationTime;   numsteps=(te)/stepsize
            tic;[t,y] = rk4fixed(@injection_eqs,[0 te],init',numsteps,ss2);ode_time=toc
            solved_ODE=1;
            % convert to mW, sTp in ns, assume 1.55um
            % also assume 60% photon loss is the mirror loss and half of it output from
the top mirror
```

```
            y(:,1) = y(:,1)*6.626e-34*3e8/1.55e-6*1000/sTp/1e-9*0.6/2;      % mW
            index = find(t >= t_start);     index = index(1);% remove the turn on
transient portion. real signal starts from t_start
            t = t(index:length(t));        y = y(index:size(y,1),:);
            Pave = mean(y(:,1));  Pout = [Pout, Pave];      % output power.
            if PLOT_TIME_TRACE       ;plot_result(t,y);end; % plot the laser output as a
function of time
            [f, specdata, RIN, specdata_inj_tot, RIN_inj_tot]=spectral_analysis (t,y,
f_sample,WINDOW_FUNCTION);
                RINs=smooth3(RIN,0.03);specdata_s=smooth3(specdata,0.03);
            if PLOT_SPECTRUM
                figure (fig_spec);   hold on;               subplot(2,1,1);hold
on;ylabel ('Noise dBm/Hz');
                plot(f,specdata_s);xlim([0 fmax_plot])      % plot out the typical
spectrum
                subplot(2,1,2);hold on;plot(f,RINs); xlim([0 fmax_plot]);ylabel ('RIN
dB/Hz');xlabel('Frequency (GHz)');           % plot out the RIN spectrum
                if INJECTION; cond = [inj_eff detune];else; cond = [0 0]; end
                title(num2str(cond));    text ( 1,max(RIN), strcat ('Output power: ',
num2str(Pave),' mW'))
                dlmwrite ( '2.rin',RINs,'\t');
            end
            temp = abs(f - freq1);    p1 = find(temp==min(temp));    specdata_freq =
specdata_s(p1(1)); RIN_freq = RINs(p1(1));
            if S21_solve==0;t=find(RINs==max(RINs)); fr=f(t(1));end
            % combine all the data
            %             resultRIN= [resultRIN, RINs];
        else
            solved_ODE=0;                   ode_time
        end
```

Bibliography

[1] T. Marozsak and E. Udvary, "Vertical cavity surface emitting lasers in radio over fiber applications," presented at 14th International Conference on Microwaves, Radar and Wireless Communications. MIKON - 2002. Conference Proceedings (IEEE Cat.No.02EX562). Telecommun. Res. Inst. Part vol.1, 2002, pp.41-4 vol.1. Gdansk, Poland.

[2] N. Kanno and K. Ito, "Fiber optic subcarrier multiplexing transport for broadband subscriber distribution network," presented at IEEE International Conference on Communications. BOSTONICC/89. World Prosperity Through Communications (Cat. No.89CH2655-9). IEEE. 1989, pp.996-1003 vol.2. New York, NY, USA., 1989.

[3] K. Noguchi, H. Miyazawa, and O. Mitomi, "75-GHz Ti:LinNbO3 optical modulator," presented at Optical Fiber Communications Conference, 1994.

[4] C. H. Chang, L. Chrostowski, and C. J. Chang-Hasnain, "Parasitics and design considerations on oxide-implant VCSELs," *IEEE Photonics Technology Letters*, vol. 13, pp. 1274-6, 2001.

[5] K. Y. Lau, N. Bar-Chaim, I. Ury, C. Harder, and A. Yariv, "Direct amplitude modulation of short-cavity GaAs lasers up to X-band frequencies," *Applied Physics Letters*, vol. 43, pp. 1-3, 1983.

[6] S. Weisser, E. C. Larkins, K. Czotscher, W. Benz, J. Daleiden, I. Esquivias, J. Fleissner, J. D. Ralston, B. Romero, R. E. Sah, A. Schonfelder, and J. Rosenzweig, "Damping-limited modulation bandwidths up to 40 GHz in undoped short-cavity In0.35Ga0.65As-GaAs Multiple-quantum well lasers," *IEEE Photonics Technology Letters*, vol. 8, pp. 608-610, 1996.

[7] G. S. Li, R. F. Nabiev, W. Yuen, M. Jasen, D. Davis, and C. J. Chang-Hasnain, "Electrically-Pumped Directly-Modulated Tunable VCSEL for Metro DWDM Applications," *European Conf. On Optical Communications*, vol. 12, pp. 1686-1688, 2001.

[8] A. Pikovsky, M. Rosenblum, and J. Kurths, *Synchronization: A Universal Concept in Nonlinear Science*: Cambridge University Press, 2001.

[9] R. Adler, "A study of locking phenomena in oscillators," *Proc. IRE*, vol. 34, pp. 351-357, 1946.

[10] R. Lang, "Injection locking properties of a semiconductor laser," *IEEE Journal of Quantum Electronics*, vol. QE-18, pp. 976-83, 1982.

[11] P. Gallion, H. Nakajima, G. Debarge, and C. Chabran, "Contribution of spontaneous emission to the linewidth of an injection-locked semiconductor laser," *Electronics Letters*, vol. 21, pp. 626-8, 1985.

[12] N. A. Olsson, H. Temkin, R. A. Logan, L. F. Johnson, G. J. Dolan, J. P. van der Ziel, and J. C. Campbell, "Chirp-free transmission over 82.5 km of single mode fibers at 2 Gbit/s with injection locked DFB semiconductor lasers," *Journal of Lightwave Technology*, vol. LT-3, pp. 63-7, 1985.

[13] Y. Yamamoto and T. Kimura, "Coherent optical fiber transmission systems," *IEEE Journal of Quantum Electronics*, vol. 17, pp. 919-935, 1981.

[14] K. Iwashita and K. Nakagawa, "Suppression of mode partition noise by laser

diode light injection," *IEEE Transactions on Microwave Theory & Techniques*, vol. MTT-30, pp. 1657-62, 1982.
[15] S. Piazzolla, P. Spano, and M. Tamburrini, "Small signal analysis of frequency chirping in injection-locked semiconductor lasers," *IEEE Journal of Quantum Electronics*, vol. QE-22, pp. 2219-23, 1986.
[16] S. Mohrdiek, H. Burkhard, and H. Walter, "Chirp reduction of directly modulated semiconductor lasers at 10 Gb/s by strong CW light injection," *Journal of Lightwave Technology*, vol. 12, pp. 418-24, 1994.
[17] M. Xue Jun, C. Tai, and M. C. Wu, "Experimental demonstration of modulation bandwidth enhancement in distributed feedback lasers with external light injection," *Electronics Letters*, vol. 34, pp. 2031-2, 1998.
[18] X. J. Meng, C. Tai, and M. C. Wu, "Improved intrinsic dynamic distortions in directly modulated semiconductor lasers by optical injection locking," *IEEE Transactions on Microwave Theory & Techniques*, vol. 47, pp. 1172-6, 1999.
[19] N. Schunk and K. Petermann, "Noise analysis of injection-locked semiconductor injection lasers," *IEEE Journal of Quantum Electronics*, vol. QE-22, pp. 642-50, 1986.
[20] V. Annovazzi-Lodi, A. Scire, M. Sorel, and S. Donati, "Dynamic behavior and locking of a semiconductor laser subjected to external injection," *IEEE Journal of Quantum Electronics*, vol. 34, pp. 2350-7, 1998.
[21] S. Kobayashi and e. al., "Single mode operation of 500 Mbit/s modulated algaassemiconductor laser by injection locking," *Electronics Letters*, vol. 16, pp. 445-447, 1980.
[22] C. H. Henry, N. A. Olsson, and N. K. Dutta, "Locking Range and Stability of Injection Locked 1.54 um InGaAsP Semiconductor Lasers," *IEEE Journal of Quantum Electronics*, vol. QE-21, pp. 1152-1156, 1985.
[23] F. Mogensen, H. Olesen, and G. Jacobsen, "Locking conditions and stability properties for a semiconductor laser with external light injection," *IEEE Journal of Quantum Electronics*, vol. QE-21, pp. 784-93, 1985.
[24] O. Lidoyne, P. Gallion, C. Chabran, and G. Debarge, "Locking range, phase noise and power spectrum of an injection-locked semiconductor laser," *IEE Proceedings-J Optoelectronics*, vol. 137, pp. 147-54, 1990.
[25] I. Petitbon, P. Gallion, G. Debarge, and C. Chabran, "Locking bandwidth and relaxation oscillations of an injection-locked semiconductor laser," *IEEE Journal of Quantum Electronics*, vol. 24, pp. 148-54, 1988.
[26] J. Sacher, D. Baums, P. Panknin, W. Elsasser, and E. O. Gobel, "Intensity instabilities of semiconductor lasers under current modulation, external light injection and delayed feedback," *Physical Review A*, vol. 45, pp. 1893-905, 1992.
[27] T. B. Simpson, J. M. Liu, A. Gavrielides, V. Kovanis, and P. M. Alsing, "Period-doubling route to chaos in a semiconductor laser subject to optical injection," *Applied Physics Letters*, vol. 64, pp. 3539-41, 1994.
[28] T. B. Simpson, J. M. Liu, and A. Gavrielides, "Small-signal analysis of modulation characteristics in a semiconductor laser subject to strong optical injection," *IEEE Journal of Quantum Electronics*, vol. 32, pp. 1456-68, 1996.
[29] T. B. Simpson and J. M. Liu, "Enhanced modulation bandwidth in injection-locked semiconductor lasers," *IEEE Photonics Technology Letters*, vol. 9, pp.

1322-4, 1997.
[30] S. K. Hwang, J. M. Liu, and J. K. White, "35-GHz Modulation Bandwidth in Injection-Locked Semiconductor Lasers," presented at IEEE Lasers and Electro-Optics Society, Tucson, Arizona, 2003.
[31] X. Jin and S. L. Chuang, "Relative intensity noise characteristics of injection-locked semiconductor lasers," *Applied Physics Letters*, vol. 77, pp. 1250-2, 2000.
[32] T. B. Simpson, J. M. Liu, and A. Gavrielides, "Bandwidth enhancement and broadband noise reduction in injection-locked semiconductor lasers," *IEEE Photonics Technology Letters*, vol. 7, pp. 709-11, 1995.
[33] Y. Hong and K. A. Shore, "Locking characteristics of a side-mode injected semiconductor laser," *IEEE Journal of Quantum Electronics*, vol. 35, pp. 1713-17, 1999.
[34] J. Y. Law, G. H. M. van Tartwijk, and G. P. Agrawal, "Effects of transverse-mode competition on the injection dynamics of vertical-cavity surface-emitting lasers," *Quantum & Semiclassical Optics*, vol. 9, pp. 737-47, 1997.
[35] H. Li, T. L. Lucas, J. G. McInerney, M. W. Wright, and R. A. Morgan, "Injection locking dynamics of vertical cavity semiconductor lasers under conventional and phase conjugate injection," *IEEE Journal of Quantum Electronics*, vol. 32, pp. 227-35, 1996.
[36] D. L. Boiko, G. M. Stephan, and P. Besnard, "Fast polarization switching with memory effect in a vertical cavity surface emitting laser subject to modulated optical injection," *Journal of Applied Physics*, vol. 86, pp. 4096-9, 1999.
[37] Y. Onishi, N. Nishiyama, C. Caneau, F. Koyama, and C. E. Zah, "Optical Inverter Using a Vertical-Cavity Surface-Emitting Laser with External Light Injection," presented at IEEE Lasers and Electro-Optics Society, Tucson, Arizona, 2003.
[38] T. Fishman and A. Hardy, "Injection-locking analysis of vertical-cavity laser arrays," *Journal of the Optical Society of America B-Optical Physics*, vol. 16, pp. 38-45, 1999.
[39] T. Fishman and A. Hardy, "Effect of spatial hole burning on injection-locked vertical-cavity surface-emitting laser arrays," *Applied Optics*, vol. 39, pp. 3108-14, 2000.
[40] A. Kaszubowska, P. Anandarajah, and L. P. Barry, "Improved performance of a hybrid radio/fiber system using a directly modulated laser transmitter with external injection," *IEEE Photonics Technology Letters*, vol. 14, pp. 233-5, 2002.
[41] L. Hai-Han, H. Hsu-Hung, S. Heng-Sheng, and W. Ming-Chuan, "Fiber optical CATV system-performance improvement by using external light-injection technique," *IEEE Photonics Technology Letters*, vol. 15, pp. 1017-19, 2003.
[42] A. M. Yurek, L. Goldberg, H. F. Taylor, and J. F. Weller, "Millimeter-wave signal generation with an injection-locked laser diode," presented at IOOC-ECOC '85. 5th International Conference on Integrated Optics and Optical Fibre Communication and 11th European Conference on Optical Communication. Technical Digest. Istituto Int. Comunicazioni. 1985, pp.791-4 vol.1. Genoa, Italy., 1985.
[43] M. Al-Mumin, W. Xinhong, M. Weiming, S. A. Pappert, and L. Guifang, "Optical generation and sideband injection locking of tunable 11-120 GHz microwave/millimetre signals," *Electronics Letters*, vol. 36, pp. 1547-8, 2000.

[44] L. A. Johansson and A. Seeds, "Multi-octave photonic RF synthesiser based on two DFB lasers," *Electronics Letters*, vol. 38, pp. 563-4, 2002.
[45] H.-K. Sung, T. Jung, M. C. Wu, D. Tishinin, K. Y. Liou, and W. T. Tsang, "Optical Generation of Millimeter-waves using Monolithic Sideband Injection Locking of A Two-Section DFB Laser," presented at IEEE Lasers and Electro-Optics Society, Tucson, Arizona, 2003.
[46] T. Jung, "Demonstration of Monolithic Optical Injection Locking using a Two Section DFB Laser," *CLEO*, pp. CThC4, 2003.
[47] K. Weich, E. Patzak, and J. Horer, "Fast all-optical switching using two-section injection-locked semiconductor lasers," *Electronics Letters*, vol. 30, pp. 493-4, 1994.
[48] C. W. Chow, C. S. Wong, and H. K. Tsang, "8 x 10 Gb/s Multi-wavelength Injection Locking of a FP Laser Diode for WDM Multicast," presented at IEEE Lasers and Electro-Optics Society, Tucson, Arizona, 2003.
[49] L. Chrostowski, C. H. Chang, R. Stone, and C. J. Chang-Hasnain, "Uncooled Injection-Locked 1.55 um Tunable VCSEL as WDM Transmitter," presented at Optical Fiber Communications Conference, 2003.
[50] L. Chrostowski, C. H. Chang, and C. J. Chang-Hasnain, "Injection-Locked 1.55 um Tunable VCSEL for Uncooled WDM Transmitter Applications," *IEEE Photonics Technology Letters*, vol. (to be published), 2004.
[51] K.-P. Ho, "Optimal utilization in subcarrier and multicarrier Systems," in *Department of Electrical Engineering and Computer Science*: University of California at Berkeley, 1995.
[52] W. I. Way, "Subcarrier multiplexed lightwave system design considerations for subscriber loop applications," *Journal of Lightwave Technology*, vol. 7, pp. 1806-18, 1989.
[53] T. R. Chen, W. Hsin, and N. Bar-Chaim, "Very high power InGaAsP/InP distributed feedback lasers at 1550 nm wavelength," *Applied Physics Letters*, vol. 72, pp. 1269-71, 1998.
[54] A. Goutzoulis, J. Zomp, and A. Johnson, "An eight-element optically powered, directly modulated receive UHF fiber optic manifold," *Microwave Journal*, vol. 39, pp. 74, 76, 78, 80, 83-4, 86, 1996.
[55] E. I. Ackerman, C. Cox, III, G. Betts, H. Roussell, F. O'Donnell, and K. Ray, "Input impedance conditions for minimizing the noise figure of an analog optical link," *IEEE Transactions on Microwave Theory & Techniques*, vol. 46, pp. 2025-31, 1998.
[56] R. Olshansky, V. A. Lanzisera, and P. M. Hill, "Subcarrier multiplexed lightwave systems for broad-band distribution," *Journal of Lightwave Technology*, vol. 7, pp. 1329-42, 1989.
[57] C. Jianyao, R. J. Ram, and R. Helkey, "Linearity and third-order intermodulation distortion in DFB semiconductor lasers," *IEEE Journal of Quantum Electronics*, vol. 35, pp. 1231-7, 1999.
[58] R. V. Dalal, R. J. Ram, R. Helkey, H. Roussell, and K. D. Choquette, "Low distortion analogue signal transmission using vertical cavity lasers," *Electronics Letters*, vol. 34, pp. 1590-1, 1998.
[59] S. A. Pappert, C. K. Sun, R. J. Orazi, and T. E. Weiner, "Microwave fiber optic

links for shipboard antenna applications," presented at Proceedings 2000 IEEE International Conference on Phased Array Systems and Technology (Cat. No.00TH8510). IEEE. 2000, pp.345-8. Piscataway, NJ, USA., 2000.
[60] G. E. Betts, "Linearized modulator for suboctave-bandpass optical analog links," *IEEE Transactions on Microwave Theory & Techniques*, vol. 42, pp. 2642-9, 1994.
[61] H. L. T. Lee, R. V. Dalal, R. J. Ram, and K. D. Choquette, "Dynamic range of vertical-cavity surface-emitting lasers in multimode links," *IEEE Photonics Technology Letters*, vol. 11, pp. 1473-5, 1999.
[62] J. Piprek, K. Takiguchi, K. A. Black, E. L. Hu, and J. E. Bowers, "Harmonic distortion in 1.55- mu m vertical-cavity lasers," *IEEE Photonics Technology Letters*, vol. 12, pp. 1686-8, 2000.
[63] R. B. Welstand, S. A. Pappert, C. K. Sun, J. T. Zhu, Y. Z. Liu, and P. K. L. Yu, "Dual-function electroabsorption waveguide modulator/detector for optoelectronic transceiver applications," *IEEE Photonics Technology Letters*, vol. 8, pp. 1540-2, 1996.
[64] R. B. Welstand, J. T. Zhu, W. X. Chen, A. R. Clawson, P. K. L. Yu, and S. A. Pappert, "Combined Franz-Keldysh and quantum-confined Stark effect waveguide modulator for analog signal transmission," *Journal of Lightwave Technology*, vol. 17, pp. 497-502, 1999.
[65] K. Asatani and T. Kimura, "Linearization of LED nonlinearity by predistortions," *IEEE Transactions on Electron Devices*, vol. ED-25, pp. 207-12, 1978.
[66] L. Hung-Tser and K. Yao-Huang, "Nonlinear distortions and compensations of DFB laser diode in AM-VSB lightwave CATV applications," *Journal of Lightwave Technology*, vol. 14, pp. 2567-74, 1996.
[67] F. Zepparelli, L. Roselli, F. Ambrosi, R. Sorrentino, P. Faccin, and A. Casini, "Modelling and design of a broadband predistortion circuit for radio-over-fibre systems," presented at Inst. Electron. Inf. & Commun. Eng. IEICE Transactions on Electronics, vol.E85-C, no.3, March 2002, pp.519-26. Japan., 2003.
[68] T. Ismail and A. J. Seeds, "Nonlinear distortion reduction in directly modulated semiconductor laser using feedforward linearisation," *http://www.ee.ucl.ac.uk/lcs/papers2003/93.pdf*, 2003.
[69] L. S. Fock, A. Kwan, and R. S. Tucker, "Reduction of semiconductor laser intensity noise by feedforward compensation: experiment and theory," *Journal of Lightwave Technology*, vol. 10, pp. 1919-25, 1992.
[70] L. S. Fock and R. S. Tucker, "Simultaneous reduction of intensity noise and distortion in semiconductor lasers by feedforward compensation," *Electronics Letters*, vol. 27, pp. 1297-9, 1991.
[71] M. H. Pua, M. K. Haldar, F. V. C. Mendis, and H. K. Garg, "Reduction of nonlinear distortion in semiconductor lasers with external light injection," *International Conference on Information, Communications and Signal Processing*, pp. 1153-1157, 1997.
[72] J. H. Seo, Y. K. Seo, and W. Y. Choi, "Nonlinear distortion suppression in directly modulated DFB lasers by sidemode optical injection," *IEEE MTT-S Digest*, pp. 555-558, 2001.
[73] K. Y. Lau, "PhD Thesis, Chapter 2."

[74] J. B. Moreno, *Journal of Applied Physics*, vol. 48, pp. 4152, 1977.
[75] C. H. Chang, L. Chrostowski, and C. J. Chang-Hasnain, "Injection Locking of VCSELs," *(accepted for publication in) Journal of Selected Topics in Quantum Electronics*, 2003.
[76] C.-H. Chang, "High Speed Vertical Cavity Surface Emitting Lasers with Injection Locking," 2002.
[77] L. Chrostowski, M. Moewe, W. Zhao, C. H. Chang, C. Chang-Hasnain, R. Shau, M. Ortsiefer, and M. C. Amann, "39 GHz Intrinsic Bandwidth of a 1.55 um Injection-Locked VCSEL," *(submitted to) Conference on Lasers and Electro-Optics*, 2004.
[78] K. Y. Lau and A. Yariv, "Intermodulation distortion in a directly modulated semiconductor injection laser," *Applied Physics Letters*, vol. 45, pp. 1034-6, 1984.
[79] G. Yabre and J. Le Bihan, "Reduction of nonlinear distortion in directly modulated semiconductor lasers by coherent light injection," *IEEE Journal of Quantum Electronics*, vol. 33, pp. 1132-40, 1997.
[80] J. Wang, M. K. Haldar, L. Li, and F. V. C. Mendis, "Enhancement of modulation bandwidth of laser diodes by injection locking," *IEEE Photonics Technology Letters*, vol. 8, pp. 34-6, 1996.
[81] L. Li, "Static and dynamic properties of injection-locked semiconductor lasers," *IEEE Journal of Quantum Electronics*, vol. 30, pp. 1701-8, 1994.
[82] R. Hui, A. D'Ottavi, A. Mecozzi, and P. Spano, "Injection locking in distributed feedback semiconductor lasers," *IEEE Journal of Quantum Electronics*, vol. 27, pp. 1688-95, 1991.
[83] O. Lidoyne, P. B. Gallion, and D. Erasme, "Modulation properties of an injection-locked semiconductor laser," *IEEE Journal of Quantum Electronics*, vol. 27, pp. 344-51, 1991.
[84] K. L. Lear, M. Ochiai, V. M. Hietala, H. Q. Hou, B. E. Hammons, J. J. Banas, and J. A. Nevers, "High-speed vertical cavity surface emitting lasers," presented at 1997 Digest of the IEEE/LEOS Summer Topical Meetings: Vertical-Cavity Lasers/Technologies for a Global Information Infrastructure/WDM Components Technology/Advanced Semiconductor Lasers and Applications/Gallium Nitride Materials, Processing, and Devices (Cat. No.97TH8276). IEEE. 1997, pp.53-4. New York, NY, USA., 1997.
[85] M. Ortsiefer, "High-speed modulation up to 10 Gbit/s with 1.55 m wavelength InGaAlAs VCSELs," *Electronics Letters*, 2002.
[86] J. C. Carlledge and R. C. Srinivasan, "Extraction of DFB laser rate equation parameters for system simulation purposes," *Journal of Lightwave Technology*, 1997.
[87] M. Ortsiefer, R. Shau, F. Mederer, R. Michalzik, J. Rosskopf, G. Bohm, F. Kohler, C. Lauer, M. Maute, and M. C. Amann, "High-speed modulation up to 10 Gbit/s with 1.55 mu m wavelength InGaAlAs VCSELs," *Electronics Letters*, vol. 38, pp. 1180-1, 2002.
[88] B. Stegmueller, E. Baur, and M. Kicherer, "15-GHz modulation performance of integrated DFB laser diode EA modulator with identical multiple-quantum-well double-stack active layer," *IEEE Photonics Technology Letters*, vol. 14, pp. 1647-9, 2002.

[89] D. E. McCumber, "Intensity fluctuations in output of cw laser oscillators. I," *Phys. Review*, vol. 141, pp. 306-322, 1966.
[90] C. Harder, J. Katz, S. Margalit, J. Shacham, and A. Yariv, "Noise equivalent circuit of a semiconductor laser diode," *IEEE Journal of Quantum Electronics*, vol. QE-18, pp. 333-7, 1982.
[91] D. Marcuse, "Computer simulation of laser photon fluctuations: Theory of single-cavity laser," *IEEE Journal of Quantum Electronics*, vol. QE-20, pp. 1139-48, 1984.
[92] G. P. Agrawal and N. K. Dutta, *Semiconductor Lasers*, 2nd ed. New York: Van Nostrand Reinhold, 1993.
[93] D. Wiedenmann, P. Schnitzer, C. Jung, M. Grabherr, R. Jager, R. Michalzik, and K. J. Ebeling, "Noise characteristics of 850 nm single-mode vertical cavity surface emitting lasers," *Applied Physics Letters*, vol. 73, pp. 717-19, 1998.
[94] D. Wiedenmann, M. Kicherer, C. Jung, M. Grabherr, M. Miller, R. Jager, and K. J. Ebeling, "Sub-poissonian intensity noise from vertical-cavity surface-emitting lasers," *Applied Physics Letters*, vol. 75, pp. 3075-7, 1999.
[95] P. Spano, S. Piazzola, and M. Tamburrini, "Measurements of the injection-locked influence on the frequency noise spectrum of single mode semiconductor lasers," *Optics Letters*, vol. 10, pp. 556-558, 1985.
[96] F. Mogensen, H. Olesen, and G. Jacobsen, "FM noise suppression and linewidth reduction in an injection-locked semiconductor laser," *Electronics Letters*, vol. 21, pp. 696-7, 1985.
[97] P. Spano, S. Piazzolla, and M. Tamburrini, "Frequency and intensity noise in injection-locked semiconductor lasers: theory an experiments," *IEEE Journal of Quantum Electronics*, vol. QE-22, pp. 427-35, 1986.
[98] M. C. Espana-Boquera and A. Puerta-Notario, "Noise effects in injection locked laser simulation: phase jumps and associated spectral components," *Electronics Letters*, vol. 32, pp. 818-19, 1996.
[99] J. M. Liu, H. F. Chen, X. J. Meng, and T. B. Simpson, "Modulation bandwidth, noise, and stability of a semiconductor laser subject to strong injection locking," *IEEE Photonics Technology Letters*, vol. 9, pp. 1325-7, 1997.
[100] G. Yabre, H. De Waardt, H. P. A. van den Boom, and G. D. Khoe, "Noise characteristics of single-mode semiconductor lasers under external light injection," *IEEE Journal of Quantum Electronics*, vol. 36, pp. 385-93, 2000.
[101] K. Schunk, G. Grosskopf, L. Kuller, and K. Petermann, "Noise characteristics of injection locked semiconductor lasers," presented at IOOC-ECOC '85. 5th International Conference on Integrated Optics and Optical Fibre Communication and 11th European Conference on Optical Communication. Technical Digest. Istituto Int. Comunicazioni. 1985, pp.717-20 vol.1. Genoa, Italy.
[102] C. H. Chang, L. Chrostowski, and C. H. Chang, "Frequency Response of an Injection-Locked Laser," *CLEO*, 2002.
[103] Agilent_Technologies, "Lightwave Signal Analyzers Measure Relative Intensity Noise, Product Note 71400-1."
[104] D. M. Baney, P. Gallion, and R. S. Tucker, "Theory and measurement techniques for the noise figure of optical amplifiers," *Optical Fiber Technology*, vol. 6, pp. 122-54, 2000.

[105] I. Jacobs, "Dependence of optical amplifier noise figure on relative-intensity-noise," *Journal of Lightwave Technology*, vol. 13, pp. 1461-5, 1995.
[106] D. V. Kuksenkov, T. H., and S. S., "Polarization instability and relative intensity noise in Vertical-Cavity Surface-Emitting Lasers."
[107] W. I. Way, C. Lin, C. E. Zah, L. Curtis, R. Spicer, and W. C. Young, "Multiple-reflection-induced intensity noise studies in a lightwave system for multichannel AM-VSB television signal distribution," *IEEE Photonics Technology Letters*, vol. 2, pp. 360-362, 1990.
[108] K. Petermann and E. Weidel, "Semiconductor laser noise in an interferometer system," *IEEE Journal of Quantum Electronics*, vol. QE-17, pp. 1251-6, 1981.
[109] W. I. Way, C. Lin, C. E. Zah, L. Curtis, R. Spicer, and W. C. Young, "Multiple-reflection-induced intensity noise studies in a lightwave system for multichannel AM-VSB television signal distribution," *IEEE Photonics Technology Letters*, vol. 2, pp. 360-2, 1990.
[110] S. Wu, A. Yariv, H. Blauvelt, and N. Kwong, "Theoretical and experimental investigation of conversion of phase noise to intensity noise by Rayleigh scattering in optical fibers," *Applied Physics Letters*, vol. 59, pp. 1156-8, 1991.
[111] H. X. Shi, D. A. Cohen, J. Barton, M. Majewski, L. A. Coldren, M. C. Larson, and G. A. Fish, "Dynamic range of widely tunable sampled grating DBR lasers," *Electronics Letters*, vol. 38, pp. 180-1, 2002.
[112] A. S. Daryoush, E. Ackerman, N. R. Samant, S. Wanuga, and D. Kasemset, "Interfaces for high speed fiber-optic links: analysis and experiment," *IEEE Transactions on Microwave Theory & Techniques, vol.39, no.12, Dec. 1991, pp.2031-44. USA.*
[113] T. B. Warren and J. Kouzoujian, "SOME NOTES ON COMPOSITE SECOND AND THIRD ORDER INTERMODULATION DISTORTIONS," Matrix Test Equipment Dec 15 1998.
[114] T. B. Warren and J. Kouzoujian, "THE RELATIONSHIP OF INTERCEPT POINTS AND COMPOSITE DISTORTIONS," Matrix Test Equipment February 18 1998.
[115] G. E. Bodeep and T. E. Darcie, "Semiconductor lasers versus external modulators: a comparison of nonlinear distortion for lightwave subcarrier CATV applications," *IEEE Photonics Technology Letters*, vol. 1, pp. 401-3, 1989.
[116] A. A. M. Saleh, "Fundamental limit on number of channels in subcarrier-multiplexed lightwave CATV system," *Electronics Letters*, vol. 25, pp. 776-7, 1989.
[117] T. E. Darcie, "Subcarrier multiplexing for lightwave networks and video distribution systems," *IEEE Journal on Selected Areas in Communications*, vol. 8, pp. 1240-8, 1990.
[118] N. J. Frigo, M. R. Phillips, and G. E. Bodeep, "Clipping distortion in lightwave CATV systems: models, simulations, and measurements," *Journal of Lightwave Technology*, vol. 11, pp. 138-46, 1993.
[119] M. R. Phillips and T. E. Darcie, "Numerical simulation of clipping-induced distortion in analog lightwave systems," *IEEE Photonics Technology Letters*, vol. 3, pp. 1153-5, 1991.
[120] T. E. Darcie and G. E. Bodeep, "Lightwave subcarrier CATV transmission

systems," *IEEE Transactions on Microwave Theory & Techniques*, vol. 38, pp. 524-33, 1990.
[121] K. E. Stubkjr, "Nonlinearity of DH GaAlAs lasers," *Electronics Letters*, vol. 15, pp. 61-3, 1979.
[122] J. Wang, M. K. Haldar, and F. V. C. Mendis, "Formula for two-carrier third-order intermodulation distortion in semiconductor laser diodes," *Electronics Letters*, vol. 29, pp. 1341-3, 1993.
[123] J. Helms, "Intermodulation and harmonic distortions of laser diodes with optical feedback," *Journal of Lightwave Technology*, vol. 9, pp. 1567-75, 1991.
[124] W. E. Stephens and T. R. Joseph, "System characteristics of direct modulated and externally modulated RF fiber-optic links," *Journal of Lightwave Technology*, vol. LT-5, pp. 380-7, 1987.
[125] C. H. Cox, III, G. E. Betts, and L. M. Johnson, "An analytic and experimental comparison of direct and external modulation in analog fiber-optic links," *IEEE Transactions on Microwave Theory & Techniques*, vol. 38, pp. 501-9, 1990.
[126] C. J. Chang-Hasnain, "Tunable VCSEL," *IEEE Journal of Selected Topics in Quantum Electronics*, vol. 6, pp. 978-87, 2000.
[127] G. K. Gopalakrishnan, T. J. Brophy, and C. Breverman, "Experimental study of fibre induced distortions in externally modulated 1550 nm analogue CATV links," *Electronics Letters*, vol. 32, pp. 1309-10, 1996.
[128] M. R. Phillips, T. E. Darcie, D. Marcuse, G. E. Bodeep, and N. J. Frigo, "Nonlinear distortion generated by dispersive transmission of chirped intensity-modulated signals," *IEEE Photonics Technology Letters*, vol. 3, pp. 481-3, 1991.
[129] L. Ki-Hyuk, C. Hyun-Yong, and C. Woo-Young, "Analysis of chromatic dispersion-induced second-harmonic distortions including laser dynamics to the second order," *IEEE Journal of Quantum Electronics*, vol. 39, pp. 640-6, 2003.
[130] E. E. Bergmann, C. Y. Kuo, and S. Y. Huang, "Dispersion-induced composite second-order distortion at 1.5 mu m," *IEEE Photonics Technology Letters*, vol. 3, pp. 59-61, 1991.
[131] G. H. Smith, D. Novak, and Z. Ahmed, "Overcoming chromatic-dispersion effects in fiber-wireless systems incorporating external modulators," *IEEE Transactions on Microwave Theory & Techniques*, vol. 45, pp. 1410-15, 1997.
[132] M. Bhattacharya, R. Mukherjee, and T. Chattopadhyay, "Reduction of frequency chirping in semiconductor lasers through injection locking," *Iete Journal of Research*, vol. 45, pp. 341-4, 1999.
[133] M. Tamburrini, S. Piazzolla, and P. Spano, "Reduction of the frequency chirping in semiconductor lasers using injection-locking," presented at ECOC 12th European Conference on Optical Communication. Technical Digest. Telefonica. 1986, pp.515-18 vol.1. Madrid, Spain., 1986.
[134] C. Y. Kuo, "Fundamental nonlinear distortions in analog links with fiber amplifiers," *Journal of Lightwave Technology*, vol. 11, pp. 7-15, 1993.
[135] C. H. Chang, L. Chrostowski, and C. Chang-Hasnain, "Enhanced VCSEL Performance by Optical Injection Locking for Analog and Digital Applications," presented at Laser and Electro Optic Society, Tucson, AZ, 2003 (to be presented).
[136] C. H. Chang, L. Chrostowski, C. J. Chang-Hasnain, and W. W. Chow, "Study of long-wavelength VCSEL-VCSEL injection locking for 2.5-Gb/s transmission,"

IEEE Photonics Technology Letters, vol. 14, pp. 1635-7, 2002.
[137] L. Chrostowski, C. Chih-Hao, and C. J. Chang-Hasnain, "Enhancement of dynamic range in 1.55- mu m VCSELs using injection locking," *IEEE Photonics Technology Letters*, vol. 15, pp. 498-500, 2003.
[138] C. H. Chang, L. Chrostowski, and C. J. Chang-Hasnain, "Transmission improvement of VCSEL at 2.5Gb/s under injection locking by another VCSEL," presented at LEOS 2001. 14th Annual Meeting of the IEEE Lasers and Electro-Optics Society (Cat. No.01CH37242). IEEE. Part vol.2, 2001, pp.728-9 vol.2. Piscataway, NJ, USA.
[139] C. M. Depriest, T. Yimaz, P. J. Delfyett, Jr., S. Etemad, A. Braun, and J. Abeles, "Ultralow noise and supermode suppression in an actively mode-locked external-cavity semiconductor diode ring laser," *Optics Letters*, vol. 27, pp. 719-21, 2002.
[140] C. F. C. Silva, A. J. Seeds, and P. J. Williams, "Terahertz span >60-channel exact frequency dense WDM source using comb generation and SG-DBR injection-locked laser filtering," *IEEE Photonics Technology Letters*, vol. 13, pp. 370-2, 2001.
[141] U. Fiedler and K. J. Ebeling, "Design of VCSEL's for feedback insensitive data transmission and external cavity active mode-locking," *IEEE Journal of Selected Topics in Quantum Electronics*, vol. 1, pp. 442-50, 1995.